COPPE
Instituto Alberto Luiz Coimbra de
Pós-Graduação e Pesquisa de Engenharia
UFRJ

RADIO FREQUENCY INTERFERENCE DETECTION AND MITIGATION FOR GNSS AND RADIO ASTRONOMY APPLICATIONS

Felipe Barboza da Silva

Tese de Doutorado apresentada ao Programa de Pós-graduação em Engenharia Elétrica, COPPE, da Universidade Federal do Rio de Janeiro, como parte dos requisitos necessários à obtenção do título de Doutor em Engenharia Elétrica.

Orientadores: Wallace Alves Martins
Ediz Cetin

Rio de Janeiro
Abril de 2022

RADIO FREQUENCY INTERFERENCE DETECTION AND MITIGATION FOR GNSS AND RADIO ASTRONOMY APPLICATIONS

Felipe Barboza da Silva

TESE SUBMETIDA AO CORPO DOCENTE DO INSTITUTO ALBERTO LUIZ COIMBRA DE PÓS-GRADUAÇÃO E PESQUISA DE ENGENHARIA DA UNIVERSIDADE FEDERAL DO RIO DE JANEIRO COMO PARTE DOS REQUISITOS NECESSÁRIOS PARA A OBTENÇÃO DO GRAU DE DOUTOR EM CIÊNCIAS EM ENGENHARIA ELÉTRICA.

Orientadores: Wallace Alves Martins
Ediz Cetin

Aprovada por: Prof. Wallace Alves Martins
Prof. Ediz Cetin
Prof. Raimundo Sampaio-Neto
Prof. Bhavani Shankar Mysore Rama Rao
Prof. Paulo Sergio Ramirez Diniz

RIO DE JANEIRO, RJ – BRASIL
ABRIL DE 2022

Silva, Felipe Barboza da

Radio Frequency Interference Detection and Mitigation for GNSS and Radio Astronomy Applications/Felipe Barboza da Silva. – Rio de Janeiro: UFRJ/COPPE, 2022.

XXI, 83 p.: il.; 29,7cm.

Orientadores: Wallace Alves Martins
Ediz Cetin

Tese (doutorado) – UFRJ/COPPE/Programa de Engenharia Elétrica, 2022.

Referências Bibliográficas: p. 71 – 80.

1. radio frequency interference. 2. global navigation satellite systems. 3. radio astronomy. 4. nonnegative matrix factorisation. I. Martins, Wallace Alves *et al.* II. Universidade Federal do Rio de Janeiro, COPPE, Programa de Engenharia Elétrica. III. Título.

Preface

The doctorate works started in March 2018 at the Electrical Engineering Program (PEE) of the Alberto Luiz Coimbra Institute for Graduate Studies and Research in Engineering (Coppe) of Federal University of Rio de Janeiro (UFRJ), Rio de Janeiro, Brazil. From March 2019 to March 2022, the research was conducted at the Faculty of Science and Engineering at Macquarie University (MQ), Sydney, Australia, with a considerable period affected by the restrictions due to the COVID-19 pandemic. This work has been under cotutelle supervision of Professor Ediz Cetin (MQ), and Professor Wallace A. Martins (UFRJ & University of Luxembourg).

The members of the assessment committee are: Professor Ediz Cetin, MQ; Professor Wallace A. Martins, UFRJ & University of Luxembourg;[1] Professor Raimundo S. Neto, PUC-Rio; Professor Bhavani Shankar M.R. Rao, University of Luxembourg; and Professor Paulo S.R. Diniz, UFRJ.

This doctorate work was funded by the Conselho Nacional de Desenvolvimento Científico e Tecnológico (CNPq), from March 2018 to December 2019, and by the Macquarie University Research Excellence Scholarship (MQRES) program from March 2019 to April 2022.

---

[1] Dr. W. A. Martins was then working as Research Scientist with the University of Luxembourg.

Agradecimentos

Agradeço à minha família pelo suporte dado para que meu doutorado pudesse virar realidade. Em especial, agradeço ao meus pais, Carla e Fernando, que sempre acreditaram que eu pudesse um dia me candidatar ao título de doutorado. As mudanças recentes que a minha vida teve, como por exemplo o novo/velho mundo que vivemos com a pandemia, e a minha mudança para um país mais de 15 mil quilômetros distante de casa (Sydney agora também é minha casa), me fizeram valorizar ainda mais o peso que minha família tem em minha vida. Eu tenho certeza que não teria conseguido chegar aqui sem eles.

Ao meu irmão, Fábio, que eu descobri ser mais forte que eu, agradeço por estar do meu lado durante todos esses anos. Ao meu avô Oscar, sou muito grato pelo apoio incondicional desde o início da minha graduação.

Agradeço à minha companheira Caroline por entender todos (ou quase todos) os “não posso sair hoje”, por me ajudar com a ansiedade durante meu doutorado, e por ter me aturado durante os *lockdowns*. Eu te amo.

Ao meu orientador Wallace Martins por ter contribuído na minha formação, não só como profissional, mas também como pessoa. Apesar de eu ter tirado 3,3/10 como primeira nota no teste de Teoria Eletromagnética, você me convidou para trabalhar contigo. Desde então são 9 anos de parceria. Sou realmente grato por todo o seu esforço e dedicação.

Agradeço também ao meu outro orientador Ediz Cetin, cuja receptividade e capacidade de compreensão foram fundamentais para que eu pudesse executar um bom trabalho depois de mudar de país. Hoje eu posso dizer que eu fui extremamente sortudo por ter Wallace e Ediz como orientadores.

Aos meu amigos Matheus Marins e Lucas Cinelli por sempre estarem dispostos a tomar uma cerveja comigo e ouvir as besteiras que eu falo. Mesmo longe, eu não esquecerei de vocês. Eu os aguardo para uma visita à Sydney. Sou grato pelos amigos que fiz por aqui, em especial Lívia Constant e Andre Aquino por todo o carinho e acolhimento desde o dia que os conheci.

Agradeço aos professores do SMT, Marcello Campos e Luiz Wagner, pelo carinho e atenção dados enquanto aluno em suas disciplinas. Agradeço também aos professores Markus Lima e Tadeu Ferreira por todas as nossas conversas no laboratório.

Agradeço também ao Conselho Nacional de Desenvolvimento Científico e Tecnológico (CNPq) e ao Macquarie University Research Excellence Scholarship program por me fornecerem suporte financeiro durante meu doutorado.

Agradeço aos Profs. Raimundo S. Neto, Bhavani Shankar M.R. Rao, Paulo S.R. Diniz, Ediz Cetin e Wallace A. Martins por participarem da minha banca de doutorado.

Acknowledgements

I thank my family for the given support so that I could pursue my PhD degree. In particular, I thank my parents, Carla and Fernando, who always believed that one day I could candidate for the Doctorate degree. The recent changes in my life, such as the new/old world that we live with this pandemic, and the move to a country 15 thousand kilometres away from home (Sydney is also my home), made me value even further the impact that my family have in my life. I am sure that I would not be able to come to this stage without them.

To my brother, Fabio, which I realised is stronger than me, I thank you for being by my side throughout all these years. To my grandfather Oscar, I am very grateful for the unconditional support provided since the beginning of my undergraduate studies.

I thank my partner Caroline for understanding all the (or almost all the) “I can’t go out today”, for helping me with my anxiety during my PhD, and for putting up with me during the lockdowns. I love you.

To my supervisor Wallace Martins for having contributed to my training, not only as a professional but also as a person. Although I got 3.3/10 as my first mark on the Electromagnetic Theory exam, you invited me to work with you. Since then, our partnership is 9-years long. I am really thankful for all your effort and dedication.

I also thank my other supervisor Ediz Cetin, whose receptivity and comprehension capability were fundamental so that I could do good work after moving to another country. Today, I can say that I was extremely lucky for having Wallace and Ediz as my supervisors.

To my friends Matheus Marins and Lucas Cinelli for always being willing to grab some beer with me and for listening to the silly things I say. Even far apart, I will not forget you. I await your visit to Sydney. I am grateful for the friends I made here, in particular Lívia Constant e Andre Aquino for all love and reception since the day we first met.

I thank the professors from SMT Marcello Campos e Luiz Wagner for the fondness and attention given to me while a student in their units. I also thank Markus Lima e Tadeu Ferreira for all of our chats in the laboratory.

I also thank the Conselho Nacional de Desenvolvimento Científico e Tecnológico

(CNPq) and the Macquarie University Research Excellence Scholarship program for funding my doctorate research.

I thank Professors Raimundo S. Neto, Bhavani Shankar M.R. Rao, Paulo S.R. Diniz, Ediz Cetin and Wallace A. Martins for being part of the assessment committee of this thesis.

Resumo da Tese apresentada à COPPE/UFRJ como parte dos requisitos necessários para a obtenção do grau de Doutor em Ciências (D.Sc.)

DETECÇÃO E MITIGAÇÃO DE INTERFERÊNCIA DE RÁDIO FREQUÊNCIA PARA APLICAÇÕES DE GNSS E RÁDIO ASTRONOMIA

Felipe Barboza da Silva

Abril/2022

Orientadores: Wallace Alves Martins
Ediz Cetin

Programa: Engenharia Elétrica

Neste trabalho nós investigamos técnicas para detecção e mitigação de interferência de rádio frequência (RFI, do inglês *radio frequency interference*) em sistemas globais de navegação por satélite (GNSS, do inglês *global navigation satellite systems*) e aplicações de rádio astronomia. No contexto de GNSS, a tese propõe um detector baseado na fatoração de matrizes não-negativas (NMF, do inglês *nonnegative matrix factorisation*) o qual proporciona capacidade de detecção competitiva e baixas taxas de falso-alarme para sinais de RFI de faixas estreita e larga. Esquemas baseados em NMF para mitigação de RFI também são propostos, superando técnicas clássicas comumente utilizadas na literatura em cenários com interferência forte. Além disso, a proposta é capaz de suprimir diferentes tipos de RFI sem informação prévia sobre a interferência. Com respeito à aplicação de rádio astronomia, nosso detector em tempo-frequência atinge altas taxas de detecção com poucos falso-alarmes, com desempenho superior usando sinais reais quando comparado com métodos amplamente utilizados nesse domínio. Além do mais, a tese propõe três esquemas baseados em NMF para supressão de RFI para aplicações de rádio astronomia. Resultados indicam que um desempenho promissor em mitigação de RFI pode ser alcançados com mínima degradação na observação de pulsares, sinalizando que NMF pode ser uma potencial ferramenta no campo de rádio astronomia.

Abstract of Thesis presented to COPPE/UFRJ as a partial fulfillment of the requirements for the degree of Doctor of Science (D.Sc.)

RADIO FREQUENCY INTERFERENCE DETECTION AND MITIGATION FOR GNSS AND RADIO ASTRONOMY APPLICATIONS

Felipe Barboza da Silva

April/2022

Advisors: Wallace Alves Martins
Ediz Cetin

Department: Electrical Engineering

In this work, we investigate techniques to detect and mitigate radio frequency interference (RFI) in global navigation satellite systems (GNSS) and radio astronomy applications. In the context of GNSS, a nonnegative matrix factorisation (NMF)-based detector is proposed which provides competitive detection capability and low false alarm rates for narrow and wideband RFI signals. NMF-based frameworks for RFI mitigation are also proposed, outperforming techniques commonly used in the literature in strong interference scenarios. Further, the proposed technique is able to suppress multiple, different types of RFI without any prior information on the interference. Concerning the radio astronomy application, the proposed time-frequency detector achieves high detection rates with low false alarms, with superior performance using real-life signals when compared with methods widely used in this domain. Moreover, three NMF-based schemes for RFI suppression for radio astronomy applications are proposed. Results show that promising RFI mitigation performance can be achieved with minimal degradation on the pulsar observation, signalling that NMF can be a potential tool in the radio astronomy field.

Contents

List of Figures

List of Tables

List of Symbols

A	total jammer power, p. 10
B	chirp frequency bandwidth, p. 9
E	total GNSS signal power, p. 10
E_p	p^{th} GNSS signal power, p. 8
$G(\cdot)$	voting scheme operator, p. 30
$\mathbf{H}$	time activation matrix, p. 10
L	window length, p. 12
$\mathcal{L}(\cdot)$	generic distance function, p. 11
M	number of time instants, p. 13
N	number of DFT bins, p. 12
P	number of in-view satellites, p. 8
R	hop size, p. 13
S	number of components, p. 11
T	chirp period, p. 9
$\mathbf{W}$	dictionary matrix, p. 10
$\mathbf{X}$	nonnegative input matrix, p. 10
β	similarity parameter, p. 11
$\circledcirc$	element-wise exponentiation operator, p. 11
$C_{\min}$	minimum distance to the optimum detection point, p. 16
c_p	p^{th} spreading code, p. 8

$\mathbb{C}$	complex set, p. 9
R_{d}	detection rate, p. 16
d_p	p^{th} navigation data, p. 8
$\mathrm{E}\left[\cdot\right]$	expected value operator, p. 46
R_{fa}	false alarm rate, p. 16
$\mathbf{f}$	ADS-B template vector, p. 29
f_{c}	carrier frequency, p. 8
$f_{\mathrm{d},p}$	p^{th} Doppler frequency, p. 8
$f[i]$	window function, p. 13
F_{s}	sampling frequency, p. 9, 17
$\bar{\gamma}$	detection threshold, p. 14
$\mathbf{H}_{\mathrm{RFI}}$	time activation matrix of the RFI, p. 36
$\mathbf{H}_{\mathrm{SOI}}$	time activation matrix of the signal of interest, p. 36
$\lVert \cdot \rVert_2$	l_2-norm, p. 14
$\mathcal{M}(\cdot)$	median operator, p. 14
$\mathbb{N}$	natural set, p. 29
$\otimes$	element-wise product operator, p. 11
Q	sampled data-length, p. 9
$\mathbf{r}[i]$	received signal as a vector, p. 9
$r[i]$	received signal in the discrete time domain, p. 9
$r(t)$	received signal in the continuous time domain, p. 8
$\lfloor \cdot \rceil$	operator that rounds to the nearest integer, p. 9
$\mathbb{R}_+$	real positive set, p. 10
$\mathbf{r}_{\mathrm{RFI}}[i]$	RFI signal as a vector, p. 36
$\mathbb{R}$	real set, p. 8

$\mathbf{r}_{\mathrm{RFI}}[i]$	signal of interest as a vector, p. 36
$s_p[i]$	received GNSS signal in the discrete time domain, p. 9
σ^2	noise variance, p. 10
$s_p(t)$	received p^{th}-GNSS signal in the continuous time domain, p. 8
$\succeq$	entry-wise nonnegativeness operator, p. 11
τ_p	p^{th} code delay, p. 8
$(\cdot)^{\mathsf{T}}$	transpose operator, p. 11
$\mathrm{Var}\left[\cdot\right]$	sample variance operator, p. 46
$\mathbf{W}_{\mathrm{RFI}}$	dictionary matrix of the RFI, p. 36
$\mathbf{W}_{\mathrm{SOI}}$	dictionary matrix of the signal of interest, p. 36
$\mathscr{Z}(\cdot)$	z-score operator, p. 13

List of Abbreviations

ADC	analogue-to-digital converter, p. 9
ADS-B	automatic dependent surveillance-broadcast, p. 3
AGC	automatic gain control, p. 2
ATOA	Australia Telescope Online Archive, p. 27
AWGN	additive white Gaussian noise, p. 8
CDF	cumulative density function, p. 22
CW	continuous wave, p. 2
DFT	discrete Fourier transform, p. 12
DME	distance measure equipment, p. 3
ES	extended squitter, p. 26
FN	false negative, p. 15
FP	false positive, p. 15
GNSS	global navigation satellite systems, p. 1
GSNR	generalised SNR, p. 46
ICA	independent component analysis, p. 10
IF	instantaneous frequency, p. 3
IISM	ionised interstellar medium, p. 57
ISCAS	IEEE International Symposium on Circuits and Systems, p. 26
JNR	jammer-to-noise ratio, p. 10
JSR	jammer-to-signal ratio, p. 10

KL	Kullback-Leibler, p. 11
NF	notch filter, p. 2
NMF	nonnegative matrix factorisation, p. 4
NNDSVD	nonnegative double singular value decomposition, p. 11
PB	pulse blanking, p. 44
PCA	principal component analysis, p. 10
PPM	pulse position modulation, p. 26
PRN	pseudorandom noise, p. 46
RFI	radio frequency interference, p. 1
ROC	receiver operating characteristic, p. 16
SBNMF	semi-blind NMF, p. 38
SINR	signal-to-interference-plus-noise ratio, p. 61
SNR	signal-to-noise ratio, p. 10
SOI	signal of interest, p. 9
STFT	short-time Fourier transform, p. 2
S	squitter, p. 26
TAES	IEEE Transactions on Aerospace and Electronic Systems, p. 8
TF	time-frequency, p. 2
TN	true negative, p. 15
TP	true positive, p. 15
URSI GASS	General Assembly and Scientific Symposium of the International Union of Radio Science, p. 35

Chapter 1

Introduction

Global navigation satellite systems (GNSS) increasingly play an important role in functioning of our modern society. In addition to enabling the determination of a user's position at any location at any time around the world, they are used in transportation services enabling the real-time tracking of location of buses and other means of public transport [1–3]. Their low received signal power levels, however, make GNSS signals vulnerable to radio frequency interference (RFI) [4–7], which can either be generated by intentional sources such as low-cost jammers sold as "personal privacy" devices [4, 8], widely present around the globe [9], or by unintentional ones like the harmonics of UHF-, VHF-, and TV-signals [10, 11]. The presence of RFI may cause large biases in the navigation solution or even complete loss of tracking [5, 6, 12]. Therefore, the development of techniques that address the RFI vulnerability of GNSS receivers is of paramount importance.

In order to ensure the integrity of systems that rely on the services provided by the GNSS infrastructure, any RFI source must be detected quickly and preferably at power levels low enough so that it can be detected before disrupting the operation of the GNSS equipment [4, 13, 14]. The presence of RFI must then conveyed to the end-users, and/or used to trigger further downstream processing. In the context of RFI geo-location systems, detailed in [4] and references therein, the geo-localisation process can be triggered by the RFI detection unit before the operation of the GNSS receivers is impacted by the RFI, resulting in increased coverage area. Further, when a network of sensors is used to locate RFI, the received signal strengths at the sensors will vary across the network. Therefore, it may be necessary to use a sensor at some distance from the RFI source, with a low received signal level, in order to undertake interference geo-localisation. Hence, weak RFI detection and subsequent processing is important for RFI geo-location.

The GNSS interference detection techniques reported in the literature can be broadly divided into two main categories based on where they are applied in the receiver processing flow: RF analogue front-end, and Digital back-end based. In the former category, techniques such as automatic gain control (AGC) [15–17] are employed to detect RFI sources. The performance of AGC based approaches, however, degrades significantly while detecting low-power RFI sources [15, 16]. In the latter category, beamforming [12, 18–20] techniques are used. These approaches require antenna arrays and hence have increased hardware complexity and reduced flexibility.

The digital back-end based approaches can be further split into two subcategories: pre- and post-GNSS processing based. Considering the latter, although generally less effective than the pre-GNSS processing techniques, the RFI can be detected indirectly by monitoring the many observables generated from normal satellite and navigation processing. In this category, carrier-to-noise ratio (C/N_0) estimates have been used for RFI detection in [21, 22]. In the pre-GNSS processing category, there are a number of detection techniques that perform signal processing on the samples coming from the RF front-end. The RFI detection and mitigation can be performed in both time [7], [11], [23], [24, 25], and transformed [7], [26–28] domains. The RFI detection and mitigation can also be performed by using statistical analysis in the aforementioned domains [11, 29], [30]. Most time domain techniques are based on either the sample or power magnitudes of the received signal [24, 25]. Transform-domain methods aim to project the received signal in a domain such that the RFI's features are more prominent. For instance, narrowband signals yield peaks in the frequency domain [26], which makes them easy to detect. Further, chirp signals can be better described when working in the time-frequency (TF) plane via short-time Fourier transform (STFT) [31], Wigner-Ville decomposition [27] or wavelets [28], to name a few. Moreover, the RFI detection can also be performed by considering the statistical properties of the received signal. Such techniques usually rely on the Gaussianity tests of the received signal [11], and goodness-of-fit approaches in the time [32], and TF domains [29].

In the context of RFI mitigation for GNSS, a number of approaches have been reported in the literature to deal with RFI in GNSS receivers [25, 27, 30, 33, 34]. Pulse blanking methods, such as the one in [25], simply zero out samples of the received signal whose magnitude is greater than a predefined threshold. While simple to implement, these techniques are better suited to pulsed-type RFI, since they may zero out a considerable number of samples at the receiver in the case of long time duration interference, which may degrade the GNSS signal quality. Notch filter (NF)-based techniques [27] are typically employed to mitigate continuous-wave-(CW) and chirp-type RFI. In the case of CW-type RFI, NF-based approaches suppress the interference by filtering out the CW frequency component, whereas in the case of chirp-type RFI, they cancel out the effect of the RFI by "dechirping" the interference, resulting in a CW signal at DC, which is then filtered out. However, NF-based approaches are quite sensitive to the interference type and usually require *a priori* information about the RFI parameters such as the CW frequency or chirp instantaneous frequency (IF). In addition, while mitigating chirp-type RFI, a significant part of the GNSS signal spectrum along with the RFI may be filtered out as well. In a bid to alleviate this issue, the use of Kalman filters has been proposed in [30], whereby the interference samples are tracked for further subtraction in the time domain. This approach, however, is best suited to chirp-type RFI, requiring *a priori* IF information. Further, IF mismatches may result in large errors in the RFI signal estimation, which may lead to further GNSS signal degradation. Wavelet-based techniques [33, 34] have also been widely used in the literature to mitigate RFI. The wavelet transform decomposes the received signal into sub-bands with different frequency resolutions. In the presence of interference, the transformed-domain samples spread across the sub-bands, whose samples are set to zero if their magnitude is greater than a predefined threshold. The remaining samples are then resynthesized into the time domain. This method is more applicable to narrowband RFI since only a few sub-bands would be affected and hence fewer samples are discarded.

The presence of RFI signals is also a threat to radio astronomy observations. Due to very low power and diversified spectrum characteristics of the signals from outer space, modern radio telescopes provide high sensitivity and wide frequency coverage [35–37]. While the capability of observing cosmic events is enhanced, the susceptibility to RFI is also increased. Further, the presence of RFI may saturate the receiver's amplifier [38], resulting in data discarding, and may induce larger uncertainties [37, 39].

Many radio frequency systems transmit signals at the radio astronomy spectrum, such as mobile phone networks, GNSS, automatic dependent surveillance-broadcast (ADS-B) from aircraft [40], distance measuring equipment (DME) signals, just to mention a few. ADS-B is used by aircraft to broadcast key flight information in real time and it is required in the majority of airspace by aviation regulatory bodies such as the FAA, EuroControl and CASA. This makes ADS-B one of the major sources of RFI for radio astronomy applications [40]. Despite its importance to the aviation sector, this system may hamper the observation of pulsars or other short-duration astronomical events by concealing or even emulating their signature [39]. Therefore, it is of vital importance to detect this type of signal in the radio astronomy field, so that further RFI mitigation processing can be triggered.

In the context of radio astronomy applications, the RFI detection can be performed in two different stages: pre- and post-folding. The former detects interference using the raw input voltage levels, where the detectors are usually implemented in hardware [41]. In the post-folding case, the detection occurs after an integration process, where the time resolution is reduced [42], and may be considerably labour intensive [43]. Considering the pre-folding techniques typically employed for detection, they can be classified as threshold-based, where the raw input voltage levels are compared with a predefined threshold in the time, frequency, and time-frequency domains [41, 43], and statistical-based, which analyses statistical moments, such as kurtosis, to determine the presence of interference [41]. For RFI mitigation, the standard procedure widely employed in the consists in zeroing out some frequency channels corrupted by interference [44, 45]. However, this may discard useful astronomical data, hindering the observation of astronomical events. Moreover, the transient properties of some cosmic events, such as pulsars, may be affected [45].

1.1 Research Goals

The main objective of this research is to devise new solutions for RFI detection and mitigation, with focus on, but not limited to, GNSS and radio astronomy applications. Considering the former, the main goals are:

- Detect very weak RFI, considering narrowband and wideband sources, without prior knowledge about the RFI.
- Mitigate strong RFI sources with different time and frequency characteristics.

In the radio astronomy domain, this thesis addresses the following topics:

- Devise an ADS-B RFI detector using real-life signals.
- Mitigate RFI while not harming the signals from the outer space.

1.2 Thesis Contributions

In order to detect weak RFI, we propose a new RFI detection scheme based on nonnegative matrix factorisation (NMF) [46–48]. With the proposed approach, the spectral shape of the interference is estimated by applying NMF on the power spectrogram (modulus square of STFT) of the received signal. This shape is then compared with the spectrogram's time slices by means of a similarity function to detect RFI. Intuitively, in the absence of interference the received signal is solely comprised of noise and GNSS signals, which are well below the receiver noise floor, resulting in noise like spectral shape estimated via NMF. Hence, the similarity between the NMF estimated spectral shape and the spectrogram's time slices will be low. The proposed approach exploits this different similarity levels to detect the presence of interference. The performance and the computational complexity of the proposed approach is compared against a TF-domain statistical approach in [29], which we refer to as the baseline method, which used specific fine-tuned parameters for detecting narrow and wideband RFI types assuming *a priori* knowledge of the RFI source type. Results show the efficacy and the versatility of the proposed approach in detecting weak RFI with minimal tuning and computational complexity, albeit with slight reduction in detection performance for some scenarios when compared with [29].

In order to devise a mitigation technique robust to the RFI type and to the multiple interference corrupting the received signal in GNSS receivers, we propose a new framework based on NMF to suppress RFI. NMF [46, 47, 49] is employed in a multitude of applications, such as acoustic signal processing [49–51], where NMF is used for blind source separation. In the context of GNSS, our NMF-based method separates the RFI signals from the GNSS signals embedded in noise. The proposal can be tailored to the RFI at hand, where the interference type is assumed known beforehand (supervised NMF), or it can be completely blind, where no information about the RFI is provided (semi-blind NMF). Further, the proposed approach can mitigate multiple RFI signals concurrently without requiring the use of antenna arrays and associated array processing for null steering. Most techniques in the literature make use of antenna arrays for such [12, 20], which have increased hardware complexity and reduced flexibility. Results show that both supervised and semi-blind NMF frameworks are able to suppress distinct RFI types, such as DME signals, and CW and chirp interference with distinct bandwidths, outperforming pulse blanking techniques, broadly used for DME, techniques based on the notch and Kalman filters [27, 30], which are devised to work with chirp-type RFI, and a wavelet-based RFI method [33]. Further, we evaluate the performance in scenarios where the received signal is corrupted by both chirp- and CW-type RFI at the same time, with the NMF-based framework yielding superior results.

In the context of ADS-B detection for radio astronomy applications, we propose a pre-folding detector based on TF analysis. Since the ADS-B signal features are known *a priori*, it is possible to design a frequency template and compare it with the received signal's spectrogram time slices through a similarity function. The proposed technique relies on the fact that in the presence of ADS-B RFI larger similarity values are observed which can be used to detect the presence of interference. The performance of the proposed detector is assessed using signals captured by the Parkes radio telescope, situated in Parkes, Australia, which is continuously affected by signals from aircraft, due to its proximity to a nearby airport. The proposed method outperforms classic techniques widely used in the radio astronomy domain [41, 43] in terms of detection and false alarm rates.

Lastly, we propose three NMF-based frameworks for RFI mitigation using the

Parkes dataset. Building on our work in GNSS, we employ the supervised and semi-blind NMF, along with a template-based NMF, which uses the ADS-B's frequency template for further suppression. Also, we describe how to train NMF so that a better representation of ADS-B signals is achieved. We evaluate the performance over the spectrograms of the reconstructed signal of interest, with good mitigation performance. Further, we make use of software for radio astronomy to analyse the impacts of the NMF-based schemes on the pulsar observation.

1.3 Summary of Publications

This section lists published papers, and those under review which resulted from this thesis:

- **F.B. da Silva**, E. Cetin and W.A. Martins, "Radio frequency interference detection using nonnegative matrix factorization," *IEEE Transactions on Aerospace and Electronic Systems*, doi: 10.1109/TAES.2021.3111730. The main content of this paper is described in Chapter 2.
- **F.B. da Silva**, E. Cetin and W.A. Martins, "ADS-B signal detection via time-frequency analysis for radio astronomy applications," *2021 IEEE International Symposium on Circuits and Systems (ISCAS)*, Daegu, Korea, 2021, pp. 1–4. This paper forms Chapter 3.
- **F.B. da Silva**, E. Cetin and W.A. Martins, "DME Interference Mitigation for GNSS Receivers via Nonnegative Matrix Factorization," *2021 XXXIVth General Assembly and Scientific Symposium of the International Union of Radio Science (URSI GASS)*, Rome, Italy, 2021, pp. 1–4. Its main content is detailed in Chapter 4, with focus on DME RFI mitigation.
- **F.B. da Silva**, E. Cetin and W.A. Martins, "Radio Frequency Interference Mitigation via Nonnegative Matrix Factorization for GNSS," under review *IEEE Transactions on Aerospace and Electronic Systems*, The main content of this paper is described in Chapter 4, focusing on chirp- and CW-type interference.

In addition, the following papers whose main topics are not strictly related to this research but were accepted or published within the doctorate term:

- I.M. Quintanilha, V.R.M. Elias, **F.B. da Silva**, *et al.*, "A fault detector/-classifier for closed-ring power generators using machine learning," *Reliability Engineering & System Safety*, v. 212, 2021, pp. 107614.

- **F.B. da Silva**, W.A. Martins, “Semi-blind data-selective and multiple threshold Volterra adaptive filtering,” *Circuits, Systems, and Signal Processing*, v. 39, 2020, pp. 1509—1532.

1.4 Thesis Organisation

The thesis is organised as follows:

Chapter 2 describes the proposed NMF-based framework to detect narrow and wideband RFI in GNSS. It describes how NMF extracts information about the interference and details the proposed detector’s functional blocks.

In Chapter 3, we discuss RFI detection for radio astronomy applications. Building on the RFI detector for GNSS, we propose a detection technique for ADS-B interference from aircraft, which poses a considerable threat to astronomical observations. We also describe the characteristics of the dataset employed for detection, acquired from the Parkes radio telescope in Australia.

Chapter 4 details how NMF can be employed to mitigate RFI in the context of GNSS. Two different frameworks based on NMF are proposed: supervised NMF assumes prior knowledge about the RFI whereas its semi-blind counterpart does not require any information about the interference. Further, we detail each processing block within the interference mitigation scheme. First, we address the RFI issue considering DME signals.

In Chapter 5, we adapt the developed NMF-based schemes to mitigate RFI in GNSS to work with ADS-B signals. We also describe the signal processing performed in order to observe pulsars. Using the signals from the Parkes radio telescope dataset, we propose three different frameworks to suppress RFI, assessed via a qualitative analysis of the reconstructed spectrograms of the signal of interest.

In Chapter 6, we draw our conclusions about the techniques presented in this thesis and the goals that we have reached, along with future works that can make use of this document for further developments and enhancements.

Chapter 2

Radio Frequency Interference Detection for GNSS

In this chapter we propose a new framework based on the nonnegative matrix factorisation (NMF) to detect radio frequency interference (RFI), focusing on low-power continuous wave (CW) and chirp signals. Throughout this text, we describe the GNSS received signal and RFI models, which will be used in further chapters. Further, we describe NMF mathematical aspects and how it can be employed to detect RFI, with further detailing of the main processing blocks of the proposed detector. This work has been accepted for publication in *IEEE Transactions on Aerospace and Electronic Systems (TAES)* [52].

2.1 Received Signal Model

Defining $s_p(t) \in \mathbb{R}$ as the signal from the p^{th}-in-view satellite, $j_g(t) \in \mathbb{R}$ as the g^{th}-RFI signal (jammer), and $n(t) \in \mathbb{R}$ as an additive white Gaussian noise (AWGN), the received signal $r(t)$ can be described as

$$r(t) = \sum_{p=1}^{P} s_p(t) + \sum_{g=1}^{G} j_g(t) + n(t), \tag{2.1}$$

where P represents the number of in-view satellites. The received p^{th}-GNSS signal, $s_p(t)$, can be expressed as:

$$s_p(t) = \sqrt{2E_p} c_p(t - \tau_p) d_p(t - \tau_p) \cos\left(2\pi(f_{\text{c}} + f_{\text{d},p})t + \phi_p\right), \tag{2.2}$$

where E_p is the p^{th} GNSS signal power, $c_p(t)$ and $d_p(t)$ are the spreading code and navigation data of the p^{th}-satellite respectively; τ_p is the code delay introduced by the propagation channel; f_{c} denotes the carrier frequency; $f_{\text{d},p}$ and ϕ_p are the carrier

Doppler frequency and phase respectively.

In the receiver's front-end, the received signal is down-converted into in-phase and quadrature components through two local oscillators, whose phases are 90° degrees apart. Next, sampling and digitisation stages are performed by an analogue-to-digital converter (ADC) with sampling frequency F_{s}, generating the baseband signal $r[i] \in \mathbb{C}$, described as

$$r[i] = \sum_{p=1}^{P} s_p[i] + \sum_{g=1}^{G} j_g[i] + n[i], \tag{2.3}$$

where

$$s_p[i] = \sqrt{2E_p} c_p \left[i - \lfloor \tau_p F_{\mathrm{s}} \rceil\right] d_p \left[i - \lfloor \tau_p F_{\mathrm{s}} \rceil\right] \mathrm{e}^{\mathrm{j}\left(2\pi f_{\mathrm{d},p} \frac{i}{F_{\mathrm{s}}} + \phi_p\right)}. \tag{2.4}$$

where $\lfloor \cdot \rceil$ rounds to the nearest integer. Further, (2.3) can be written in vector form as

$$\mathbf{r}[i] = \left[\, r[i] \, r[i-1] \, \cdots \, r[i-Q+1] \,\right]^{\mathsf{T}}, \tag{2.5}$$

where Q denotes the sampled data-length. As seen in (2.3), the received signal can be interpreted as the sum of an undesired term, i.e., the jamming signals, and the signal of interest (SOI), composed by the spreading codes embedded in noise.

Interference sources can be classified as narrowband and wideband with respect to the bandwidth of the desired GNSS signal. Narrowband interference sources occupy much less frequency spectrum than the satellite signals, and typically originate from the harmonics of other radio or communication systems such as UHF, VHF, and TV [11]. Continuous wave (CW) interference is the narrowest type of interference consisting of a single un-modulated carrier. Wideband interference sources, on the other hand, have spectral energy spread over a wider bandwidth of which majority is captured by the GNSS receiver front-end. They are the most common interference signal types emitted from commercial jammers sold as "personal privacy" devices [8], and are normally represented as chirps [9], whose main features such as the period T and bandwidth B, are given by a sawtooth function [8]. In this work, both CW- and chirp-type type RFI are considered and modelled using a unified framework, which can be described as

$$j[i] = A[i]\mathrm{e}^{\mathrm{j}2\pi F[i] i}, \ \mathrm{j}^2 = -1, \tag{2.6}$$

where

$$F[i] = \frac{1}{F_\mathrm{s}} \left[B \left(\frac{i}{TF_\mathrm{s}} - \left\lfloor \frac{i}{TF_\mathrm{s}} \right\rfloor \right) + f_\mathrm{off} \right], \tag{2.7}$$

with $A[i]$ representing the instantaneous amplitude, $\lfloor \cdot \rfloor$ denoting rounding to the nearest integer towards $-\infty$, and f_off the frequency offset from DC. Figure 2.1 describes the instantaneous frequency F as a function of time for chirp-type RFI signals. When f_0 denotes a given frequency component and B is set to zero, (2.6) degenerates into a CW-type RFI. Considering the noise variance as σ^2, and the total GNSS signal power as E, the signal-to-noise ratio (SNR) can be expressed as E/σ^2. Analogously, assuming the total jammer power as A, the jammer-to-noise ratio (JNR) can be defined as $\mathrm{JSR} = A/\sigma^2$, with the jammer-to-signal ratio (JSR) being described as $\mathrm{JSR} = A/E$.

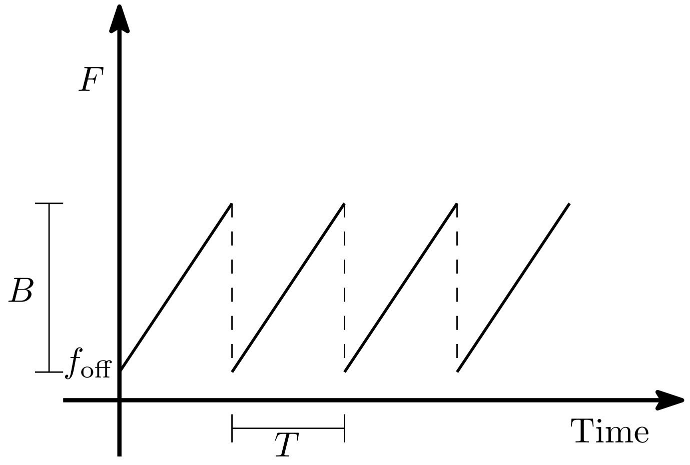

Figure 2.1: Instantaneous frequency vs. time of a typical chirp signal.

2.2 Nonnegative Matrix Factorisation

The NMF is a technique employed to extract features from a set of nonnegative data represented by $\mathbf{X} \in \mathbb{R}_+^{N \times M}$. NMF was first proposed in [46], and became quite popular after the work in [47]. NMF works as an alternative to other low-rank decomposition techniques such as principal and independent component analysis, PCA and ICA respectively. Unlike PCA and ICA, however, NMF's inherent nonnegativeness constraint allows for physical interpretation of the resulting decomposed matrices. Many problems in the literature such as acoustic source separation [49, 50, 53–55], and image processing [47, 56, 57], have input data matrices whose entries are nonnegative. For instance, when $\mathbf{X}$ is a power spectrogram, NMF decomposes it as a product of two lower-rank matrices: $\mathbf{X} \approx \mathbf{WH}$, $\mathbf{W} \in \mathbb{R}_+^{N \times S}$, $\mathbf{H} \in \mathbb{R}_+^{S \times M}$, with

$S < \min(N, M)$, where $\mathbf{W}$ and $\mathbf{H}$ represent time and frequency information respectively, and S denotes the predefined number of components. The decomposition is achieved by means of an optimisation problem given as:

$$\begin{aligned} &\min_{\mathbf{W},\mathbf{H}} \mathcal{L}\left(\mathbf{X}, [\mathbf{W}, \mathbf{H}]\right) \\ &\text{subject to}\, \mathbf{W} \succeq 0, \mathbf{H} \succeq 0, \end{aligned} \tag{2.8}$$

where $\mathcal{L}(\cdot)$ represents a generic distance function between $\mathbf{X}$ and $[\mathbf{W}, \mathbf{H}]$, and the symbol "$\succeq$" denotes entry-wise nonnegativeness. This distance is usually measured by means of the β-divergence. Considering a,$b \in \mathbb{R}_+$, the β-divergence between a and b can be described as [58]

$$d_\beta(a|b) = \begin{cases} \frac{1}{\beta(\beta-1)}\left(a^\beta + (\beta-1)b^\beta - \beta a b^{\beta-1}\right) & \text{if } \beta \in \mathbb{R}\backslash\{0, 1\}, \\ a(\log a - \log b) + (b - a) & \text{if } \beta = 1, \\ \frac{a}{b} - \log\frac{a}{b} - 1 & \text{if } \beta = 0, \end{cases} \tag{2.9}$$

The most popular β-divergences are the Euclidean ($\beta = 2$), generalised Kullback-Leibler (KL) divergence ($\beta = 1$), and Itakura-Saito ($\beta = 0$) distances [53, 59]. The update equations for the matrices $\mathbf{H}$ and $\mathbf{W}$ as a function of β can be described as [58]

$$\mathbf{H}[k+1] = \mathbf{H}[k] \otimes \left[\frac{\mathbf{W}^\intercal[k]\left[(\mathbf{W}[k]\mathbf{H}[k])^{\circledcirc(\beta-2)} \otimes \mathbf{X}\right]}{\mathbf{W}^\intercal[k](\mathbf{W}[k]\mathbf{H}[k])^{\circledcirc(\beta-1)}}\right], \tag{2.10}$$

$$\mathbf{W}[k+1] = \mathbf{W}[k] \otimes \left[\frac{\left[(\mathbf{W}[k]\mathbf{H}[k+1])^{\circledcirc(\beta-2)} \otimes \mathbf{X}\right]\mathbf{H}^\intercal[k+1]}{(\mathbf{W}[k]\mathbf{H}[k+1])^{\circledcirc(\beta-1)}\mathbf{H}^\intercal[k+1]}\right], \tag{2.11}$$

where $\otimes$ and $\circledcirc$ represent the element-wise product and exponentiation operators respectively, and the division between the numerator and denominator in (2.10) and in (2.11) is also performed element-wise. It is worth noting that the initialisation of $\mathbf{W}$ and $\mathbf{H}$ can be performed in several ways e.g. nonnegative random initialisation, and nonnegative double singular value decomposition (NNDSVD) [60].

2.3 NMF-Based RFI Feature Extraction

In the context of RFI detection, $\mathbf{X}$ represents the power spectrogram matrix of the received signal containing the GNSS signals contaminated by RFI and AWGN as given in (2.3). Setting $S = 1$ results in $\mathbf{W}[k]$ and $\mathbf{H}[k]$ degenerating to vectors $\mathbf{w}[k] \in \mathbb{R}^{N\times 1}$ and $\mathbf{h}[k] \in \mathbb{R}^{1\times M}$, which we will refer to as dictionary ($\mathbf{w}$) and activation ($\mathbf{h}$) vectors respectively.

In order to demonstrate the physical correspondence of $\mathbf{w}$ and $\mathbf{h}$, Figure 2.2 depicts the spectrogram of a 100 μs-length chirp signal with period $T = 8.62$ μs, frequency offset $f_0 = 2$ MHz, and bandwidth $B = 8$ MHz. The JNR is set to 10 dB, while the spectrogram parameters are set as follows: $N = 64$ discrete Fourier transform (DFT) bins, rectangular window length $L = N = 64$, and $N - 1$ overlapping samples between consecutive windows. It is worth highlighting that zero valued samples were concatenated prior and after the chirp signal to emulate the onset (25 μs) and offset (125 μs) of the interference source. Figures 2.3(a) and 2.3(b) show the resulting dictionary and activation vectors.

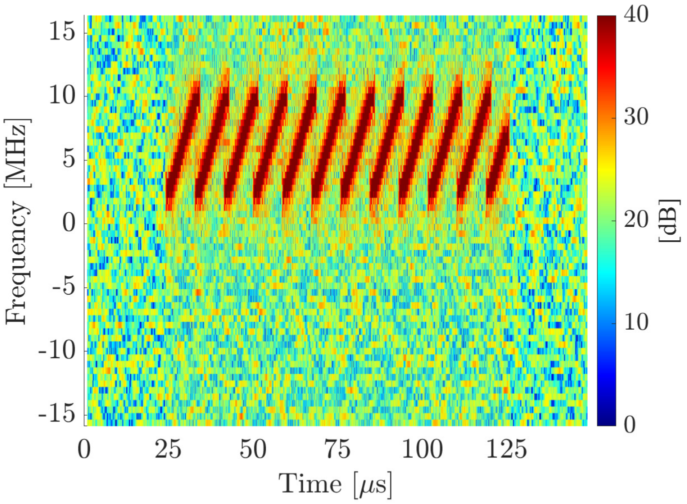

Figure 2.2: Spectrogram of chirp signal with period $T = 8.62$ μs, and bandwidth $B = 8$ MHz.

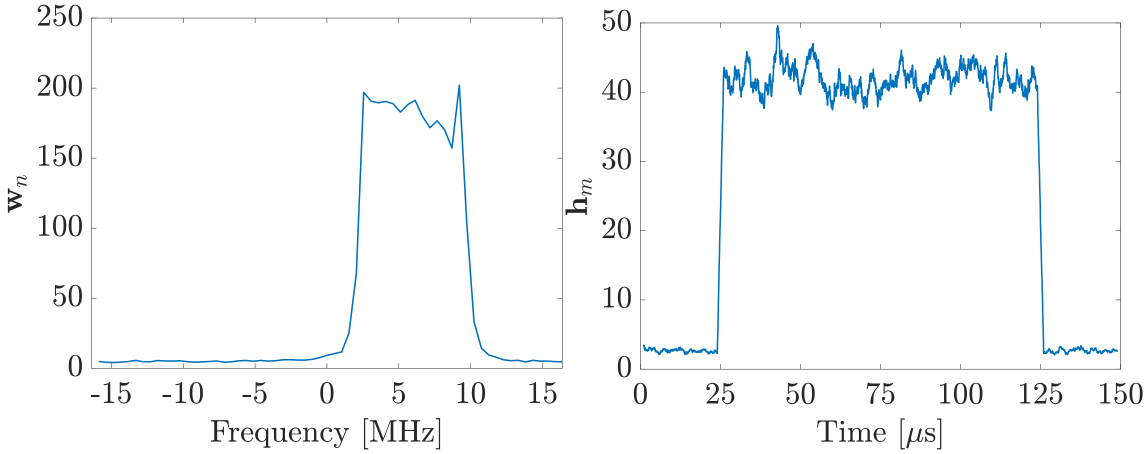

(a) NMF dictionary vector ($\mathbf{w}$).

(b) NMF activation vector ($\mathbf{h}$).

Figure 2.3: NMF output vectors for a chirp signal with period $T = 8.62$ μs, and bandwidth $B = 8$ MHz.

As can be observed, Figure 2.3(a) precisely describes the chirp signal's bandwidth information, which ranges from 2 – 10 MHz, while Figure 2.3(b) accurately represents the chirp signal's time properties. This information can be exploited for RFI detection using NMF, and in the next section we describe an NMF-based RFI detector.

2.4 NMF-Based RFI Detection

The main contribution of this work relies on using the features extracted from the received signal by NMF to detect the presence of RFI. In the following, each of the functional blocks of the proposed NMF-based detector are detailed. However, prior to this, some mathematical definitions should be stated. Considering N DFT points, M time instants, a window $f[i]$ with length L, and hop size of R samples, the $(n{,}m)^{\text{th}}$-element of short-time Fourier transform (STFT) matrix $\mathbf{S}$ is defined as

$$[\mathbf{S}]_{n,\,m} = \sum_{l=0}^{L-1} r[mR + l] f[l] \mathrm{e}^{-\mathrm{j}\frac{2\pi}{N}nl}, \tag{2.12}$$

with the $(n{,}m)^{\text{th}}$-element of the power spectrogram matrix $\mathbf{X}$ computed as

$$[\mathbf{X}]_{nm} = \left| \, [\mathbf{S}]_{n,\,m} \right|^2. \tag{2.13}$$

Thus, $\mathbf{X} = [\,\mathbf{x}_1\,\mathbf{x}_2\,\cdots\,\mathbf{x}_M\,]$, where the n^{th}-entry of $\mathbf{x}_m \in \mathbb{R}_+^N$ is $[\mathbf{X}]_{nm}$ in (2.13).

As discussed in Section 2.3, the NMF method generates the output vectors $\mathbf{w}$ and $\mathbf{h}$ according to the input matrix $\mathbf{X}$. The proposed RFI detection technique is performed using the levels of similarity between $\mathbf{w}$ and the m^{th}-column, $m \in \{1, 2, \ldots, M\}$, of $\mathbf{X}$. In order to avoid a biased similarity evaluation, the *z-score* [61] normalisation process is applied, which removes the sample mean of a given data, followed by scaling by its standard deviation. This process, applied to vector $\mathbf{a}$, can be expressed as:

$$\mathcal{Z}(\mathbf{a}) = \frac{\mathbf{a} - \mu_a \cdot \mathbf{1}_{N\times 1}}{\sigma_a}, \tag{2.14}$$

where μ_a and σ_a denote the sample mean and standard deviation of $\mathbf{a}$ respectively. Accordingly, the z-score processing is also performed over $\mathbf{w}$, generating $\overline{\mathbf{w}} = \mathcal{Z}(\mathbf{w})$, and over each column of $\mathbf{X}$ which yields $\overline{\mathbf{X}} = [\,\overline{\mathbf{x}}_1\,\overline{\mathbf{x}}_2\,\cdots\,\overline{\mathbf{x}}_M\,]$. The similarity evaluation is done using the *cosine* between vectors, which has low computational complexity and does not require setting predefined parameters. It is worth noting that other similarity functions such as Gaussian and polynomial kernels [62] can also be employed. However, these have higher computational burden and require parameter setting. We have carried out simulations employing these kernels as well, with resulting performances very akin to that of the cosine function and hence they were not further considered. Thus, the similarity between $\overline{\mathbf{x}}_m$ and $\overline{\mathbf{w}}$ is defined as

$$s_m = \frac{\overline{\mathbf{x}}_m^{\intercal}\overline{\mathbf{w}}}{\|\overline{\mathbf{x}}_m\|\|\overline{\mathbf{w}}\|}, \tag{2.15}$$

with $\mathbf{s} = [\, s_1\, s_2\, \cdots\, s_M\,]^{\intercal}$. The elements of $\mathbf{s}$ tend to 1 as more identical $\overline{\mathbf{w}}$ is to $\overline{\mathbf{x}}_m$, and tend to 0 otherwise. In the presence of RFI, the shape of $\overline{\mathbf{w}}$ is well-defined, as observed in Figure 2.3(a), resulting in high similarity levels. On the other hand, in the absence of interference, the columns of the power spectrogram and $\overline{\mathbf{w}}$ tend to be noise-like with very low similarity levels. Hence, by using a detection threshold $\bar{\gamma}$, the presence of RFI can be detected as:

$$d_m = \begin{cases} 1, & \text{if } s_m > \bar{\gamma} \text{ (RFI present)}, \\ 0, & \text{otherwise (no RFI present)}. \end{cases} \tag{2.16}$$

with $\mathbf{d} = [\, d_1\, d_2\, \cdots\, d_M\,]^{\intercal}$. The detection threshold $\bar{\gamma}$ can be chosen in a variety of ways. For instance, it can be set according to a predefined level of false alarm rate, or by minimising a figure of merit, such as accuracy, or precision. The choice of $\bar{\gamma}$ is discussed further in Section 2.5.1.

Since the detection is performed column-wise on the power spectrogram, in low-JNR scenarios the entries of $\mathbf{d}$ tend to present spikes i.e. abrupt variations from 0 to 1 and vice-versa, even though the RFI source is present across all the M spectrogram columns. In order to address this issue, a majority voting scheme is applied, which is implemented as the sample median of $\mathbf{d}$, defined as $\mathcal{M}(\mathbf{d})$. Hence, if more than half of the elements of $\mathbf{d}$ are comprised of 1s, the proposed detector indicates the presence of interference. The functional block diagram of the proposed NMF-based RFI detection is given in Figure 2.4. It is worth mentioning that the vector $\mathbf{h}$ can also be employed for detecting RFI. However, based on prior simulations, the detection performance in low-JNR scenarios was poor, which motivated the use of the cosine similarity along with the *z-score* scheme and the median operator. Further, vectors $\mathbf{w}, \mathbf{h}$ are by-products of the NMF decomposition, which is not unique. Considering $\delta \in \mathbb{R}_+$ as a scaling factor, the power spectrogram matrix $\mathbf{X}$ can be decomposed as $\mathbf{X} \approx \mathbf{wh} = \left(\frac{\mathbf{w}}{\delta}\right)(\mathbf{h}\delta) = (\delta\mathbf{w})\left(\frac{\mathbf{h}}{\delta}\right)$. Therefore, the nonuniqueness of NMF impairs the detection threshold setting.

2.5 Performance Assessment

In this section the performance of the proposed technique is evaluated and compared against the baseline method described in [29]. This technique, to the best of our knowledge, is the state-of-the-art method for detection in low-JNR scenarios,

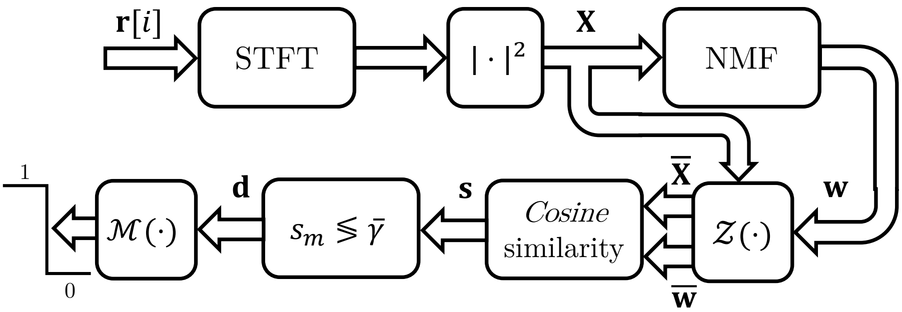

Figure 2.4: Block diagram of the proposed detection framework.

which is why it was chosen as baseline for performance comparison. The method in [29] evaluates the statistical distribution of the spectrogram's frequency slices via a goodness-of-fit test. It must be mentioned that the proposed technique is compared against the block-wise version of the method given in [29] where the STFT is evaluated using non-overlapped samples. To verify the effectiveness of the proposed method, chirp signals with varying bandwidths and periods along with CW signals are used as RFI sources. The chirp parameters in this work follow the most common RFI captured in different regions of the world, as reported in [9], thus well representing real jamming signals. Further, different JNR scenarios are considered, which allows for performance evaluation under various noisy environments. A qualitative analysis of the computational complexity of the proposed and baseline techniques is also presented.

2.5.1 Figures of Merit

In order to properly assess the performance of the proposed technique and contrast it to that of the baseline's, one needs to quantify it by means of figures of merit. Considering a detection application, which is regarded as a binary problem (*RFI source present or absent*), the figures of merit are usually described as a function of the following conditions:

- True positive (TP): if detector's output indicates the presence of interference when there are RFI samples in the received signal;
- True negative (TN): if detector's output indicates absence of interference when there are no RFI samples in the received signal.

Conversely, the false positive (FP), and false negative (FN) conditions can also be defined. Table 2.1 summarises the relationship between the detector's output (predicted condition) and the actual condition. In Boolean representation, the positive and negative conditions are associated with the values 1 and 0 respectively.

Table 2.1: Relation between the actual and predicted conditions for a binary detector.

		True condition	
		Positive	**Negative**
Detector's output	**Positive**	TP	FP
	Negative	FN	TN

Subsequently, the true positive rate (TPR), which is defined by the ratio between the true positive occurrences and sum of all positive occurrences (TPs and FNs) is given as:

$$\mathrm{TPR} = \frac{\sum \mathrm{TP}}{\sum \mathrm{TP} + \sum \mathrm{FN}}. \tag{2.17}$$

Analogously, the false positive rate (FPR) can be defined as:

$$\mathrm{FPR} = \frac{\sum \mathrm{FP}}{\sum \mathrm{FP} + \sum \mathrm{TN}}. \tag{2.18}$$

Hence, the performance of the detector can be assessed by means of true positive and false positive rates, which, in RFI detection applications, are also referred to as detection rate (R_{d}) and false alarm rate (R_{fa}) respectively. In this sense, the receiver operating characteristic (ROC) curve is one of the most common tools used to analyse the relationship between R_{fa}, R_{d} and the detection threshold $\bar{\gamma}$ for a given JNR. Also, it is possible to define the Euclidean distance between a given point of the ROC curve and the optimal detection point ($R_{\mathrm{d}} = 1, R_{\mathrm{fa}} = 0$). Thus, the minimum distance to the optimal point is described as [52]

$$C_{\min} = \min_{\bar{\gamma}} \sqrt{R_{\mathrm{fa}}^2 + (1 - R_{\mathrm{d}})^2}. \tag{2.19}$$

We evaluate the performance of the detectors in terms of estimated R_{fa} and R_{d} as a function of the detection threshold $\bar{\gamma}$ by analysing the ROC curve. Each data point of the ROC curve corresponds to a value of false alarm and detection rates for a given threshold. The figure of merit employed in this work to compare different detectors is the $C_{\min}$, which is the minimum distance from the ROC curve to the optimal detection point ($R_{\mathrm{d}} = 1$, $R_{\mathrm{fa}} = 0$), i.e., perfect detection without false alarms. In effect, $C_{\min}$ is a way to assess the performance via the ROC information (and consequently the corresponding values of R_{d} and R_{fa}). $C_{\min}$ is adopted to simplify the analysis considering different scenarios, such as distinct JNR levels and RFI-types.

2.5.2 Experimental Setup

The experimental setup used follows the one in [29]. The sampling frequency employed is $F_\mathrm{s} = 32.768$ MHz, the CW interference signal frequency is fixed at $F_\mathrm{s} \times 0.12 = 3.93$ MHz, while the chirp interference bandwidth varies from $B \in \{2, 8, 14\}$ MHz, and period from $T \in [8.62, 17.50]\,\mu$s, with step-size of $2.96\,\mu$s. A set of five GPS signals with signal-to-noise ratios (SNRs) of -25 dB is employed in the simulations. The JNR is varied between -25 to 0 dB, with the detection threshold for the proposed technique varying from $\bar{\gamma} \in [0, 0.2]$, and the baseline's one ranging from $\bar{\gamma} \in [10^{-8}, 10^{-2}]$. Further, 1,000 independent runs are used to compute the false alarm and detection rates, with each run using 4,096 complex baseband samples to calculate the power spectrogram of the received signal. The C_min evaluation is repeated for 10 Monte Carlo loops, so that the statistical properties of the detection results can be assessed.

For the STFT computation, a rectangular window of length $L = 16$ is used for the proposed technique providing a reasonable performance for both CW- and chirp-type interference, whereas the baseline technique presented in [29], wherein the RFI type is assumed to be known *a priori*, used fine-tuned window length of $L = 19$ for CW and $L = 3$ for chirp-type interference respectively. To provide a fair comparison, both window lengths were used i.e. $L \in \{3, 19\}$ while evaluating the performance of the baseline technique considering both interference types.

The number of DFT points is set to $N = 16$, for the proposed technique, and $N \in \{1365, 215\}$ for $L \in \{3, 19\}$ respectively for the baseline technique. In addition, the hop size is set to $R = 1$ and $R = L$ for the proposed and the baseline techniques respectively. For the proposed technique, the window length L was chosen based on simulations using a similar setup as previously described in this section, with $L \in \{8, 16, 32, 64, 128\}$. Figure 2.5 shows the C_min levels for CW- and chirp-type interference signals. As it can be observed, the value of L that yields the lowest C_min values for CW is $L = 128$. However, this L value leads to the highest C_min levels for chirp-type interference signals. For chirp-type RFI, the window lengths that lead to the lowest C_min values are $L \in \{16, 32\}$. Nonetheless, the use of $L = 16$ results in a slightly degraded performance for CW, whereas $L = 32$ yields increased computational complexity when compared to $L = 16$. Considering the performance for both RFI types, and the computational burden trade-off, $L = 16$ is chosen as the window length. The number of overlapping samples is chosen as $L - 1$ so that a good time resolution can be achieved to appropriately represent the chirp-type RFI in the time-frequency domain. Also, the number of DFT points was chosen as $N = L$ to minimise the computational burden. Regarding the baseline method, the parameters were set as in [29].

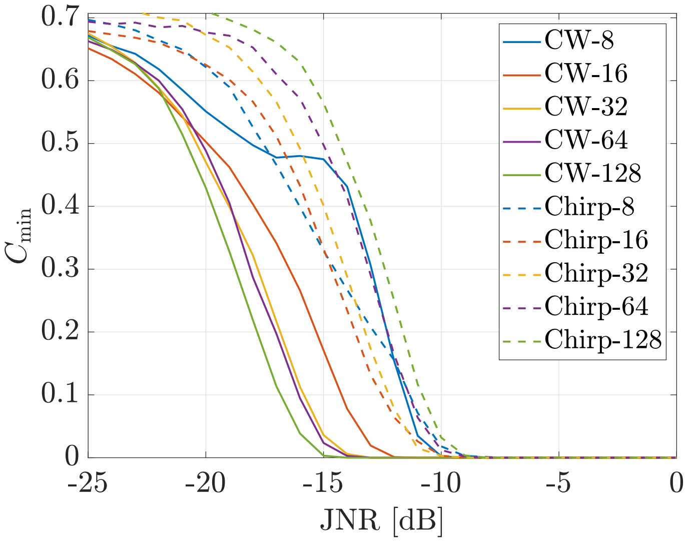

Figure 2.5: C_{min} values for different L's for both CW- and chirp-type RFI.

Lastly, regarding the NMF parameters, the *Kullback-Leibler divergence* cost function is used, with **w** and **h** randomly initialised. The proposed and the baseline techniques are hereafter referred to as NMF-based, and statistical-based respectively.

2.5.3 CW-type RFI

The ROC curves for -15 dB JNR, which represents a quite low JNR scenario, are depicted in Figure 2.6, where the dashed line represents the case of $R_{\text{fa}} = R_{\text{d}}$, i.e. a random guess. As shown, the proposed NMF-based technique outperforms the statistical-based detector in terms of $R_{\text{d}}, R_{\text{fa}}$ when $L = 3$, which is the fine-tuned parameter value for a chirp-type RFI for [29], is used and yields degraded performance when $L = 19$, which is the fine-tuned parameter value for a CW-type RFI for [29], is used. It can be observed that, for the statistical-approach, the performance degrades significantly when L tuned for the chirp-type RFI is used for detecting the presence of a CW-type interference. Results in terms of C_{min} considering R_{d} and R_{fa} values for various JNR levels are shown in Figure 2.7, with the sub-figure depicting the performance from -17 to -13 dB JNR, and the error bars denoting the standard deviation of C_{min} calculated across the Monte Carlo loops. As it can be observed, the proposed technique yields lower C_{min} values for all of the JNR values when compared to the statistical-based one for $L = 3$. Considering $L = 19$, it outperforms the statistical-based one for JNR levels -25 to -18 dB, and performs slight worse for other JNR values. Further, for JNR values -25 to -18 dB, the proposed technique has lower C_{min} values than the statistical one regardless of the window length used.

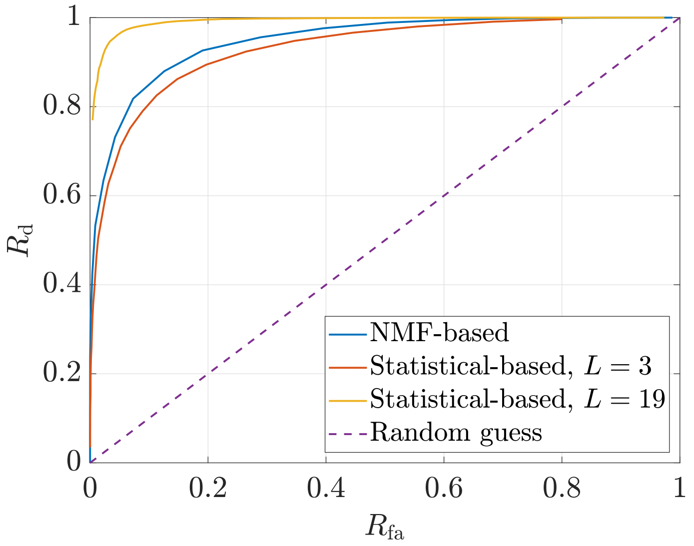

Figure 2.6: ROC curves for the NMF- and statistical-based detectors for different L's under -15 dB JNR for CW-type interference signal.

2.5.4 Chirp-type RFI

The performance of the proposed NMF-based technique is evaluated for chirp type RFI with varying period and bandwidths under a variety of JNR levels.

Detection vs. Period

Figure 2.8 shows the performance in terms of C_min for the NMF-based detector considering different chirp period values for $B = 14$ MHz, whereas Figure 2.9 depicts the baseline statistical-based technique's performance using $L = 3$ for the same bandwidth value. It can be observed that the performance of both techniques is not impacted by varying chirp period since, for each JNR, the C_min values are roughly constant for different periods. In effect, given that the number of samples employed to evaluate the spectrogram is fixed, varying chirp period simply alters the number of replicas observed in the spectrogram. Moreover, the period-invariant behaviour can be explained by the high time resolution provided by the short-length windows employed in both techniques ($\{0.09, 0.48\}\,\mu$s, for $L \in \{3, 16\}$ respectively).

Detection vs. Bandwidth

In this subsection the performance of the proposed technique is compared with baseline's considering a wide range of bandwidths. Figures 2.10(a) – (c) display the ROC curves for JNR $= -15$ dB for a bandwidth ranging from 2 – 14 MHz, and $T = 8.62\,\mu$s. It can be observed that, except for $B = 2$ MHz, the NMF-based proposed technique outperforms the baseline statistical-based one when $L = 19$, which implies that larger detection rates can be achieved at smaller false alarm

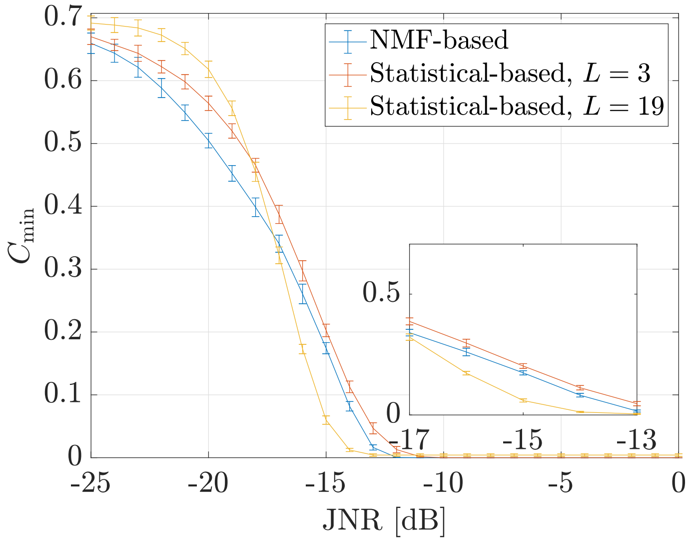

Figure 2.7: $C_{\min}$ for different JNR levels for the proposed and baseline techniques considering various window lengths for CW-type interference signal.

rates. Further, considering $L = 3$, which is the optimal window length for the baseline technique for a chirp-type RFI, the performance of the proposed technique is slightly better for $B = 2$ MHz, slightly degraded for $B = 8$ MHz and degraded for $B = 14$ MHz when compared with that of the baseline's.

Figures 2.11(a) – (c) display the $C_{\min}$ values for varying bandwidths. Overall, as the bandwidth increases, the performance of both techniques worsens. For instance, considering Figure 2.11(a), the $C_{\min}$ values for the proposed technique are quite similar to the baseline's, whereas in Figures 2.11(b), and 2.11(c) the NMF-based detector outperforms its statistical counterpart for $L = 19$ and presents similar or reasonably close performance for $L = 3$. It should be highlighted that the proposed detector yields good performance for a given L regardless of the interference type. On the other hand, the performance of the statistical-based detector is considerably affected by the window length as it can be seen from the corresponding $C_{\min}$ values for $L = 3$ and $L = 19$ in Figures 2.11(a) – (c). In fact, when the optimal window length value for CW-type RFI of $L = 19$ is used for chirp-type RFI, the performance of the baseline method degrades significantly, highlighting the sensitivity of the baseline method to the choice of L, hence, its reliance on *a priori* knowledge of the RFI type. This occurs due to the fact that the statistical-based detector relies on using short window length L when computing the spectrogram, resulting in lower frequency resolution and spectral leakage. This alters the statistical properties of the frequency slices of the spectrogram, thereby, the detection capability of the baseline method.

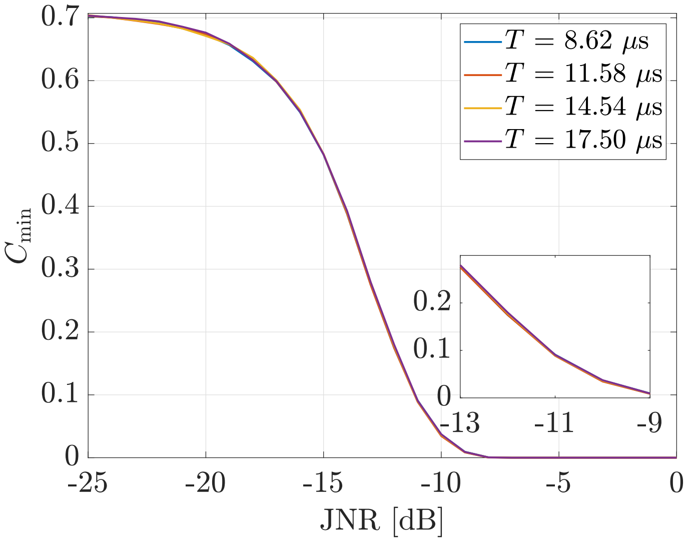

Figure 2.8: NMF-based detector C_{min} values for different periods considering chirp-type interference signal for $B = 14$ MHz.

Detection vs. Fixed Sweep Rate

The detection performance can also be analysed by fixing the chirp sweep rate, defined as $S_{\text{w}} = \frac{B}{T}$. In Section 2.5.4 we describe the performance for a fixed bandwidth, while varying the period and sweep rate. The results in Subsection 2.5.4 consider a single T with varying B and S_{w} values. In this subsection, we describe the results considering a fixed sweep rate, with distinct B and T values. Figure 2.12 and Figure 2.13 show the ROC curves for $B = 8$ MHz, $T = 8$ μs, and $B = 10$ MHz, $T = 10$ μs respectively, with Figure 2.14 and Figure 2.15 depicting the corresponding results in terms of C_{min}. Similar to what was observed in the previous subsections, the proposed technique outperforms the baseline for $L = 19$, and leads to similar performance for $L = 3$. In fact, as concluded in Subsection 2.5.4, both techniques are robust to variations of T, with B being the major RFI parameter. Hence, the fixed sweep rate and bandwidth analyses yield very similar results and discussions.

In general, the NMF-based detection technique presents good performance for both RFI types. In most cases, it outperforms the baseline method when the fine-tuned window length L for a specific RFI type is not used, highlighting the robustness of the proposed technique to the RFI type.Further, considering the chirp-type RFI results, the proposed technique is able to detect interference with time-varying characteristics. This is brought about by using the time-frequency representation of the received signal and the extraction of its features by NMF.

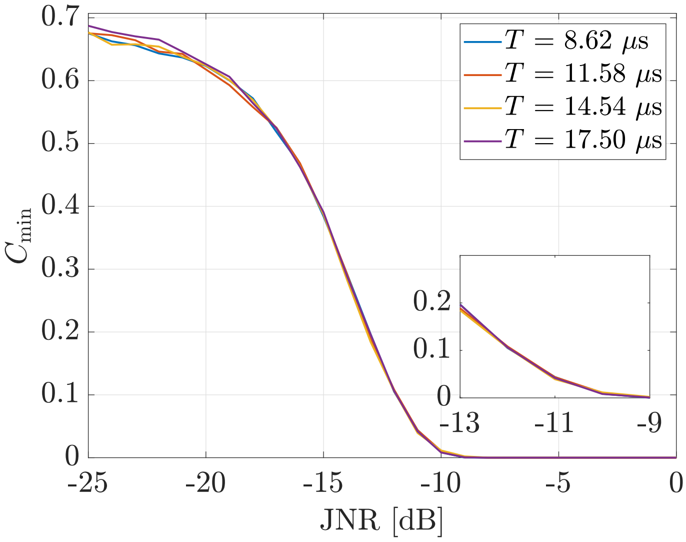

Figure 2.9: Statistical-based detector C_{min} values for different periods considering chirp-type interference signal for $B = 14$ MHz.

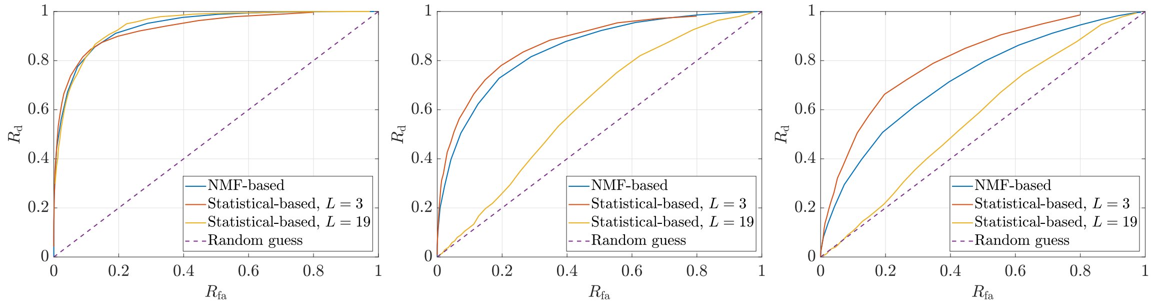

(a) $B = 2$ MHz.

(b) $B = 8$ MHz.

(c) $B = 14$ MHz.

Figure 2.10: ROC curves for chirp interference signal, JNR $= -15$ dB, $T = 8.62\,\mu$s, and various bandwidths for the NMF- and statistical-based detectors.

2.5.5 Computational Complexity

Computational complexity is another key metric when comparing the proposed and the baseline techniques. Considering the statistical-based approach, since it relies on a goodness-of-fit test, it involves sorting operations and cumulative density function (CDF) estimation, thus, it is not straightforward to analyse its computational complexity via traditional number of additions and multiplications. Therefore, the computational complexity comparison is performed qualitatively in terms of execution time. This assessment was carried out on a PC with the following specifications: Intel© Core™ i5-8350U, 8 GB of RAM, and 256 GB-SSD storage. Table 2.2 displays the average execution time considering 100 independent runs of the NMF- and statistical-based methods. As shown, the proposed technique's execution time is much lower than the baseline's. For instance, for $L = 3$, which yields the best results for the statistical-based detector for a chirp-type RFI, the corresponding execution time is roughly 35× larger than that of the NMF-based one, even though

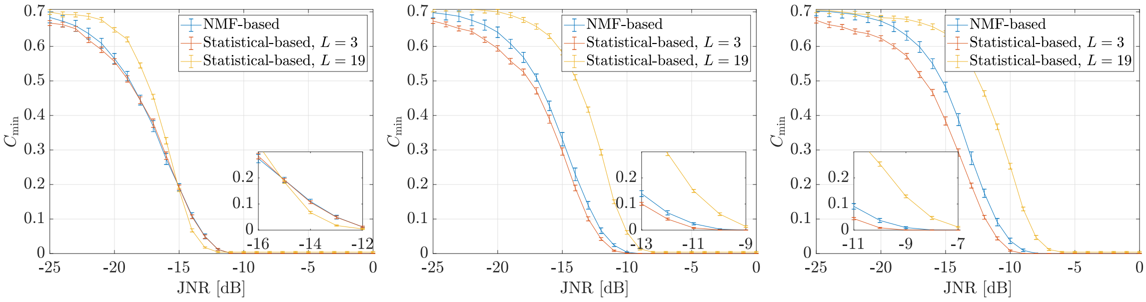

(a) $B = 2$ MHz. (b) $B = 8$ MHz. (c) $B = 14$ MHz.

Figure 2.11: $C_{\min}$ values for chirp-type interference signal, $T = 8.62\,\mu$s, and various bandwidths for the NMF- and statistical-based detectors.

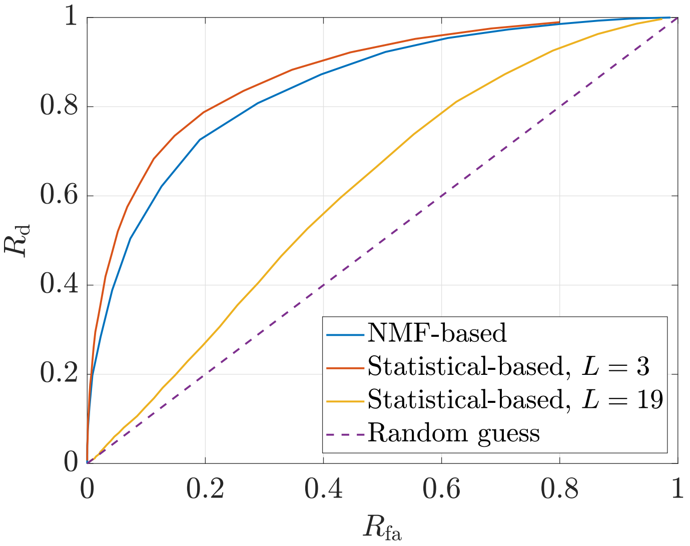

Figure 2.12: ROC curve for the NMF- and statistical-based detectors for different L's under -15 dB JNR for $B = 8$ MHz, $T = 8$ μs.

their performances are very similar. As for $L = 19$ the computational complexity of the baseline technique reduces but it is still considerably larger than that of the proposed NMF-based technique's.

Table 2.2: Average execution time of the NMF- and statistical-based techniques.

	Execution time [ms]
NMF-based	**13.96**
Statistical-based, $L = 3$	496.01
Statistical-based, $L = 19$	57.90

2.6 Conclusions

The results of Section 2.5 show that the proposed NMF-based technique provides high levels of detection rate with low levels of false alarm rate, even in highly noisy

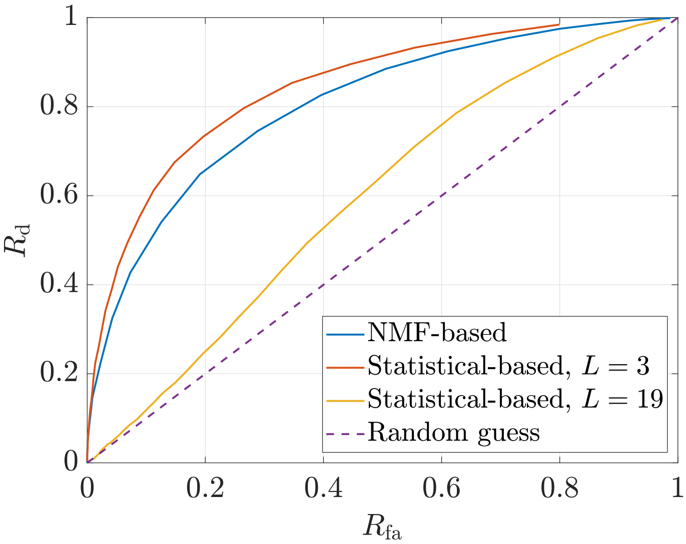

Figure 2.13: ROC curve for the NMF- and statistical-based detectors for different L's under -15 dB JNR for $B = 10$ MHz, $T = 10$ μs.

scenarios for both narrowband and wideband interference sources. Compared with the baseline statistical-based technique, the proposed approach yielded good detection results for different RFI-types and low JNRs with significantly reduced computational complexity.

In the next chapter it is described the proposed detection technique for radio astronomy applications, more specifically, ADS-B signals, which play an important role in the aviation sector, though they corrupt the weak signals captured by radio telescopes.

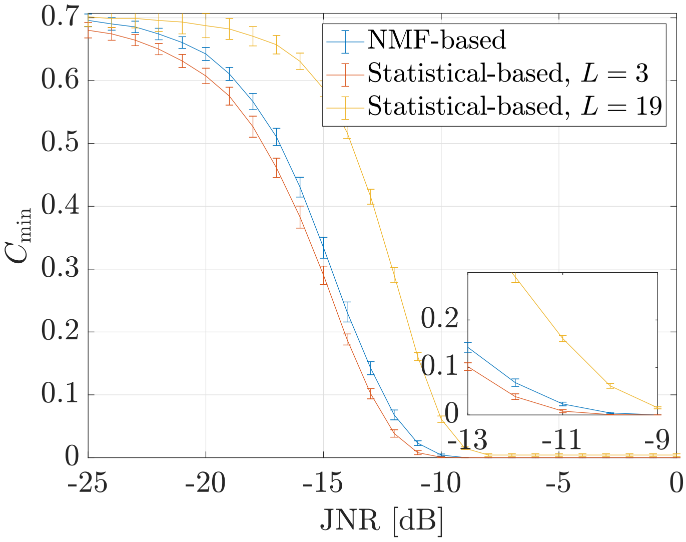

Figure 2.14: $C_{\min}$ values for chirp-type interference signal, for $B = 8$ MHz, $T = 8$ μs for the NMF- and statistical-based detectors.

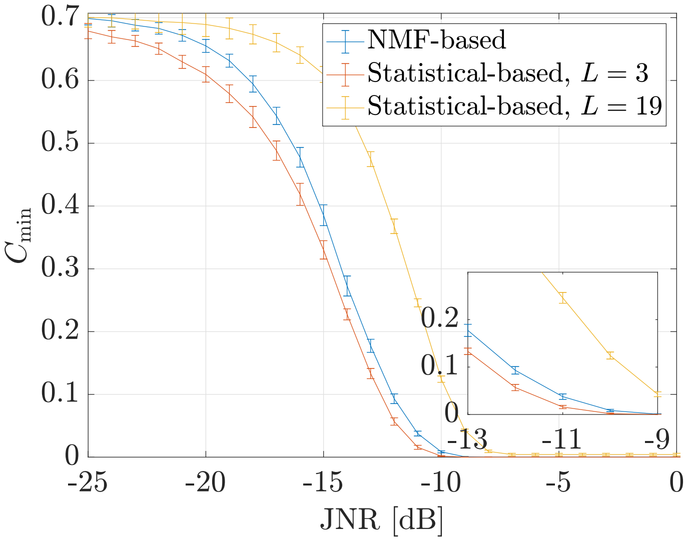

Figure 2.15: $C_{\min}$ values for chirp-type interference signal, for $B = 10$ MHz, $T = 10$ μs for the NMF- and statistical-based detectors.

Chapter 3

Radio Frequency Interference Detection for Radio Astronomy

RFI signals pose serious risks to the observation of astronomical events. Essentially, the signals captured by radio telescopes are severely corrupted by interference due to increasing usage of the radio frequency spectrum. Therefore, it is of paramount importance to address the RFI issue. In this chapter, a framework based on time-frequency (TF) to detect ADS-B signals is proposed with a view to triggering downstream mitigation strategies which are described in Chapter 5. We apply this scheme to real-life data from Parkes radio telescope, located in Parkes, New South Wales, Australia, to demonstrate its performance and efficacy in detecting RFI. The main content of this chapter was presented and published in the proceedings of the *2021 IEEE International Symposium on Circuits and Systems* (ISCAS) [63].

3.1 ADS-B Signal Description

The ADS-B is a surveillance system for tracking aircraft that provides several important measurements in the context of aviation, such as altitude, position, and velocity among others. The communication can occur between a ground station and aircraft, aircraft-to-aircraft, and aircraft-to-satellite. The most used ADS-B configurations are the *squitter* (S) and the *extended squitter* (ES) modes. The ADS-B message consists of a preamble of $8\,\mu$s and a data length of 56 or $112\,\mu$s (mode S, mode ES respectively), and it is modulated using pulse position modulation (PPM), as depicted in Figure 3.1. The message is transmitted every second with each aircraft randomly jittering its transmission around 1 s to avoid message collisions. As for the spectral characteristics, the ADS-B signal has a centre frequency of 1,090 MHz, and a bandwidth of 4.6 MHz [64].

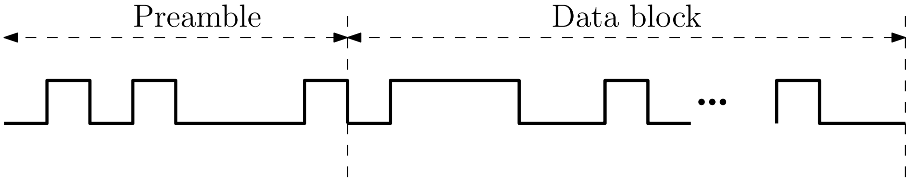

Figure 3.1: ADS-B message.

3.2 Parkes Dataset

The dataset employed in this work was acquired at the Parkes radio telescope, located in Parkes, New South Wales, Australia. The radio receiver uses a dual-polarised antenna, with corresponding polarisations named polA and polB respectively. The system is capable of receiving signals from 704 to 4,032 MHz, covering a bandwidth of 3,328 MHz divided into 26 sub-bands of 128 MHz. Each sub-band signal is complex sampled using 16 bits, down-converted to DC, and down-sampled to 128 Msamples/s. Further details can be found in [40]. The ADS-B signal falls into sub-band 3, which spans $[1{,}088, 1{,}216]$ MHz. According to [40], 58% of sub-band 3's spectrum has useful data for astronomy purposes. Therefore, it is of paramount importance to detect the ADS-B signals so that further downstream interference mitigation processing can be triggered. In addition to ADS-B, there are other interference sources that fall into sub-band 3. One such interference source is the distance measuring equipment (DME) signals used for aircraft guidance, whose characteristics and mitigation are described in Chapter 4. Parkes radio telescope data can be accessed through the Australia Telescope Online Archive (ATOA) [65].

3.2.1 Data Characteristics

The 10.02-s long sub-band 3 signal from the Parkes radio telescope was divided into non-overlapped frames of 10 ms each resulting in 1,003 frames in total. Each of these frames were then manually labelled and classified into 7 different groups with the assistance of a specialist in radio astronomy. Table 3.1 depicts these groups, along with the number of frames per group. Group 1 corresponds to the signal frames with no RFI; Groups 2 and 3 are related to the signal frames corrupted either by ADS-B or DME signals only respectively. Group 4 represents the signal frames corrupted by both ADS-B and DME RFI, while Group 5 is reserved for the signal frames with unknown RFI types. Signal frames in Group 5 were classified as such since no known source could be attributed to them by the team and the specialist in radio astronomy. Lastly, Group 6 corresponds to the signal frames corrupted with only ADS-B and unknown RFI, and Group 7 represents the signal frames corrupted by all RFI types (ADS-B, DME and unknown RFI).

Table 3.1: Groups used to label the Parkes dataset.

Groups	**#signal frames**
1. No RFI	63
2. ADS-B	166
3. DME	200
4. ADS-B & DME	572
5. Unknown RFI	0
6. ADS-B & Unknown RFI	1
7. ADS-B & DME & Unknown RFI	1

For the purpose of ADS-B signal detection, 740 signal frames from Groups 2, 4, 6, and 7 were used, with 263 signal-frames from Groups 1, 3, and 5 without ADS-B used to evaluate the false alarm rate. Figure 3.2 illustrates the magnitude STFT spectrograms of four signal frames from the Parkes dataset in polA, with the ADS-B RFI highlighted by black rectangles. Figures 3.2(a – b) are from Group 2, with the former representing weak ADS-B occurrences, while the latter is for the case where the signal is corrupted by strong ADS-B interference. It is important to highlight that in Figure 3.2(b) it is possible to observe the ADS-B signal aliased around 1,216 MHz, due to the design of the polyphase filter banks in the receiver. The spectrogram in Figure 3.2(c) is zoomed in so that the unknown RFI within the blue rectangle can be better visualised, with that of the ADS-B RFI visible inside the black rectangle. Despite being located near the ADS-B centre frequency, that signal was deemed as "unknown" due to its shorter time duration than that of the ADS-B's. Figure 3.2(d), on the other hand, displays a spectrogram from Group 7 with the red rectangle highlighting an "unknown RFI", which is related to data buffering issues at the receiver, along with the ADS-B occurrences in black rectangles as usual. Further, there is also a DME signal present at 1,209 MHz, albeit it is not visible given the scale of the figure.

3.3 TF-Based detector

In Chapter 2, a detector that extracts the interference features via nonnegative matrix factorisation (NMF) and performs a similarity evaluation between the received signal's spectrogram's time slices and the RFI's characteristics was proposed. The work detailed in this chapter builds on from this work and extends it to tackle ADS-B signals where the signal characteristics such as pulse duration and bandwidth are determined by international standards [64] and are known *a priori* and hence can be used in the detection process. This eliminates the need for the NMF-based feature extraction used in Chapter 2.

The block diagram of the proposed TF-based detector is illustrated in Figure 3.3.

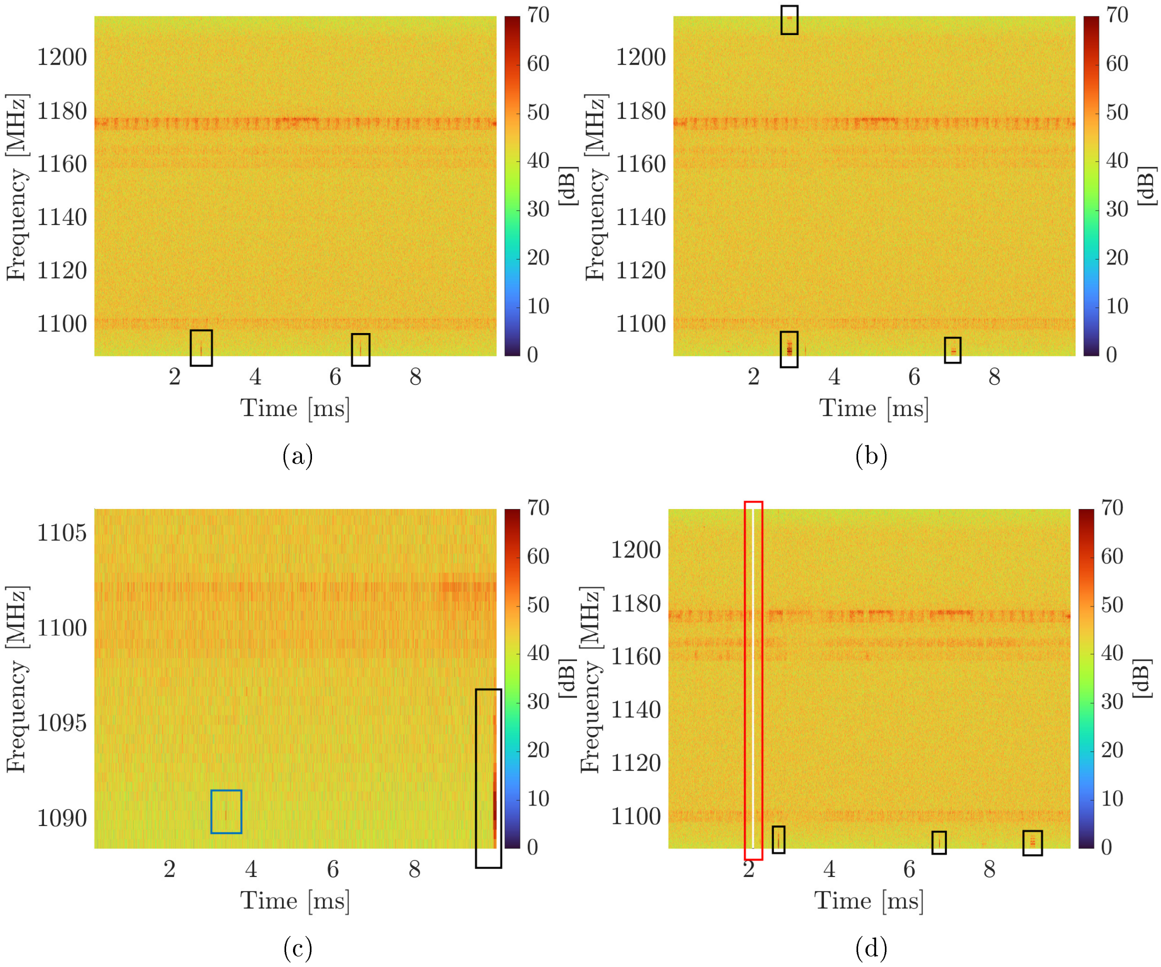

(a) (b) (c) (d)

Figure 3.2: Spectrogram of four signal frames corrupted by ADS-B interference from the Parkes dataset.

The power spectrogram matrix $\mathbf{X}_p$ of the p^{th}-signal frame $\mathbf{r}^p[i]$ from the Parkes dataset is evaluated via the STFT using (2.12).

As mentioned at the beginning of this section, *a priori* information about the ADS-B signals can be used to determine their characteristics, which are represented by the frequency template vector $\mathbf{f} \in \mathbb{N}^{N\times 1}$, whose non-zero entries define the ADS-B signal's bandwidth, as shown in Figure 3.4(a).[1] The next step consists of using the *z-score* operator $\mathcal{Z}(\cdot)$ [61] in both the spectrogram's time slices (columns of $\mathbf{X}^p$), and the template $\mathbf{f}$ to avoid anomalous similarity values, resulting in $\overline{\mathbf{f}} = \mathcal{Z}(\mathbf{f})$, and $\overline{\mathbf{X}^p} = \mathcal{Z}(\mathbf{X}^p) = [\,\overline{\mathbf{x}}_1^p\,\overline{\mathbf{x}}_2^p\,\cdots\,\overline{\mathbf{x}}_M^p\,]$. Analogously to Section 2.4, the similarity between $\overline{\mathbf{x}}_m^p$ and $\overline{\mathbf{f}}$ is assessed by means of the *cosine* function, which can be described as

$$s_m^p = \frac{\overline{\mathbf{f}}^{\mathrm{T}}\overline{\mathbf{x}}_m^p}{\|\overline{\mathbf{f}}\|\|\overline{\mathbf{x}}_m^p\|}, \tag{3.1}$$

---

[1] The frequency axis in Figure 3.4(a) varies from 0–2π as opposed to $-\pi$–π. This was set so that to achieve a continuous spectrum since the aliasing when representing the ADS-B signals may occur, as observed in Figure 3.2(c).

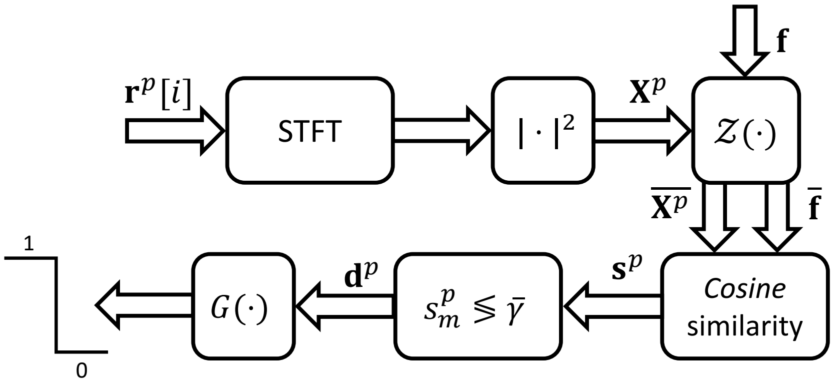

Figure 3.3: Block diagram of the proposed detection framework.

with $\mathbf{s}^p = [\, s_1^p \, s_2^p \, \cdots \, s_M^p \,]^{\mathrm{T}}$. Figure 3.4(b) shows the corresponding similarity vector for the spectrogram described in Figure 3.2(a) and $\bar{\mathbf{f}}$. It can be observed that the similarity values are higher at the time instants where the ADS-B signal is active. Thus, if s_m^p, $m \in \{1, \ldots, M\}$, is larger than the predefined threshold $\bar{\gamma}$, the corresponding sample is flagged as corrupted by RFI. Evaluation of this threshold is discussed in Section 3.4. The output of the threshold comparison is vector $\mathbf{d}^p \in \mathbb{N}^{M\times 1}$, whose m^{th}-sample is 1 if RFI is detected and 0 otherwise. Lastly, the voting scheme, $G : \mathbb{N}^{M\times 1} \to \{0, 1\}$, determines whether the p^{th}-signal frame is corrupted by interference. $G(\mathbf{d}^p)$ plays the role of a majority process, which can be implemented by different functions, such as the median, where the presence of interference is declared if more than 50% of the samples of $\mathbf{d}^p$ indicates the presence of RFI, the logical OR, which flags the RFI corruption if one or more samples of $\mathbf{d}^p$ are 1. The time domain properties of the RFI must be taken into account when choosing G. For instance, the median function is better suited for long-duration interference, whereas the OR function is more applicable when detecting pulsed-type interference, which span only a few samples of the spectrogram.

3.4 Performance Assessment

In this section the performance of the proposed method is compared against frequency- and TF-based detectors, which are widely used in radio astronomy [41, 43]. These methods evaluate the magnitude of the frequency bin that corresponds to the ADS-B centre frequency (1,090 MHz), flagging the presence of interference in the p^{th}-signal frame if the calculated value is above a predefined threshold. For the TF-based technique, the magnitude of the 1,090-MHz bin is assessed for each time slice of the spectrogram. Given the short time duration of the ADS-B signals, both the proposed and the TF-based techniques make use of the logical OR as the voting scheme to generate the single bit detection output per signal frame. The

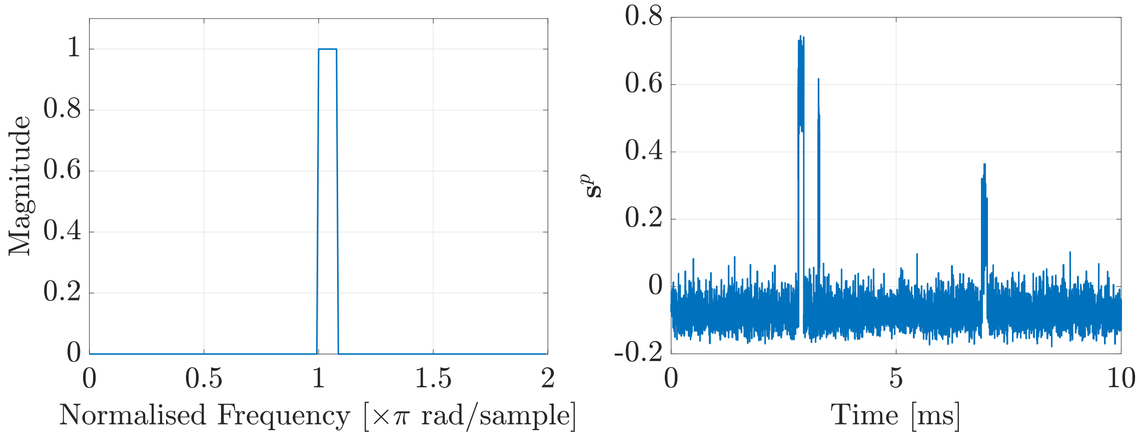

(a) (b)

Figure 3.4: ADS-B frequency template $\mathbf{f}$ (a) and the similarity $\mathbf{s}^p$ between the magnitude spectrogram in Figure 3.2(a) and $\bar{\mathbf{f}}$ (b).

Parkes dataset was split into training and test signal frames. The thresholds for the proposed, frequency- and TF-based detectors were established based on the training dataset and the performance evaluated using the signal frames from the test dataset. In order to have a fair comparison, the performance of the time-domain based techniques is not presented since they do not make use of ADS-B frequency information, such as the centre frequency. The proposed, frequency- and TF-based techniques are hereafter named as Template-, Frequency-, and TF-based respectively. The performance of the techniques in this chapter is assessed via $C_{\min}$ and ROC curves as in Chapter 2.

3.4.1 Experimental Setup

The sampling frequency employed to acquire the Parkes dataset, as described in Section 3.2.1, is 128 MHz. The signals from the Parkes dataset corresponding to polA are used for detection. The detection threshold used in the Template-based technique varies in the interval $[0, 1]$, while the Frequency- and TF-based detectors' ones vary in the intervals $[0, 20 \times 10^4]$ and $[200, 3000]$ respectively. As for the STFT parameters, the number of DFT points and the length of the rectangular window are $N = L = 256$, with a hop size of $R = L/2 = 128$ samples.

The training and test datasets were generated randomly using a proportion of 60% of the signal frames for training, and 40% for test. This represents 444 frames with ADS-B and 158 without ADS-B signals for training, and 296 with and 105 without ADS-B signals for test datasets.

3.4.2 Training Results

The performance of the proposed Template-, the Frequency- and TF-based detectors using the training dataset is shown in Figure 3.5, with the sub-figure depicting the performance of the Template- and TF-based methods using logarithmic scale to better visualise the performance differences for lower false alarm rates. It can be observed that the proposed Template-based method outperforms the baseline techniques, providing a higher detection rate at a lower false alarm rate. Table 3.2 describes the corresponding figures of merit and detection thresholds obtained by the minimisation in (2.19). As can be observed, the proposed detector achieves the smallest C_{min} value among all the techniques, detecting ADS-B in 398 out of 444 signal frames corrupted by such interference, with only 10 false alarms out of 158 frames.

The Frequency-based detector achieved detection and false alarm rates of 0.7095 and 0.3291 respectively. Whereby it was not able to detect the presence of ADS-B interference in 129 out of 444 signal frames, with 52 out of 158 signal frames wrongly flagged as corrupted by ADS-B signals, despite their absence. The TF-based method, on the other hand, was not able to detect the presence of ADS-B signals in 90 signal frames, with 12 of them detected incorrectly.

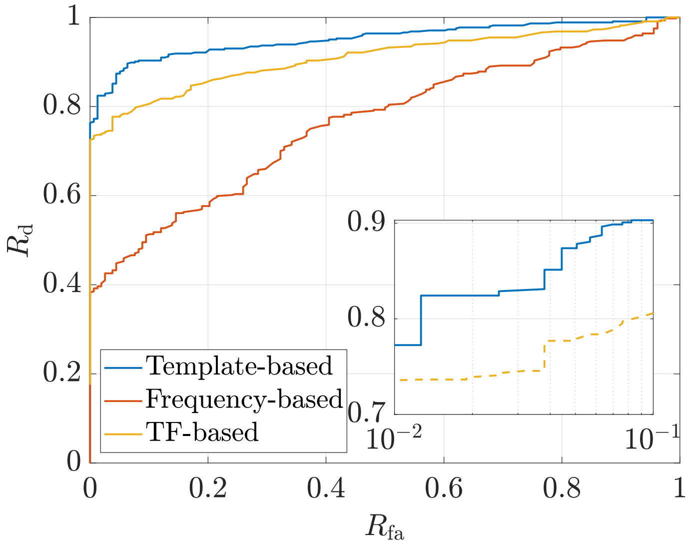

Figure 3.5: ROC curves of the proposed, Frequency-, and TF-based detectors.

Table 3.2: Detection results for the training dataset.

	Proposed	**Frequency-based**	**TF-based**
C_{min}	0.1214	0.4390	0.2165
R_{d}	0.8964	0.7095	0.7973
R_{fa}	0.0633	0.3291	0.0756
$\bar{\gamma}$	0.1545	1.1900×10^4	540.2000

For lower false alarm rates, referring to the logarithmic scale sub-figure in Figure 3.5, overall the proposed method yields higher detection rates with lower false alarm rates. Considering radio astronomy applications, a higher R_{d} might be prioritised, over false alarm rate. As such, for R_{d} around $= 0.9$, the corresponding false alarm rate of the proposed technique is $R_{\mathrm{fa}} = 0.0823$, whereas the TF-Based one is around $R_{\mathrm{fa}} = 0.3670$, more than 4 times higher.

3.4.3 Test Results

The results in this section use the threshold that was obtained via (2.19) using the training dataset. This is done to investigate whether the optimised threshold $\bar{\gamma}$ is generic enough to yield similar detection results when using the signal frames from the test dataset. Table 3.3 shows the performance of the proposed and baseline techniques using their corresponding thresholds from Table 3.2, where C denotes the distance from the resulting point $(R_{\mathrm{fa}}, R_{\mathrm{d}})$ achieved using the threshold from the training dataset to $(0, 1)$. As in Section 3.4.2, the proposed Template-based technique outperforms the baseline methods, achieving higher detection rate with few false alarms.[2]

Table 3.3: Detection results for the test dataset.

	Proposed	**Frequency-based**	**TF-based**
C	0.1792	0.3913	0.2017
R_{d}	0.8918	0.7669	0.8277
R_{fa}	0.1429	0.3143	0.1048

It is important to mention that the improved detection capability offered by the proposed approach is achieved at the expense of increased computational complexity. The additional computational burden of the proposal, when compared to the TF-based method, is the *cosine* similarity and z-score evaluation, which can be cast as low complexity inner products.

3.5 Conclusions

In this chapter a new TF-based detector for radio astronomy signals was proposed. Inspired by the technique described in Chapter 2, the proposed method outperformed classic techniques used in the radio astronomy field, yielding higher detection rates with few false alarm events. In the next chapter we discuss RFI mitigation in

---

[2] The results presented in Sections 3.4.2 and 3.4.3 are slightly different from the ones in [63]. This is due to formatting issues when reading the Parkes dataset, which were later fixed by the expert in radio astronomy signals who collaborated in this research project.

the context of GNSS, describing the proposed frameworks in detail and comparing their performance against techniques commonly used in the literature.

Chapter 4

Radio Frequency Interference Mitigation for GNSS

In Chapter 2 we described the mathematical definitions of NMF and how it performs the decomposition of a nonnegative matrix $\mathbf{X}$ into $\mathbf{WH}$. Throughout the text, we show how to estimate $\mathbf{W}$ in order to promote the separation between interference and the GNSS signals. The proposal can be tailored to the RFI at hand, where the interference type is assumed known beforehand (supervised NMF), or it can be completely blind, where no information about the RFI is provided (semi-blind NMF). In addition, the proposed framework is able to mitigate multiple RFI signals with a single receiver. Distinct types of RFI are used for performance evaluation, such as CW and chirp interference, and distance measuring equipment (DME) signals, employed for aircraft guidance. We compare the performance of the NMF-based technique with classic methods from the literature, with the proposal yielding superior results in strong RFI scenarios. The NMF scheme for DME signals was presented and published in the proceedings of the *2021 XXXIVth General Assembly and Scientific Symposium of the International Union of Radio Science* (URSI GASS) [66]. An extended version of this work which covers the CW- and chirp-type RFI mitigation with the addition of the semi-blind framework, is currently under review for publication in *IEEE Transactions on Aerospace and Electronic Systems (TAES)* [67].

4.1 NMF-Based RFI Mitigation Scheme

In this section we present the proposed NMF-based frameworks for RFI mitigation. The main idea is to separate the interference from the so-called signal of interest, composed by the GNSS signals embedded in noise, using NMF. In (2.3), we describe the received signal as the sum of an undesired term, i.e., the jamming signals, and the signal of interest (SOI), composed by the spreading codes embedded in noise. Therefore, the received signal can also be described in vector form as

$$\mathbf{r}[i] = \mathbf{r}_{\mathrm{RFI}}[i] + \mathbf{r}_{\mathrm{SOI}}[i]. \tag{4.1}$$

This notation will be useful further in the text when describing the proposed RFI mitigation frameworks. In the next subsections, we show how to calculate and use the dictionary matrix $\mathbf{W}$ along with the time activation matrix $\mathbf{H}$ for further estimation of $\mathbf{r}_{\mathrm{RFI}}[i]$ and $\mathbf{r}_{\mathrm{SOI}}[i]$ as in (4.1).

4.1.1 Supervised NMF for GNSS

The NMF decomposes a matrix $\mathbf{X}$, whose elements are nonnegative, into a product of two matrices such that $\mathbf{X} \approx \mathbf{WH}$. As described in Chapter 2, the estimation of $\mathbf{W}$ and $\mathbf{H}$ is performed via an optimisation problem, whose solution is reached recursively using (2.10) and (2.11). This assumes no prior knowledge about the sources at hand, such as their frequency content. However, in some applications such as audio processing, clean versions of the sources may be available. For instance, suppose the mixture signal is comprised of a guitar playing along with a piano. It is possible to obtain clean versions of signals from those instruments and perform the so-called supervised NMF to separate them [68, 69]. In the context of GNSS, the RFI signals can be obtained through a prior characterisation process. Also, the unique spreading code associated with each GNSS signal along with the white noise assumption can be used to estimate the RFI and GNSS signal $\mathbf{W}$ matrices, hereafter named as $\mathbf{W}_{\mathrm{RFI}}$ and $\mathbf{W}_{\mathrm{SOI}}$ respectively, and further employ the NMF algorithm to estimate the respective activation sub-matrices in $\mathbf{H}$ (see (4.2)), while keeping $\mathbf{W}$ fixed. This process can be better described as follows: during the training phase, a clean version of the RFI, and of the GNSS signals are used to estimate their respective dictionary matrices $\mathbf{W}_{\mathrm{RFI}}$ and $\mathbf{W}_{\mathrm{SOI}}$ using both (2.10) and (2.11). In the second step, called test phase, those matrices are concatenated so as to have a single $\mathbf{W}$ matrix, $\mathbf{W} = [\mathbf{W}_{\mathrm{RFI}}\, \mathbf{W}_{\mathrm{SOI}}]$, which is kept fixed across the iterations, i.e., $\mathbf{W}[k] = \mathbf{W}$, and employed to estimate $\mathbf{H}$ using (2.10). This process is further described in Algorithm 1. The activation matrix can be expressed as

$$\mathbf{H} = \begin{bmatrix} \mathbf{H}_{\mathrm{RFI}} \\ \mathbf{H}_{\mathrm{SOI}} \end{bmatrix}. \tag{4.2}$$

In order to illustrate how NMF decomposes the matrix $\mathbf{X}$, Figure 4.1 shows the magnitude spectrogram of a chirp signal with $B = 8$ MHz and $T = 8.62$ μs embedded in noise with one GPS L1 signal for 30-dB JSR. (Further details regarding

Algorithm 1 Pseudo-code for the supervised NMF framework.

```
1: Initialisation:
    Randomly choose $\mathbf{W}$ and $\mathbf{H}$.
2: Training phase:
    Use clean versions of the signal of interest and RFI.
    Estimate $\mathbf{W}_{\text{RFI}}$ and $\mathbf{W}_{\text{SOI}}$ to form $\mathbf{W}$ and the respective $\mathbf{H}$ matrices using (2.10) and (2.11).
    Store $\mathbf{W}_{\text{RFI}}$ and $\mathbf{W}_{\text{SOI}}$.
3: Test phase:
    Using the received signal, estimate $\mathbf{H}_{\text{RFI}}$ and $\mathbf{H}_{\text{SOI}}$ via (2.10) to form $\mathbf{H}$ using the previously computed $\mathbf{W}_{\text{RFI}}$ and $\mathbf{W}_{\text{SOI}}$.
```

magnitude spectrogram calculation are given in Section 4.1.4.) Figure 4.2 displays the corresponding $S = 5$ columns of $\mathbf{W}_{\text{RFI}}$, estimated via (2.10) and (2.11), using the "clean" version of the chirp signal. As can be observed, the components accurately represent the spectrum of the chirp signal. Figure 4.3 displays the S rows of the $\mathbf{H}_{\text{RFI}}$ matrix, which represent the time evolution of the chirp frequency spectrum, computed as (2.10) using the previously estimated $\mathbf{W}_{\text{RFI}}$. As can be seen from Figure 4.1, at around 7 μs, the chirp instantaneous frequency wraps around from 4 to -4 MHz, represented by the blue curve in Figure 4.3, which in turn, is related to the blue curve in Figure 4.2. Similarly, as the chirp instantaneous frequency evolves over time, the remaining components of $\mathbf{H}$ are activated, until the maximum frequency is reached at around 15 μs.

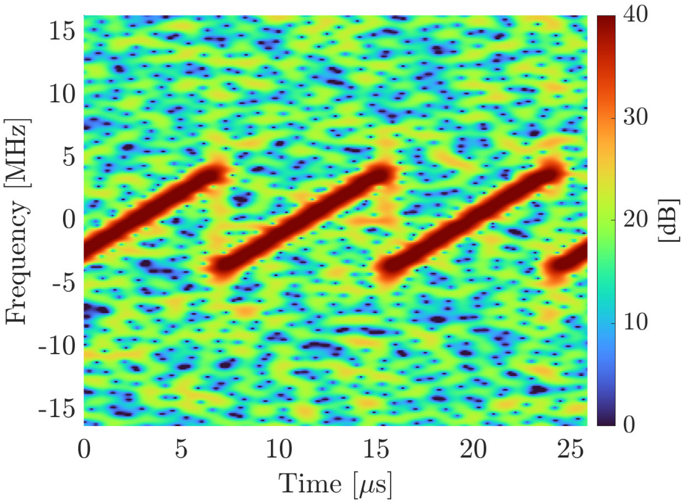

Figure 4.1: Magnitude spectrogram of the chirp signal with $B = 8$ MHz and $T = 8.62$ μs corrupted by noise with one GPS L1 signal.

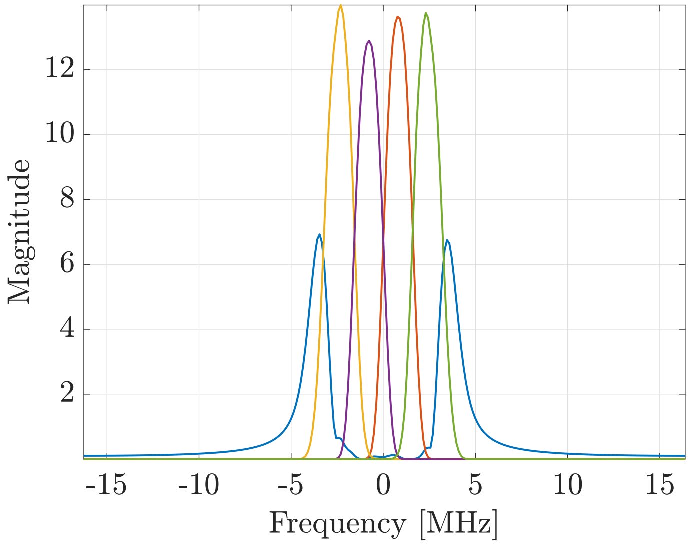

Figure 4.2: Columns of $\mathbf{W}_{\text{RFI}}$ estimated in the training phase for an 8 MHz chirp-type RFI.

4.1.2 Semi-blind NMF

In the semi-blind NMF framework, the RFI signal is considered unknown. Regarding the GNSS application, the RFI can have distinct time and frequency properties, with CW- and chirp-type interference being among the most commonly encountered signals. In order to mitigate RFI with such distinct characteristics and without any prior knowledge about them, we propose the use of the semi-blind NMF (SBNMF) [70]. Similarly to the supervised NMF, the working principle of SBNMF can also be divided into training and test phases. In the former, only $\mathbf{W}_{\text{SOI}}$ is estimated using the GNSS spreading code signal embedded in noise. In the test phase, unlike supervised NMF, with SBNMF the RFI frequency signature matrix $\mathbf{W}_{\text{RFI}}$ is estimated on the fly using (2.11) and (2.10). In high JSR environments, the RFI component in (4.1) dominates over the signal of interest, which makes the received signal spectrum very similar to that of the RFI's. In this sense, $\mathbf{W}_{\text{RFI}}$ estimation is quite similar to the supervised NMF's. The idea of SBNMF is to separate any signal in a way distinct from the signal of interest. The SBNMF framework employs $\mathbf{W}_{\text{SOI}}$ to aid the estimation of $\mathbf{W}_{\text{RFI}}$ and the respective time activation matrices $\mathbf{H}_{\text{RFI}}$ and $\mathbf{H}_{\text{SOI}}$. Figures. 4.4 and 4.5 show the $\mathbf{W}_{\text{RFI}}$ and $\mathbf{H}_{\text{RFI}}$ matrices estimated in the test phase. Close comparison of Figures. 4.2 and 4.4 show that estimated $\mathbf{W}_{\text{RFI}}$ matrices are quite similar to one another within the RFI bandwidth for the supervised and semi-blind cases. While the curves are somewhat different in shape and magnitude, the overall spectrum represented by them is identical. The small fluctuations outside of the RFI bandwidth can be attributed to noise.

The $\mathbf{W}_{\text{RFI}}$ matrix estimated by the semi-blind NMF framework in the presence of multiple RFI sources – an 8 MHz chirp- and a CW-type RFI at 2 MHz – corrupting

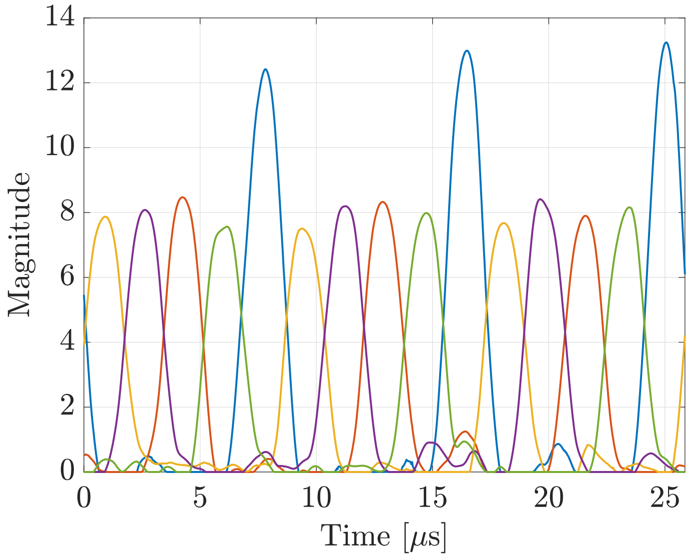

Figure 4.3: Rows of $\mathbf{H}_{\mathrm{RFI}}$ estimated in the training phase for an 8 MHz chirp-type RFI.

the received signal is shown in Figure 4.6. As can be observed, without any *a priori* information about the RFI signals or an RFI characterisation system, the semi-blind NMF approach is able to estimate the spectrum signature of multiple RFI signals. Although the supervised NMF method can also do so, previous information about the chirp bandwidth and CW centre frequency would need to be available for a proper computation of $\mathbf{W}_{\mathrm{RFI}}$. However, in practice, these characteristics may be unknown or need to be estimated.

Hence, the RFI mitigation problem can be cast as the separation of two sources, one comprised of the sum of RFI signals ($\mathbf{r}_{\mathrm{RFI}}[i]$) and the other containing the signals of interest ($\mathbf{r}_{\mathrm{SOI}}[i]$) – the GNSS signals, as in the signal model in (4.1). In the supervised NMF framework, RFI characteristics must be know *a priori* so that $\mathbf{W}_{\mathrm{RFI}}$ matrix can be calculated properly. For semi-blind NMF this is not necessary, since $\mathbf{W}_{\mathrm{RFI}}$ is calculated directly on-the-fly from the received signal.

4.1.3 Phase Reconstruction

The proposed NMF-based scheme decomposes the input matrix $\mathbf{X}$ as $\mathbf{X} \approx \mathbf{W}_{\mathrm{RFI}}\mathbf{H}_{\mathrm{RFI}} + \mathbf{W}_{\mathrm{SOI}}\mathbf{H}_{\mathrm{SOI}}$, i.e., the sum of two magnitude time-frequency matrices. In order to add the phase information of the RFI and signal of interest to enable reconstruction in the time domain, we employ the Wiener filtering process [50, 71]. Hence, the complex time-frequency representation of each source can be described

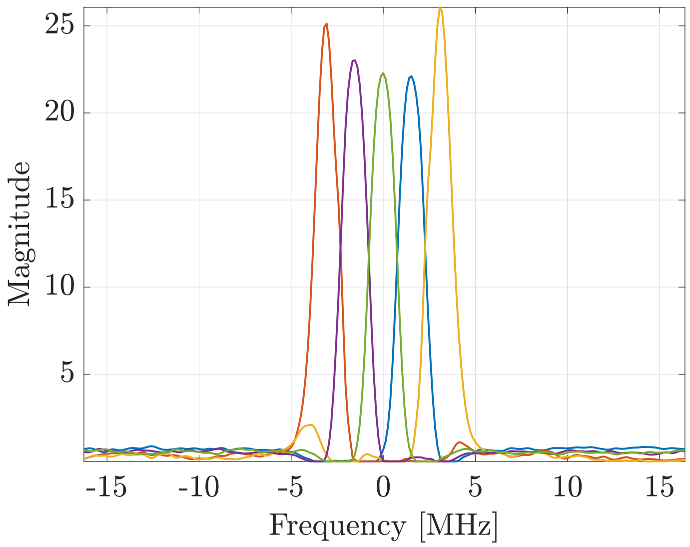

Figure 4.4: Columns of $\mathbf{W}_{\mathrm{RFI}}$ estimated in the test phase for an 8 MHz chirp-type RFI.

as

$$\hat{\mathbf{R}}_{\mathrm{RFI}} = \frac{\mathbf{W}_{\mathrm{RFI}}\mathbf{H}_{\mathrm{RFI}}}{\mathbf{WH}} \otimes \mathbf{R}, \tag{4.3}$$

$$\hat{\mathbf{R}}_{\mathrm{SOI}} = \frac{\mathbf{W}_{\mathrm{SOI}}\mathbf{H}_{\mathrm{SOI}}}{\mathbf{WH}} \otimes \mathbf{R}, \tag{4.4}$$

where $\mathbf{R}$ represents the complex time-frequency (TF) matrix calculated from the received signal $\mathbf{r}$. Thus, the inverse time-frequency transform is used to recreate both the RFI and signal of interest in the time domain, $\hat{\mathbf{r}}_{\mathrm{RFI}}$ and $\hat{\mathbf{r}}_{\mathrm{SOI}}$, respectively.

The block diagram of the proposed NMF-based framework for RFI mitigation is illustrated in Figure 4.7. The TF matrix $\mathbf{R}$ is calculated from the received signal $\mathbf{r}$. Next, the magnitude of each entry of $\mathbf{R}$ forms matrix $\mathbf{X}$, which serves as the input to the NMF-based framework (supervised or semi-blind) for the calculation of $\mathbf{W}$ and $\mathbf{H}$. These matrices, along with $\mathbf{R}$, are used to compute the complex time-frequency matrices $\hat{\mathbf{R}}_{\mathrm{RFI}}$ and $\hat{\mathbf{R}}_{\mathrm{SOI}}$. Finally, $\hat{\mathbf{r}}_{\mathrm{SOI}}$ is obtained via inverse TF transform. While $\hat{\mathbf{r}}_{\mathrm{SOI}}$ is used in subsequent GNSS processing, $\hat{\mathbf{r}}_{\mathrm{RFI}}$ can be used for further RFI classification, and characterisation as well as for geo-localisation purposes.

4.1.4 Time-Frequency Transforms

NMF-based techniques require that the input matrix $\mathbf{X}$ is nonnegative and it is desirable that the underlying TF transform is invertible. Given the RFI characteristics, a large variety of works in the literature use the STFT, or its magnitude [27, 30, 52, 72].

The STFT is a popular choice as time-frequency (TF) transform, however, it has some inherent limitations. Its time-frequency resolution is constant, i.e., a higher

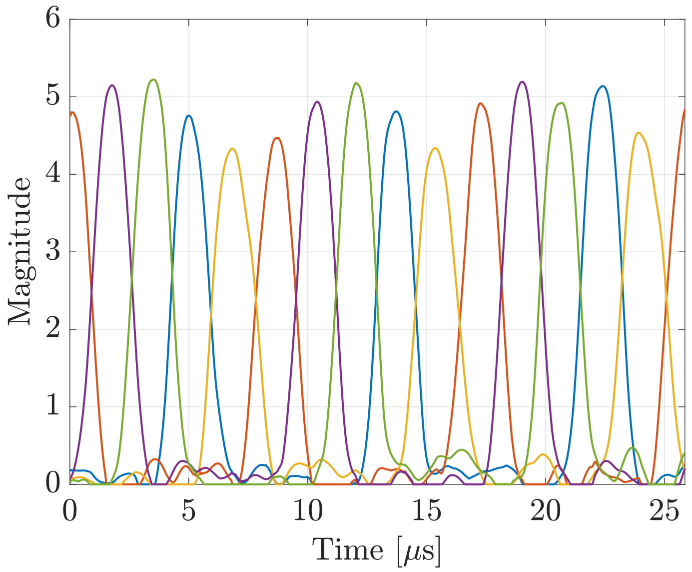

Figure 4.5: Rows of $\mathbf{H}_{\mathrm{RFI}}$ estimated in the test phase for an 8 MHz chirp-type RFI.

resolution in the time domain is achieved at the expense of a poorer frequency resolution, and vice-versa [73]. Considering a chirp-type RFI, due to its relatively short period (usually a few microseconds), small window lengths should be used, which produce low frequency resolutions in the TF domain. As can be observed in Figure 4.1, the STFT representation of the chirp signal is not well localised, with the instantaneous frequency spread across a number of adjacent frequency bins. As a result, the STFT yields noticeably thick lines in the magnitude spectrogram. In the context of NMF-based techniques, better separation results are obtained when the overlap in the TF domain between the signal of interest and interference is minimised. In order to address this issue, we propose the use of Fourier synchrosqueezed transform (FSST) [74, 75], which is a modified version of the STFT tailored to work with multicomponent signals, such as chirps and CW. In fact, the FSST reduces the spectral leakage amongst the adjacent frequency bins, enhancing the time-frequency resolution, thus yielding better localised representations in the TF domain. Therefore, the FSST may help minimising the overlap between the RFI and the signal of interest in the TF plane, thereby leading to better estimation of $\hat{\mathbf{r}}_{\mathrm{SOI}}$ and $\hat{\mathbf{r}}_{\mathrm{RFI}}$. Before defining the FSST, we modify (2.12) as

$$\left[\widetilde{\mathbf{S}}\right]_{n,m} = \sum_{l=0}^{L-1} r[m+l] f[l] \mathrm{e}^{-\mathrm{j}\frac{2\pi}{N}n(l-m)}. \tag{4.5}$$

Thus, the FSST can be expressed as

$$[\mathbf{T}]_{\widetilde{n},m} = \frac{1}{f_0} \sum_{n=0}^{N-1} \widetilde{\mathbf{S}}_{n,m} \delta[\widetilde{n} - \hat{\phi}_{n,m}], \tag{4.6}$$

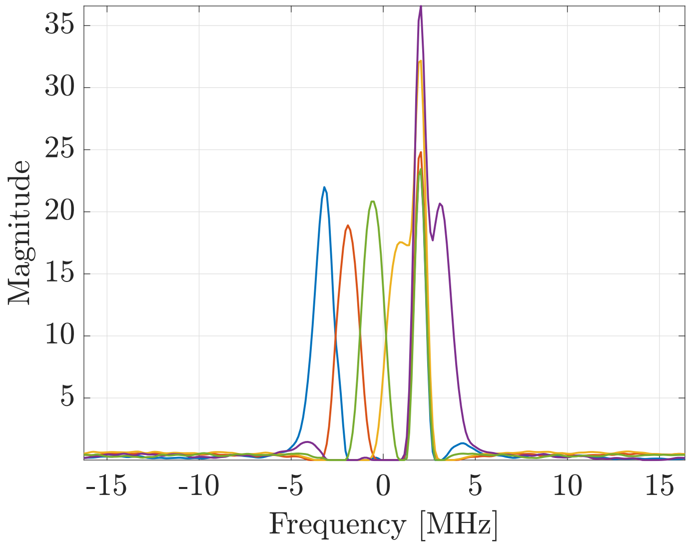

Figure 4.6: Columns of $\mathbf{W}_{\mathrm{RFI}}$ estimated in the test phase for an 8-MHz chirp- and CW-type RFI at 2 MHz.

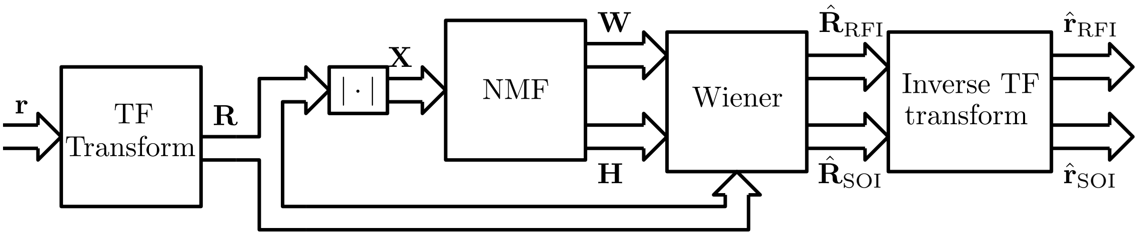

Figure 4.7: Block diagram of the NMF-based framework.

where f_0 denotes the middle sample of the window f, $\delta[i]$ represents the Kronecker delta function, and $\hat{\phi}_{n,m}$ stands for the $(n,m)^{\text{th}}$-local instantaneous frequency estimated as in [75], with $R = 1$ in (4.5) to ensure perfect reconstruction. Figure 4.8 displays the magnitude FSST spectrogram of an 8 MHz chirp-type RFI signal. When compared to the magnitude spectrogram calculated via STFT in Figure 4.1, it can be observed that the chirp spectrum is more concentrated around the instantaneous frequencies due to the "squeezing" process described in (4.6). However, this enhanced localisation property is slightly degraded for rapidly time-varying signals, such as chirps with wide bandwidths and small periods. It is worth pointing out that the TF transform matrix $\mathbf{R}$ can be calculated using STFT as in (2.12) or FSST as in (4.6). Further, our framework enables the use of any nonnegative TF transform whose inverse ensures perfect or nearly perfect signal reconstruction.

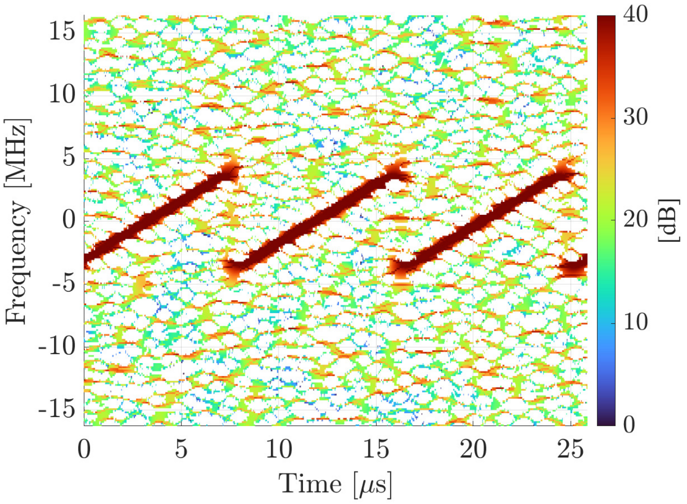

Figure 4.8: Magnitude FSST spectrogram of a chirp signal with $B = 8$ MHz and $T = 8.62$ μs corrupted by noise with one GPS L1 signal.

4.2 DME Signal Mitigation

In Chapter 2 we described the main RFI types in the context of GNSS, i.e., chirp and CW signals. However, there is a myriad of signals that can be deemed as interference. For instance, the distance measurement equipment (DME) system operating in the 962–1,213 MHz band [76], sharing frequency spectrum with GPS L5, centred at 1,176.45 MHz is one such interference source. DME is a two-way ranging system that enables the aircraft to calculate its slant range to a DME ground station. The aircraft transmits an interrogation signal to the ground station, which then generates a corresponding reply. The time delay between the interrogation and reply signals is then used for range calculation. Multiple ground stations can be visible to the aircraft, thus making DME a potential RFI threat to the GPS L5 signal.

4.2.1 DME Signal Characteristics

The aircraft transponder transmits a pair of 3.5-μs pulses separated by 12 μs whose power varies between 50 to 2,000 W [77]. Typically, the pulse pair rate ranges from 1,200 to 1,500 pulses/s. The DME band is divided into 126 channels for reply (ground-to-air), and 126 channels for interrogation (air-to-ground), with channel spacing of 1 MHz and signal bandwidth of 100 kHz. The interrogation and reply frequencies are always ±63 MHz apart. The DME transmission and reception frequency scheme is illustrated in Figure 4.9. For instance, if the aircraft interrogates at 1,107 MHz, the ground station replies at 1,170 MHz.

The baseband DME signals employed in this work were generated using [78], which allows us to set a variety of parameters, such as aircraft position, speed,

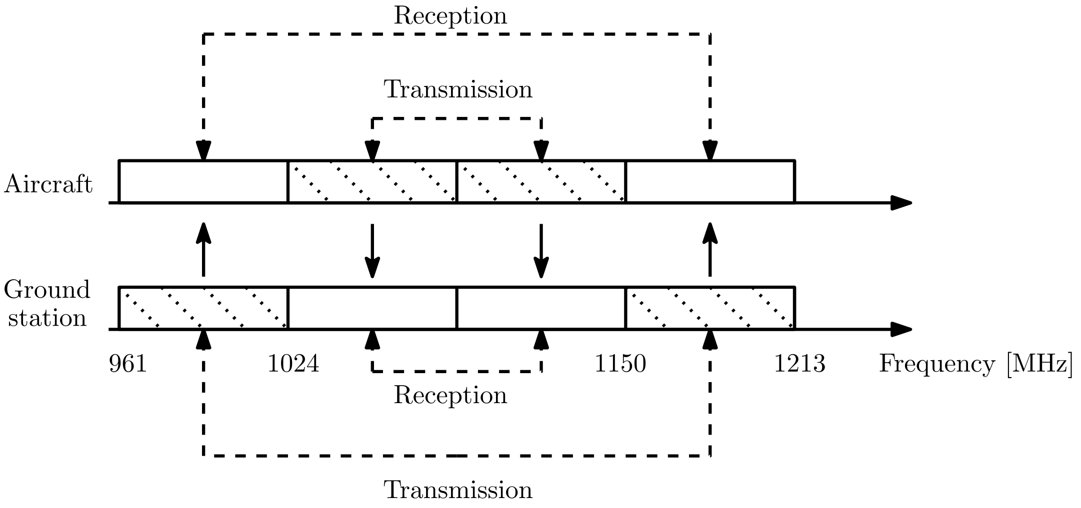

Figure 4.9: DME transmission and reception scheme.

and altitude, among others. The simulator employs information of various DME ground stations spread across Europe to generate the received signal at the aircraft. Considering flight level FL390 with altitude 11,800 m, there are 78 visible ground stations to the aircraft receiver. Figure 4.10(a) depicts a 1-ms snapshot of the generated DME signal in the time domain with numerous peaks, whereas Figure 4.10(b) shows the corresponding signal spectrum, with the GPS L5 frequency band displayed in red highlighting the considerable overlap around 1,176.45 MHz, the GPS L5 centre frequency.

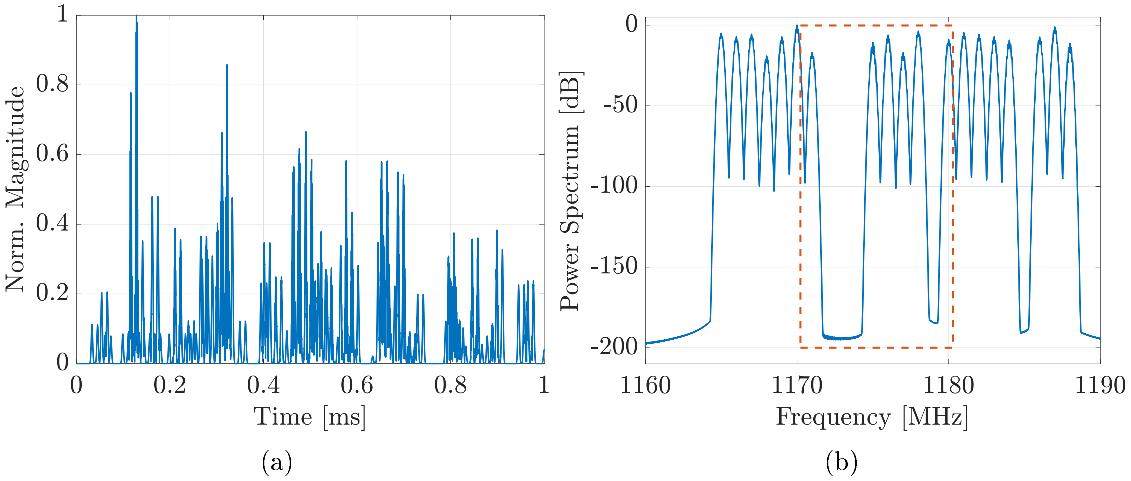

(a) (b)

Figure 4.10: Generated DME signal in the time (a) and frequency (b) domains.

4.2.2 Performance Evaluation

The performance of the proposed supervised NMF-based technique is evaluated considering various jammer-to-signal ratios (JSRs), and compared against pulse blanking (PB) methods from the literature. PB techniques zeros out the samples of the received signal in the time or frequency domain whose magnitude exceed a predefined threshold, thus being suitable to pulsed interference, which makes these techniques widely employed to mitigate DME signals for GNSS [79–81].

Figures of Merit

In the context of GNSS, there are several figures of merit that can be used to assess the RFI mitigation performance such as the carrier-to-noise ratio (C/N$_0$), correlator SNR and generalised SNR, to name a few. The first two rely on post-correlation observables, thus not directly evaluating the impact of RFI on GNSS signal acquisition process. Acquisition process enables the detection of the in-view satellite signals and provides coarse estimates of the code delays and Doppler shifts. The output of the acquisition process is a two-dimensional function of the spreading code delay (τ) and Doppler frequency (f_d) for each in-view satellite signal, which is called the cross ambiguity function (CAF). Using (2.3) and (2.4), the CAF can be expressed as

$$\mathrm{R}_{rc,p}(f_\mathrm{d}, \tau) = \sum_{q=0}^{Q-1} r[q] c_p[q-\tau] \mathrm{e}^{\mathrm{j}\frac{2\pi}{F_\mathrm{s}} f_\mathrm{d} q}. \tag{4.7}$$

Figure 4.11 illustrates a normalised CAF considering a clean GPS signal with code delay of 500 μs and a Doppler shift of 2 kHz. A pronounced peak at around the true code delay and frequency shift values can be clearly observed from the figure.

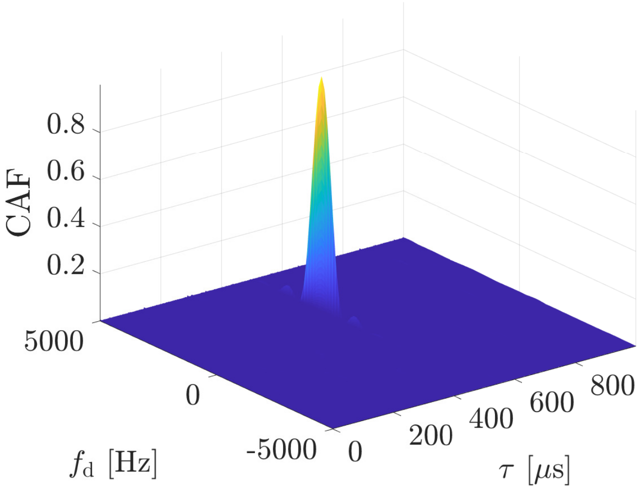

Figure 4.11: CAF of a clean GPS signal.

In order to determine the presence of the p^th-satellite's signal, the magnitude squared value of $\mathrm{R}_{rc,p}(f_\mathrm{d}, \tau)$, defined as $\mathrm{S}_{rc,p}(f_\mathrm{d}, \tau) = |\mathrm{R}_{rc,p}(f_\mathrm{d}, \tau)|^2$, can be compared with a predefined detection threshold [82]. Further, the maximum likelihood estimates of $(f_{\mathrm{d},p}, \tau_p)$ can be obtained as

$$(\hat{f}_{\mathrm{d},p}, \hat{\tau}_p) = \arg\max_{f_\mathrm{d},\tau} \left\{ \mathrm{S}_{rc,p}(f_\mathrm{d}, \tau) \right\}. \tag{4.8}$$

Under reasonable SNR conditions and in the absence of interference, the CAF presents a prominent peak which is used to estimate $f_{\mathrm{d},p}, \tau_p$, and considerable low background "noise" level due to low correlation values between the desired and the actual pseudorandom noise (PRN) codes. The existence of RFI may yield spurious peaks in the CAF, inducing large estimation errors or even hampering the signal detection and acquisition. One of the figures of merit that makes use of the CAF is the generalised SNR (GSNR) [83], which evaluates the mean square distance of the CAF's true peak to the noise floor, normalised by its noise variance. In other words, GSNR measures the CAF quality, assessing how prominent the main peak is in relation to the noise level. The GSNR can be described as

$$\mathrm{GSNR} = \frac{\left(\mathrm{E}\left[\mathrm{S}_{rc,p}(f_{\mathrm{d},p}, \tau_p) - \mathrm{S}_{rc,p}(f_\mathrm{d} \neq f_{\mathrm{d},p}, \tau \neq \tau_p)\right]\right)^2}{\mathrm{Var}\left[\mathrm{S}_{rc,p}(f_\mathrm{d}, \tau)\right]}, \tag{4.9}$$

where τ_p and $f_{\mathrm{d},p}$ represent the true code delay and Doppler shift of the signal from the p^{th}-in-view satellite. Therefore, the performance of the RFI mitigation techniques can be assessed by means of the GSNR, since it reflects the level of corruption of the received signal in the acquisition stage.

Experimental Setup

The sampling frequency is set to $F_\mathrm{s} = 50$ MHz. One GPS L5 signal is generated using [84], with its power set to achieve an SNR of -20 dB, combined with the DME signals generated for flight level FL390, and corrupted by circularly symmetric additive white Gaussian noise, with variance $\sigma^2 = 1$. The JSR varies between $[30, 60]$ dB with 5 dB steps. The discarding threshold for the PB methods (time and frequency) is set to $\bar{\gamma} = 2.146$ so as to achieve a false alarm probability of 0.01. The coherent time considered for acquisition is 1 ms, with 200 independent runs. Overall, 200 ms of DME signals are generated, and at each acquisition time the aircraft is at a different position, hence the DME interference is different for each independent run.

Regarding the STFT parameters, rectangular windows of length $L = 256$ and $L = 1024$ are used, with $N = L$, and a hop size of $R = 1$ for both cases. Therefore, the proposed NMF supervised frameworks are hereafter named NMF-256 and NMF-1024, and the semi-blind schemes called SBNMF-256 and SBNMF-1024 respectively, with the baseline PB techniques in time and frequency domains denominated as PB-time and PB-freq respectively. It is worth highlighting that the FSST is not employed for mitigation here since it is more suitable to chirp- and CW-type RFI, thus it would not bring considerable benefits in terms of signal representation for DME. As per the NMF settings, the KL divergence ($\beta = 1$ in (2.9)) is employed, with number of components to represent both DME signal and signal of interest $S = 60$ for $L = 256$, and $S = 400$ for $L = 1024$, resulting in $(\mathbf{W}_{\mathrm{RFI}}, \mathbf{W}_{\mathrm{SOI}}) \in \mathbb{R}_{+}^{256\times120}$ and $(\mathbf{W}_{\mathrm{RFI}}, \mathbf{W}_{\mathrm{SOI}}) \in \mathbb{R}_{+}^{1024\times800}$ respectively. Further, for estimating those matrices, DME signals are generated using a different aircraft position and hence, they are different from the ones employed for performance evaluation.

Mitigation Results

The generalised SNR performance of the proposed, and the time- and frequency-domain blanking techniques along with the case where no mitigation is employed is shown in Figure 4.12. As can be observed, NMF-1024 outperforms all the techniques considered, with its semi-blind counterpart SBNMF-1024 presenting very similar performance. Further, NMF-256 and SBNMF-256 outperforms the blanking techniques for JSR$\in [30, 50]$ dB. In general, the semi-blind framework achieves akin performance to the supervised scheme, not requiring prior knowledge about the ground station's transmission frequencies. Furthermore, in most cases, the NMF-based techniques yield higher GSNR values. This implies larger correlation ambiguity function (CAF) peak amplitude with a lower noise floor, i.e., lower spurious CAF peak amplitudes, thus improving the GNSS signal detection and subsequent acquisition performance. Moreover, as expected, when no mitigation technique is employed, the GSNR decreases as the power of the DME increases, indicating a higher CAF noise floor. To illustrate this, Figure 4.13 shows the CAFs for JSR $= 60$ dB considering a GPS L5 signal with code delay $\tau = 10$ μs and a Doppler shift $F_{\mathrm{d}} = 1.5$ kHz without the employment of a mitigation technique, Figure 4.13(a), and using, Figure 4.13(b), NMF-1024 based mitigation. In the absence of mitigation the CAF presents many spurious peaks hindering the GPS signal detection. The proposed technique, on the other hand, is able to suppress the strong interference, allowing the detection and subsequent acquisition of the GPS signal.

Another advantage of the NMF-based methods is the RFI suppression without data discarding. The PB techniques, on the other hand, zero out samples in either time or frequency domain to mitigate interference. To better illustrate this effect, Figure 4.14 shows the percentage of discarded samples for each JSR value for the PB-time and PB-freq techniques. For JSR $= 60$ dB, PB-time discards more than 78% of the received signal samples, whereas PB-freq zeroes out more than 30% of the frequency bins, which may result in tracking and navigation data losses. It is important to note that the performance achieved by the proposed technique comes at the expense of higher computational complexity relative to the blanking techniques.

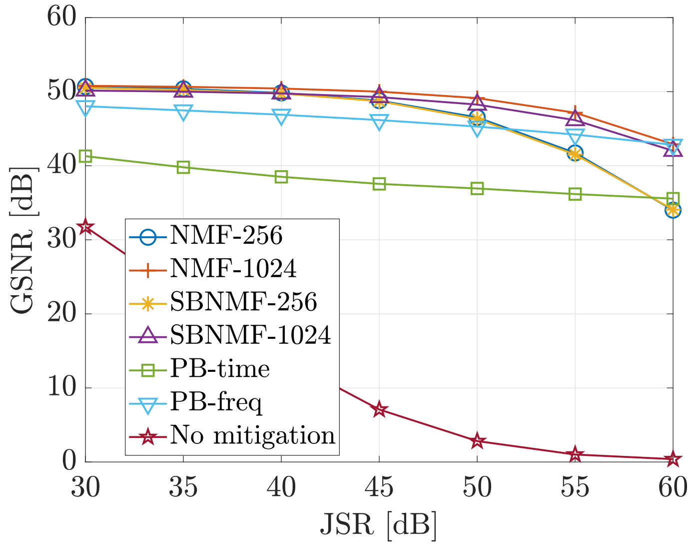

Figure 4.12: Generalised SNR with and without mitigation for different JSR values.

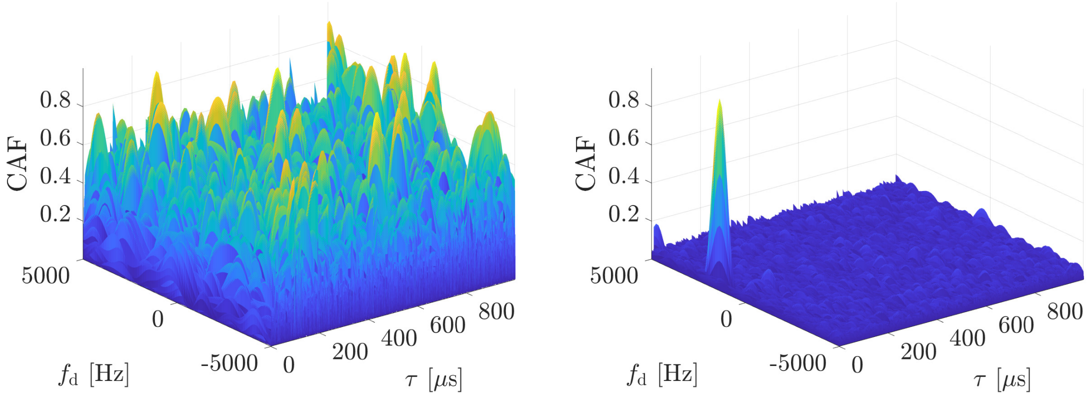

(a) No mitigation.

(b) NMF-1024.

Figure 4.13: CAF without mitigation (a) and for the NMF-1024 technique (b) for JSR = 60 dB.

4.3 CW- and Chirp-type RFI Mitigation

In this section we present the mitigation results considering the most common RFI types found in real life scenarios as described in Section 2.1.

4.3.1 Performance Evaluation

The performance of the proposed techniques is assessed and compared against three GNSS RFI mitigation methods from the literature, viz.: Kalman [30], notch filter [27], and wavelet-based [33]. The former tracks the interference samples for further subtraction in the time domain, whilst the notch filter scheme cancels out the RFI, more specifically chirp signals, by “dechirping” the interference, resulting in a CW signal at DC, which is then filtered out. Both techniques estimate the

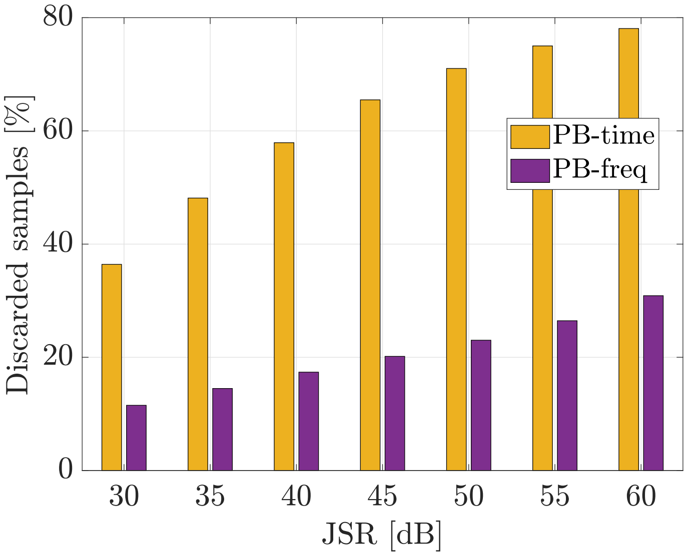

Figure 4.14: Percentage of discarded samples for the PB-time and PB-freq methods for different JSR values.

chirp instantaneous frequency for mitigation. In the wavelet-based technique, received signal is decomposed into sub-bands with distinct frequency resolutions. In the presence of RFI, its samples spread across the sub-bands, which are zeroed out if their magnitude surpasses a predefined threshold. The remaining samples are then resynthesized back into the time domain.

In order to determine the efficacy of the proposed NMF-based framework in dealing with narrow- and wideband RFI sources, chirp-type RFI with different bandwidths, and CW-type RFI with varying frequencies under challenging JSR scenarios are used. Further, combination of multiple RFI signals are employed to evaluate and demonstrate the mitigation capabilities of the proposed approach in the presence of multiple different RFI sources. For the sake of simplicity, the STFT- and FSST-based techniques are hereafter named NMF-STFT and NMF-FSST respectively, with their semi-blind counterparts referred to as SBNMF-STFT and SBNMF-FSST. As for the Kalman, notch filter, and wavelet-based techniques, they are referred to as Kalman, NF and Wavelet, respectively.

Figures of Merit

In order to quantify the performance for CW- and chirp-type RFI, we employ the generalised SNR described in Section 4.2.2. In addition, the GNSS signal detection capability can also be employed to evaluate the RFI suppression performance. This process usually relies on the level of $\mathrm{S}_{rc,p}(\hat{f}_{\mathrm{d},p}, \hat{\tau}_p)$ to indicate the presence of a given spreading code in the received signal. In this work, the detection is performed by comparing the ratio between the highest and the second highest CAF peaks against a threshold $\bar{\gamma}$ as in [82]. Thus, in the presence of GNSS signal, a true positive detection occurs if the ratio exceeds $\bar{\gamma}$ and the highest CAF peak is the true one (the corresponding τ_p and $f_{\mathrm{d},p}$ are known *a priori*). Analogously, a false positive detection takes places when the peak ratio is greater than the threshold, despite the absence of GNSS signal. By calculating the ratio between the true/false positives and the number of trials, the so-called detection and false alarm rates R_{d} and R_{fa} can be determined. These are employed to evaluate the receiver operating characteristic (ROC) curve, which describes the detection capability as a function of the threshold $\bar{\gamma}$ and the true CAF peak detection. Further, in order to leverage the information provided by the ROC, we employ the $C_{\min}$ as in (2.19).

Ultimately, $C_{\min}$ translates the effectiveness of the RFI mitigation method in terms of the GNSS signal detection and thus, along with the GSNR, will be the figures of merit employed in the forthcoming sections.

Experimental Setup

Chirp-type RFI with bandwidth $B \in \{2, 8, 14\}$ MHz and period $T = 8.62\,\mu$s centred at DC, and a CW-type RFI with frequency of 2 MHz are used, along with one GPS L1 signal with an SNR of -20 dB. The JSR for the experiments varies between 25 to 50 dB, with 5 dB steps. The sampling frequency is set to $F_{\mathrm{s}} = 32.768$ MHz, the receiver coherence time is 1 ms, hence, the CAFs are evaluated using 32,768 complex samples. The generalised SNR and $C_{\min}$ values are averaged over 500 trials.

For the STFT and FSST computation, a Kaiser window [73] with shape factor 60 is employed to ensure that the chirp-type RFI can be better localised in the TF domain. The number of frequency bins is set to $N = 256$, with Kaiser window length $L = 256$, and hop size $R = 1$ to ensure good time resolution to properly describe the time properties of the chirp-type RFI.

For NMF, the number of components to describe both the RFI and the signal of interest is set to $S = 5$, hence $(\mathbf{W}_{\mathrm{RFI}}, \mathbf{W}_{\mathrm{SOI}}) \in \mathbb{R}_{+}^{256\times 10}$. The KL divergence ($\beta = 1$ in (2.9)) is used as similarity function. Further, the maximum number of iterations for NMF is set to 500 so as to ensure convergence.

4.3.2 Chirp-Type RFI Mitigation

In this subsection the mitigation results considering chirp-type RFI with varying bandwidth are presented. Figure 4.15 displays the generalised SNR results for $B \in \{2, 8, 14\}$ MHz. As can be seen from Figure 4.15(a), NMF-FSST yields the highest GSNR levels across the JSR values, with GSNR of around 20 dB at JSR $= 50$ dB. For higher JSR values, the wavelet-based method leads to similar GSNRs, followed by the proposed semi-blind techniques, and the NMF-STFT. The Kalman and notch filters present the worst performance, since they are very sensitive to parameter estimation errors, such as instantaneous frequency mismatch. It is worth mentioning that in the scenario of $B = 2$ MHz, in the frequency domain, the GPS *sinc*-shaped main lobe is dramatically corrupted by RFI. Therefore, a considerable part of the GPS spectrum is also filtered out along with the RFI's.

Figure 4.15(b) depicts the GSNR curves for $B = 8$ MHz. Similarly as in Figure 4.15(a), NMF-FSST has the highest GSNR levels, with its STFT-based counterpart NMF-STFT showing similar performance. Further, the performance of the SBNMF-FSST method is on par with that of NMF-STFT, except for JSR = 50 dB. The performance of the SBNMF-STFT technique, on the other hand, is slightly degraded when compared to that of SBNMF-FSST. This is due to the poorer localisation of chirp signals in the TF domain provided by STFT when compared with FSST. It is important to re-note that both SBNMF-FSST and SBNMF-STFT techniques do not require any prior knowledge about the RFI. For the wavelet-based technique, as the chirp bandwidth spreads across the spectrum, more decomposition stages are corrupted by the RFI. As a consequence, more samples of those stages are zeroed out, which affects the signal reconstruction.

In Figure 4.15(c), the results for $B = 14$ MHz are shown. Overall, both supervised and semi-blind NMF frameworks outperform the baseline techniques. For JSR greater than 40 dB, the performance of the latter is slightly degraded. Further, the performance of the techniques that make use of the STFT is enhanced, whereas the performance of those that use FSST-based is slightly deteriorated. This deterioration is related to the chirp rate of the RFI, i.e., the ratio between B and the chirp period T. As discussed in [75], the FSST yields sharper TF representations for slowly time-varying signals, hence the worse performance for $B = 14$ MHz.

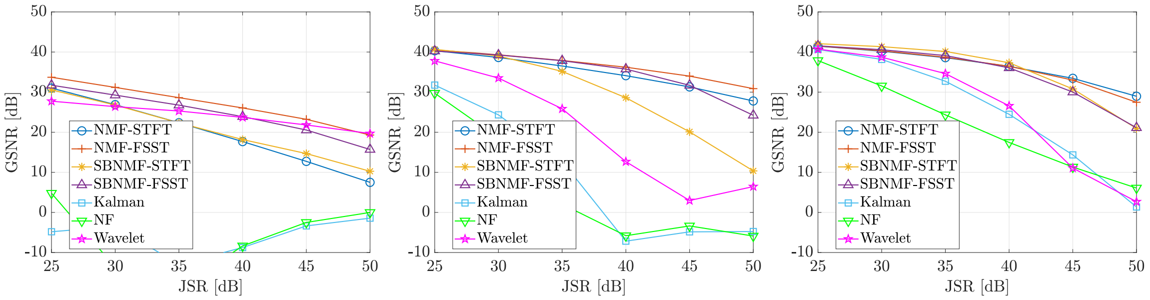

(a) $B = 2$ MHz.

(b) $B = 8$ MHz.

(c) $B = 14$ MHz.

Figure 4.15: Generalised SNR of the proposed and baseline techniques for different values of B.

In terms of evaluating the performance of detecting the correct CAF peak after RFI mitigation, Figure 4.16 shows the C_{min} results for $B \in \{2, 8, 14\}$ MHz. For 2 MHz, the best performance is yielded by NMF-FSST with near zero C_{min} value for 40 dB JSR, followed by Wavelet, and SBNMF-FSST techniques. In other words, a high detection rate was achieved at very low false alarms, despite the presence of strong RFI. In addition, the $C_{\min}$ results can be used to establish the minimum GSNR for successful GNSS signal detection. As previously mentioned, it can be observed in Figure 4.16(a) that for JSR $=$ 40 dB, the resulting $C_{\min}$ is near zero for the NMF-FSST technique, with a corresponding GSNR of $\approx$ 26 dB. At JSR $=$ 45 dB, there is a considerable increase in $C_{\min}$ with GSNR $=$ 23.9 dB. Hence, we adopt 26 dB as a reasonable GSNR level for GNSS signal detection. In our experiments, JSR values higher than 50 dB resulted in GSNR values lower than 26 after RFI mitigation and the GPS signal could not be detected and acquired.

From Figure 4.16(b) and Figure 4.16(c), it can be observed that the proposed techniques outperform the baseline methods, with very low $C_{\min}$ levels in scenarios with very strong RFI (50 dB JSR). It is worth mentioning that some $C_{\min}$ levels are above the value $1/\sqrt{2}$ as a result of the respective technique not being able to detect the true peak in the CAF. Hence, $R_{\mathrm{d}} = 0$ and $C_{\min} = 1$. In order to further demonstrate the effectiveness of the proposed techniques, Figure 4.17 shows the normalised CAFs for the supervised and semi-blind methods for B = 14 MHz and JSR $=$ 45 dB, with Figures 4.18(a)-(c) displaying the normalised CAFs for the baseline techniques, and Figure 4.18(d) the CAF calculated directly from the received signal in the absence of any RFI mitigation. It can be observed from these figures that the NMF-based techniques suppressed the RFI, resulting in a clear peak in the CAFs, enabling the GNSS signal acquisition and further processing. This is not the case when the baseline methods are used, or when no RFI mitigation is applied. Under such cases, the true peak is buried in noise, hampering the signal detection.

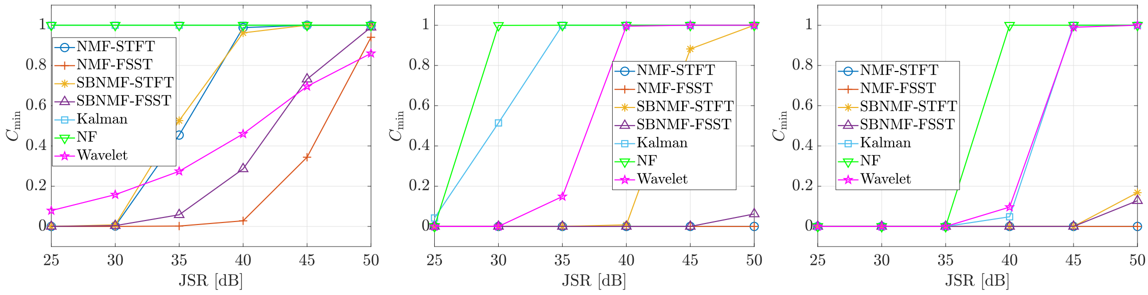

(a) $B = 2$ MHz. (b) $B = 8$ MHz. (c) $B = 14$ MHz.

Figure 4.16: $C_{\min}$ values of the proposed and baseline techniques for different values of B.

4.3.3 Multiple RFI Mitigation

In this subsection the mitigation performance of the proposed and baseline methods is evaluated under the condition of multiple RFI signals – a chirp-type RFI with

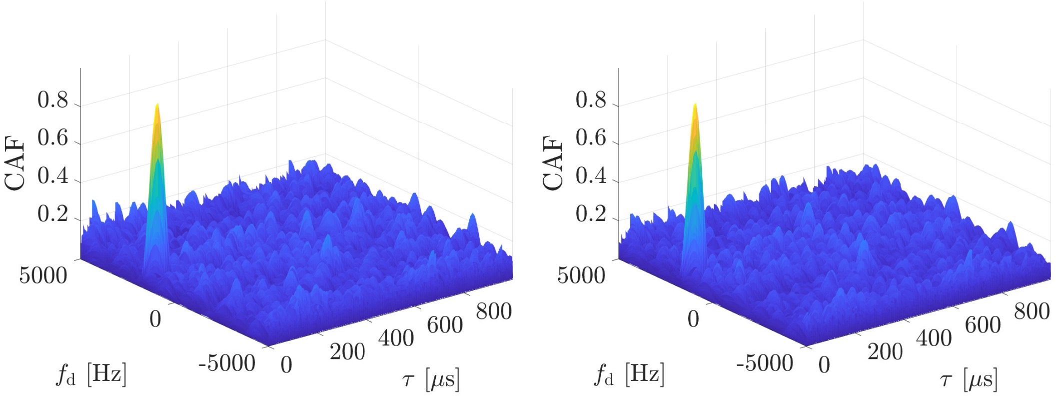

(a) NMF-STFT.

(b) NMF-FSST.

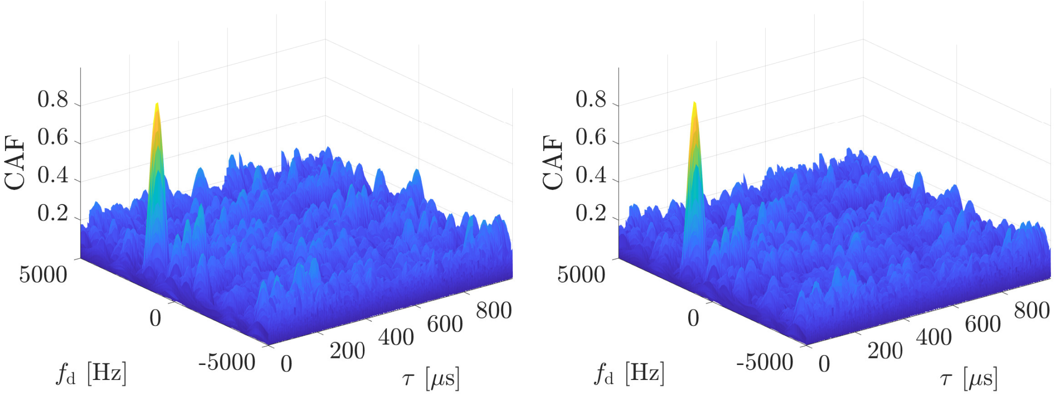

(c) SBNMF-STFT.

(d) SBNMF-FSST.

Figure 4.17: CAFs for the proposed techniques for $B = 14$ MHz and a JSR of 45 dB.

$B \in \{2, 8, 14\}$ MHz and CW-type RFI at 2 MHz – corrupting the received GNSS signal. Performance results are depicted in Figure 4.19, and similar to what was observed for the single RFI case, the NMF-based frameworks yield the highest GSNR levels in the case of multi-RFI sources.

Considering $B \in \{8, 14\}$ MHz, the semi-blind techniques lead to on par performance with their supervised counterparts for JSRs between 25 and 50 dB, and slightly degraded for JSRs = 45 and 50 dB. However, unlike the supervised techniques, they estimate the RFI frequency characteristics directly from the received signal. Therefore, regardless of the number of RFI corrupting the GNSS signals, the semi-blind framework attempts to mitigate RFI by calculating the corresponding $\mathbf{W}_\mathrm{RFI}$ matrix, which is further employed to separate interference from the signal of interest. This enables the suppression of numerous RFI without a prior characterisation scheme, or the use of antenna arrays.

Figure 4.20 displays the GPS signal detection results for multiple RFI. As before, the NMF-based methods yield the lowest C_min levels among all techniques considered. Similarly as in Section 4.3.2, the proposed NMF-based frameworks present superior detection performance despite the high JSR values considering two differ-

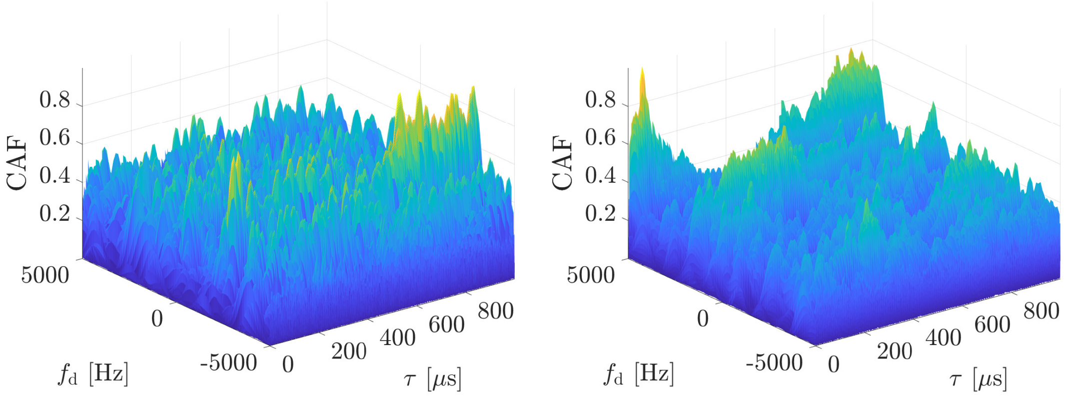

(a) Kalman.

(b) NF.

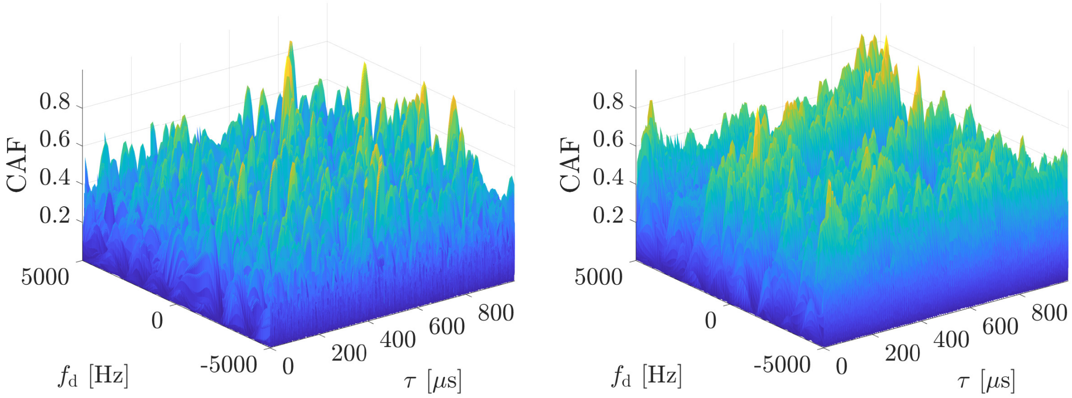

(c) Wavelet.

(d) No mitigation.

Figure 4.18: CAFs for the baseline techniques and no mitigation for $B = 14$ MHz and a JSR of 45 dB.

ent type RFI signals.

In general, the proposed NMF-based techniques outperform the baseline methods for distinct values of chirp bandwidth, enabling the GNSS signal acquisition in JSR levels as high as 50 dB, with the semi-blind NMF frameworks presenting similar or slightly degraded performance when compared to their supervised counterparts. The semi-blind NMF approaches however, do not require *a priori* information regarding the RFI and do not rely on any RFI characterisation scheme to estimate the RFI dictionary matrix $\mathbf{W}_{\mathrm{RFI}}$. Further, the NMF-based approach is able to suppress multiple RFI corrupting the received signal simultaneously.

4.4 Conclusions

In this chapter an NMF-based framework for RFI mitigation in GNSS is proposed. The supervised NMF extracts the RFI and signal of interest frequency features from clean interference signals prior to a calculation of their time activation properties. On the other hand, its semi-blind counterpart computes the interference fingerprint

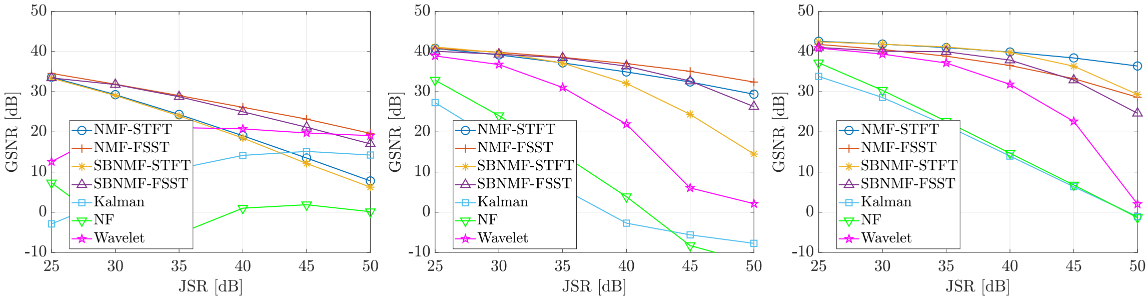

(a) $B = 2$ MHz.

(b) $B = 8$ MHz.

(c) $B = 14$ MHz.

Figure 4.19: Generalised SNR of the proposed and baseline techniques for different values of B for multiple RFI.

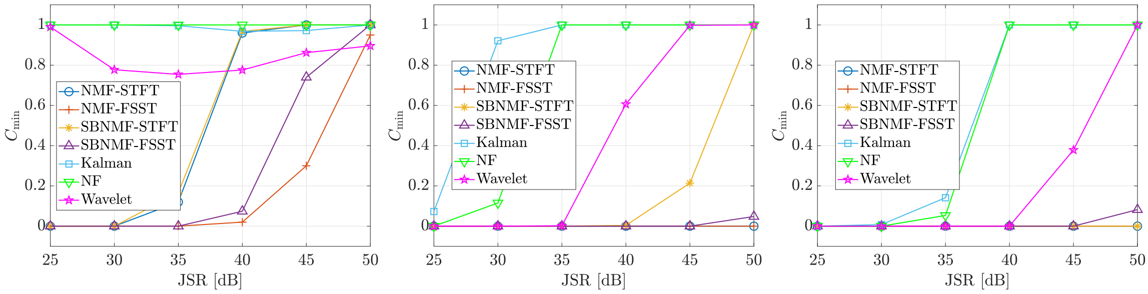

(a) $B = 2$ MHz.

(b) $B = 8$ MHz.

(c) $B = 14$ MHz.

Figure 4.20: $C_{\min}$ values of the proposed and baseline techniques for different values of B for multiple RFI.

directly from the received signal, e.g., it does not require *a priori* information about the RFI. The extracted frequency and time characteristics are used to estimate the RFI signals and signal of interest, which is then used in the GNSS receiver downstream.

Simulation results indicated that the proposed NMF-based scheme is able to mitigate narrow and wideband RFI signals in challenging JSR environments, outperforming techniques tailored to the RFI type (chirp), and classic methods from the literature, enabling the GNSS signal acquisition and further processing even in scenarios where the interference is 50 dB stronger than the GNSS signal. Further, the semi-blind scheme does not require any prior information or characterisation of the RFI, highlighting the flexibility of the NMF-based framework. Moreover, the proposed techniques are able to suppress multiple interference signals at the receiver, improving the reliability of GNSS-based services without requiring antenna arrays.

In the next chapter we adapt the proposed NMF-based schemes for the signals of the Parkes dataset. We describe how to train NMF to deal with pulsed interference, such as ADS-B signals, and analyse the impact of the proposed methods on the observation of cosmic events.

Chapter 5

Radio Frequency Interference Mitigation for Radio Astronomy

As discussed in Chapter 3, RFI can interfere with the astronomical observations, and even mimic the behaviour of pulsed-type events, such as pulsars [39]. To alleviate this, a TF-based RFI detection scheme for ADS-B signals was detailed and its performance analysed. This detector forms the first processing block in the receiver chain indicating the presence or absence of RFI. In the presence of RFI, the subsequent mitigation unit is triggered and further processing takes place to remove the aforementioned RFI.

One of the cosmic events of considerable interest in radio astronomy is the pulsar observation. Pulsars are magnetised rotating neutron stars that emit radio frequency beams out of their magnetic poles [85]. As the pulsar rotates, the beam sweeps around the sky, being periodically perceived by radio telescopes whenever the magnetic poles point towards the Earth, similar to the lighthouse working principle. Pulsars have relatively stable spinning periods, and for this reason, attract great interest for deep space navigation, being able to work as an alternative in the absence of GNSS-based systems [86, 87].

In this chapter, we briefly describe how the received signal is processed to observe the pulsar events. Further, we propose and outline three NMF-based techniques to suppress RFI in radio astronomy applications, with ADS-B being the major RFI of concern, while not corrupting underlying signal of interest and hence the observation of cosmic events.

5.1 Pulsar Processing

In order to analyse the pulsar characteristics, the received signal acquired by the radio telescopes undertakes a process called pulsar folding [40, 88]. The main idea is to integrate the pulsar signals according to the rotational period so that they can be observed, while compensating for the ionised interstellar medium (IISM). This frequency-dependent effect disperses the emitted waves along the path between the pulsar and the observer [40], with behaviour similar to multipath, altering the waves' time of arrival [89], degrading the performance of pulsar-based timing and synchronisation systems. A software package broadly used by the astronomers for this post-processing is the `DSPSR` [88]. Considering the Parkes dataset, the observed pulsar is the J1939+2134, a double pulsar (two neutron stars in orbit around each other), with rotational period around 1.56 ms. Using a 1-s long signal from sub-band 3 of the Parkes dataset as input to the software `DSPSR`, we are able to generate a spectrogram-like plot, hereafter called DSPSR spectrogram, shown in Figure 5.1(a), with a zoomed in version around the ADS-B centre frequency (1,090 MHz) in Figure 5.1(b). These spectrograms are calculated considering the sum of both signal polarisations. The DSPSR software provides information about the strongest RFI within the frequency range, highlighting the most powerful RFI at 1,090 MHz, indicating that the ADS-B signals represent a threat to the pulsar observation. Further, within 1,120–1,140 MHz, very sparse signals can be observed, which are related to the DME RFI. It is worth mentioning that there are also other interference signals in the Parkes dataset such as the ones at 1,100 MHz and within the interval 1,160–1,178 MHz. However, the sources of such RFI are still unknown to the experts in radio astronomy, with the major interference being flagged as the ADS-B signals by the software `DSPSR`. The pulsar profile is computed by integrating the frequency bins of the DSPSR spectrogram, resulting in a curve as shown in Figure 5.2, which consists of a pulsar phase vs. electromagnetic flux plot. Ideally, the peaks at around 0.1 and 0.6 would be more pronounced, with lower "noise" levels. However, due to interference, the profile estimation becomes less accurate, which directly impacts the observation and calculation of the pulsar characteristics.

5.2 NMF-Based RFI Mitigation Techniques

In this section we detail the proposed NMF-based techniques to mitigate RFI, with a major focus on the ADS-B signals, and analyse the impact of mitigation on the signal of interest, i.e., the pulsar observation.

5.2.1 Supervised NMF with Frequency Selection

The supervised NMF presented in Section 4.1.1 relies on the availability of clean versions of the signal of interest and respective RFI sources. Nonetheless, in real scenarios, including the signal captured by the Parkes radio telescope, these assump-

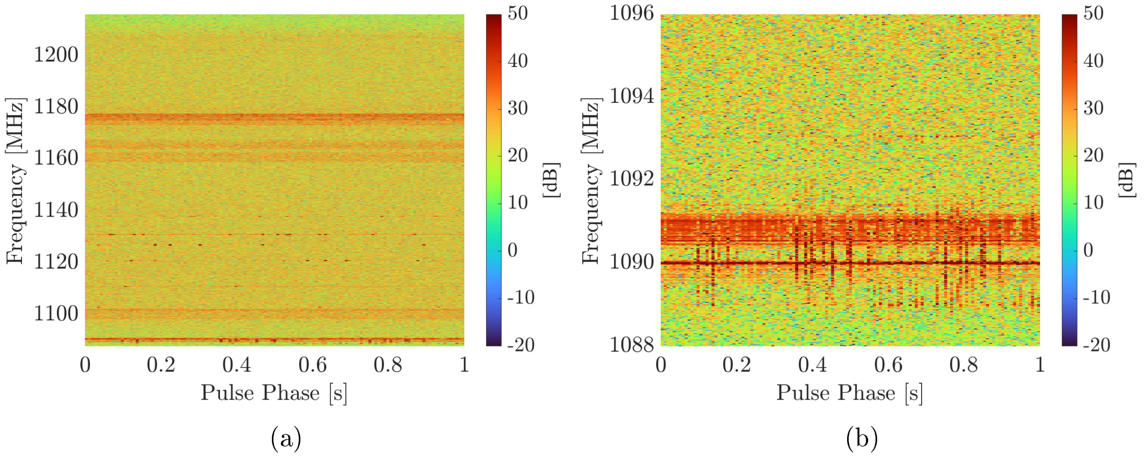

Figure 5.1: DSPSR spectrogram (a) with its zoomed in version at 1,090 MHz (b).

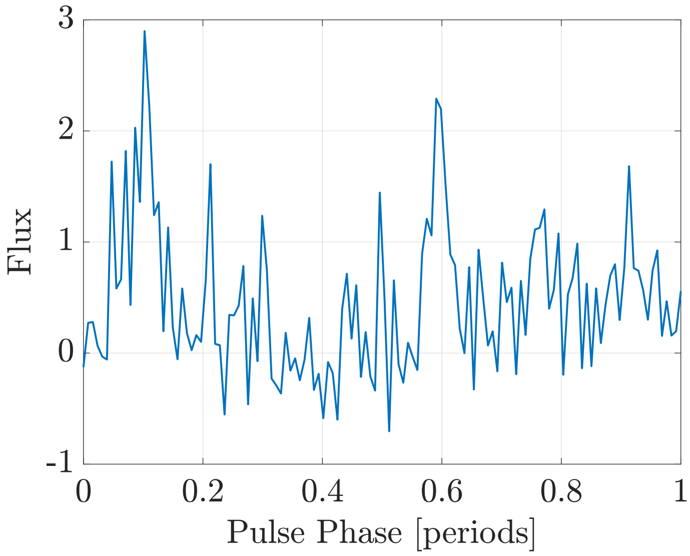

Figure 5.2: Pulsar profile without RFI mitigation.

tions rarely hold. Further, due to the short time duration of pulsed-type RFI, the signal frames labelled as corrupted by interference are mostly composed of the signal of interest, with only a few samples within each 10-ms signal frame corrupted by ADS-B. Thus, when estimating $\mathbf{W}_{\text{RFI}}$, the majority of its components represent the signal of interest, which, according to prior simulations, induced a larger disruption of the signal of interest. In order to alleviate this issue, we manually extract the excerpts of the Parkes dataset composed mainly of ADS-B signals and use them for evaluating $\mathbf{W}_{\text{RFI}}$. After estimating the RFI frequency content, we employ a post-processing scheme to eliminate spurious values in $\mathbf{W}_{\text{RFI}}$, since the ADS-B bandwidth is defined by international standards [64], we can easily select the appropriate ADS-B frequency range. Using 20 signal frames corrupted by ADS-B, considering the Kullback-Leibler divergence as distance function, and $S = 10$ to compute $\mathbf{W}_{\text{RFI}}$ and $\mathbf{W}_{\text{SOI}}$, Figures 5.3(a–b) show the estimated $\mathbf{W}_{\text{RFI}}$ before, and after frequency selection respectively, where each line represent a single column of $\mathbf{W}_{\mathrm{RFI}}$.

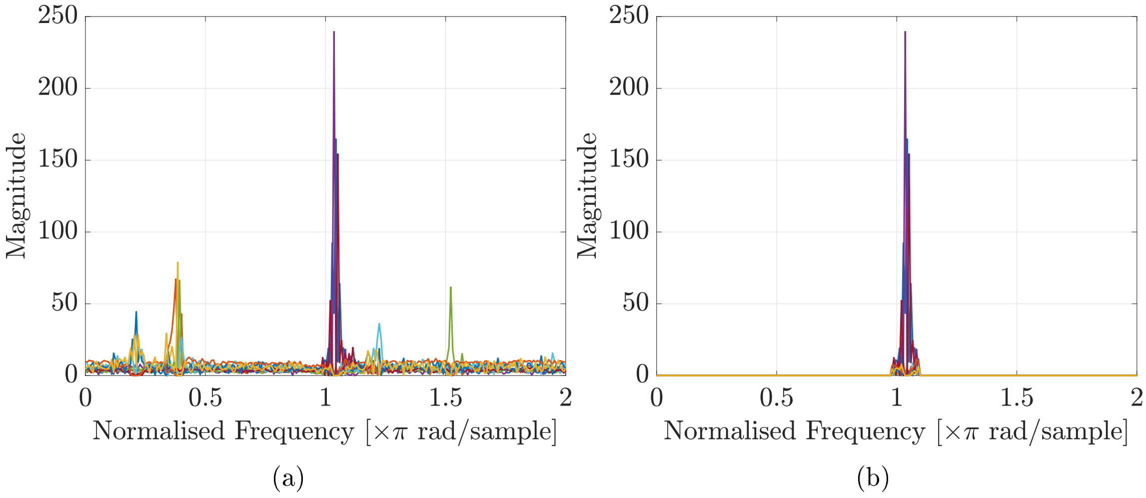

Figure 5.3: Estimated $\mathbf{W}_{\mathrm{RFI}}$ before (a) and after (b) frequency selection.

5.2.2 Supervised NMF with RFI Template

One of the drawbacks of the frequency selection detailed in the previous sub-section is that within the ADS-B signal bandwidth we also have, albeit small amount, the signal of interest. Therefore, to alleviate this problem, we employ the ADS-B template described in Section 3.3 as $\mathbf{W}_{\mathrm{RFI}}$. Consequently, the ADS-B frequency content in $\mathbf{W}_{\mathrm{RFI}}$ is represented by a single component i.e. a vector.

5.2.3 Semi-Blind NMF

In radio astronomy applications, besides not having clean RFI signals, there is also a considerable number of potential RFI sources due to the high sensitivity and wide frequency coverage of the receiver. In order to employ the supervised NMF framework, one would need to have a large variety of "clean" RFI signals to estimate $\mathbf{W}_{\mathrm{RFI}}$ properly. In order to address this issue, we propose the use of the semi-blind NMF to mitigate RFI, as described for the context of GNSS in Chapter 4. This way, no prior knowledge about the RFI is needed, with $\mathbf{W}_{\mathrm{SOI}}$ being computed from the interference free signal frames. Figures 5.4(a) and 5.4(c) show the magnitude spectrograms of two signal frames from the Parkes dataset and their corresponding $\mathbf{W}_{\mathrm{RFI}}$ matrices (Figures 5.4(b) and 5.4(d)) from polarisation A (polA). As mentioned in Chapter 3, the ADS-B signals are aliased due to their closeness to the channel edges and the characteristics of the polyphase filter bank' in the receiver. Hence, the following magnitude spectrograms' and $\mathbf{W}_{\mathrm{RFI}}$'s frequency axes are displayed from $[0, 2\pi]$ as opposed to the traditional $[-\pi, \pi]$ representation. The presence of ADS-B is highlighted by the black rectangles, whose spectral properties are described by one component (column) of $\mathbf{W}_{\mathrm{RFI}}$ as shown in Figure 5.4(b). In Figure 5.4(c), ADS-B as well as DME signals (blue rectangles) are present, with their corresponding spectral features displayed in Figure 5.4(d).

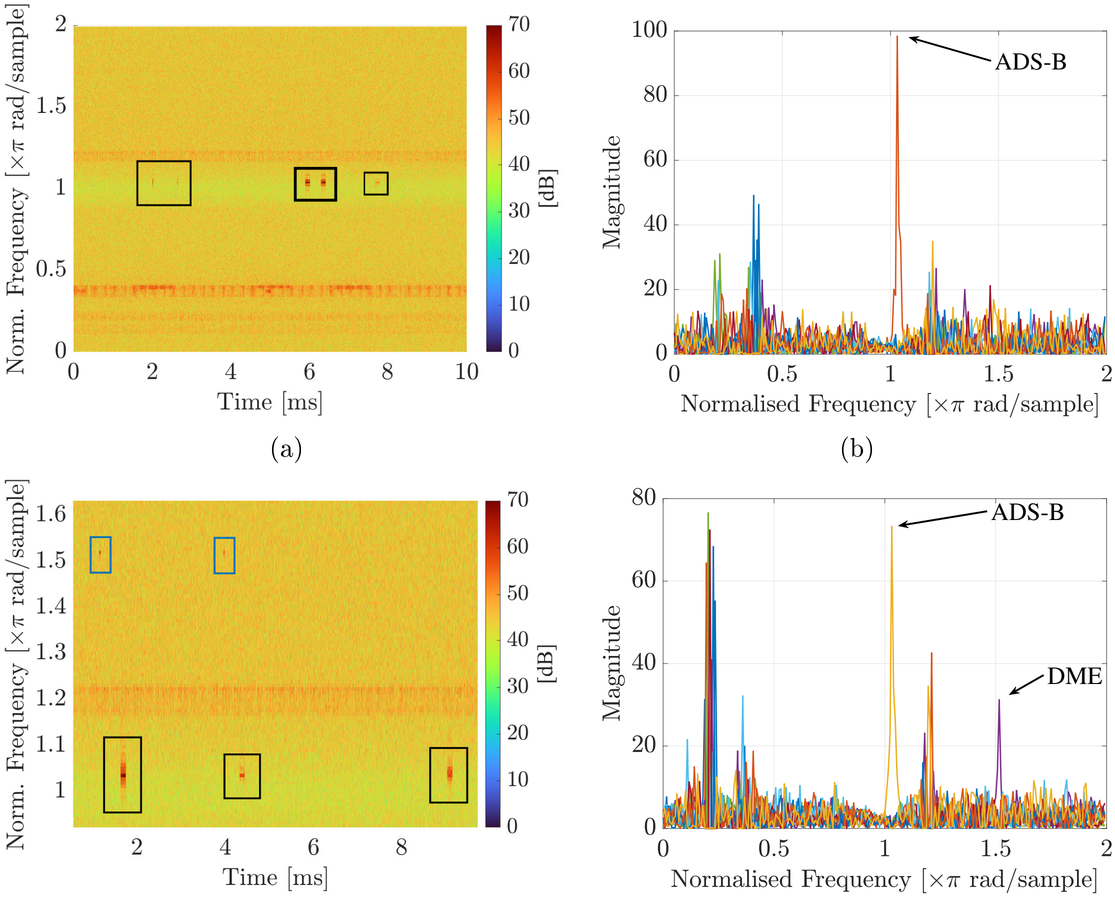

(a) (b)

(c) (d)

Figure 5.4: Magnitude spectrogram corrupted only by ADS-B (a) and its respective estimated $\mathbf{W}_{\mathrm{RFI}}$ (b), and a spectrogram corrupted by ADS-B and DME (c) and its corresponding calculated $\mathbf{W}_{\mathrm{RFI}}$ (d).

5.3 Performance Evaluation

In this section we assess the performance of the supervised and semi-blind NMF techniques presented in Sections 5.2.1, 5.2.2, and 5.2.3 respectively in mitigating RFI. Further, we also provide a discussion about the impact of the mitigation process on the signal of interest (pulsar signals). While supervised and semi-blind NMF can be used to mitigate ADS-B signals, only the semi-blind method is able to deal with multiple RFI concurrently, such as ADS-B and DME, without requiring any modification. In order to achieve the same for the supervised NMF, the training would have to take into account the DME occurrences as well, with a proper frequency selection for such interference. Hence, in this chapter we only evaluate the performance of ADS-B signal mitigation, although we describe how to suppress DME signals. The supervised NMF with frequency selection, supervised NMF with RFI template, and semi-blind NMF technique are hereafter referred to as NMF-Sel, NMF-Temp, and NMF-Semi respectively.

5.3.1 Figures of Merit

The performance of interference mitigation techniques in the RF-based communication systems is generally evaluated by means of the signal-to-interference-plus-noise ratio (SINR) [90]. In this case, one has a certain level of knowledge about the signal of interest and noise powers. Moreover, the focus is to suppress the RFI, with moderate concern about the signal of interest. In the area of audio processing, where the final goal is to separate different sources, such as instruments and voice, the SINR is employed along with subjective figures of merit, which measures the degradation of the separated signals from the human hearing perspective [91]. In the context of radio astronomy, the RFI power is rarely known, and the signal of interest is of major concern, where any artefact introduced by the mitigation algorithm may yield biased observations of the cosmic events. In [92], a figure of merit to evaluate the performance of time-frequency RFI mitigation techniques in radio astronomy signals was proposed. Nonetheless, it assumes prior knowledge about the RFI power and does not take into account the degradation to the signal of interest. In [93], the authors assess the performance of the techniques by analysing the spectrum before and after mitigation by visual inspection, without an objective figure of merit. In fact, the performance evaluation relies on the specific science case, with no figure of merit being a consensus among the astronomers. For this reason, in this work we gauge the performance based on two ways: the magnitude spectrograms of the signal of interest after RFI mitigation, which is here denominated as pre-folding, and based on pulsar profiles described in Section 5.1, named post-folding.

5.3.2 Experimental Setup

The data employed for the performance analysis in this chapter is also from the Parkes dataset, described in Section 3.2. This experimental uses the same dataset as in Section 3.2.1. The first 100 signal frames from the Parkes dataset are used here to calculate the pulsar profiles, with 76 of them corrupted by ADS-B and/or other RFI, and 24 without any interference. Regarding the STFT parameters, we use a rectangular window of length $L = 256$, number of DFT bins $N = 256$ and hop size of $R = L/2 = 128$ samples. As in Section 4.2.2, the FSST is not employed in this chapter due to the RFI time duration characteristics. As for the NMF parameters, we employ the KL divergence ($\beta = 1$), random initialisation of $\mathbf{W}$ and $\mathbf{H}$, and 10 components to represent both signal of interest and RFI signals, except for the case where we employ the ADS-B template (single component) to represent it. During the training phase, 20 signal frames are employed to compute $\mathbf{W}_{\mathrm{SOI}}$, and 20 signal frames out of the 76 are used to calculate $\mathbf{W}_{\mathrm{RFI}}$ (for NMF-Sel). It is worth mentioning that the NMF-based frameworks are employed on the signals of both polarisations i.e. polA and polB, and the matrices $\mathbf{W}_{\mathrm{RFI}}$ and $\mathbf{W}_{\mathrm{SOI}}$ are calculated considering each polarisation individually. All proposed frameworks share the same $\mathbf{W}_{\mathrm{SOI}}$ (computed considering polA), displayed in Figure 5.5. Moreover, NMF achieves convergence in our scenario within 300 iterations.

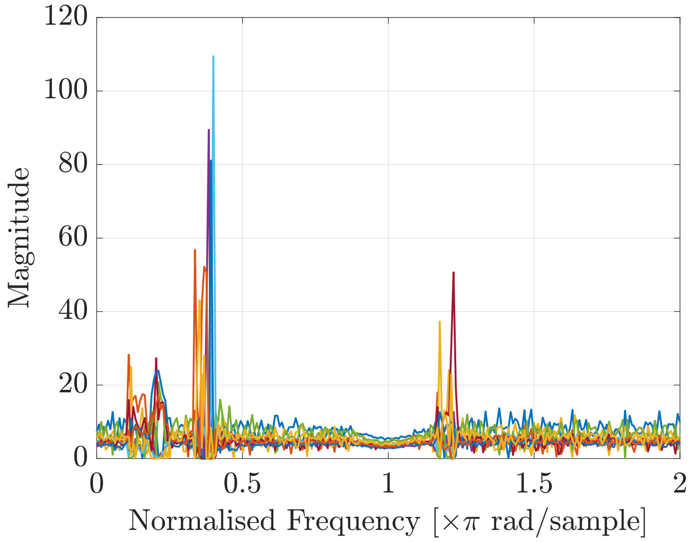

Figure 5.5: Estimated $\mathbf{W}_{\mathrm{SOI}}$ matrix during the training phase.

5.3.3 Pre-folding Results

In this subsection we describe the mitigation results by means of reconstructed spectrograms of the signal of interest. For the sake of simplicity, we only display the spectrograms corresponding to polA. Out of 76 signal frames used for performance evaluation, we show the corresponding spectrograms of the two most representative ones here. Figures 5.6(a–b) show two spectrograms corrupted by RFI from the Parkes dataset, where the black and blue rectangles point out the ADS-B and DME signals in the TF domain respectively. In those figures it is possible to observe strong ADS-B signals, and in Figure 5.6(b) two DME signals at around 1.5π rad/sample (1,120 MHz).

The NMF-Sel's reconstructed spectrograms are shown in Figures 5.7(a–b). Overall, the ADS-B signals are drastically suppressed, with only a residual fraction of ADS-B RFI within the leftmost rectangle in Figure 5.7(a). Also, the signal of interest does not seem to be attenuated, especially within the ADS-B signal frequency

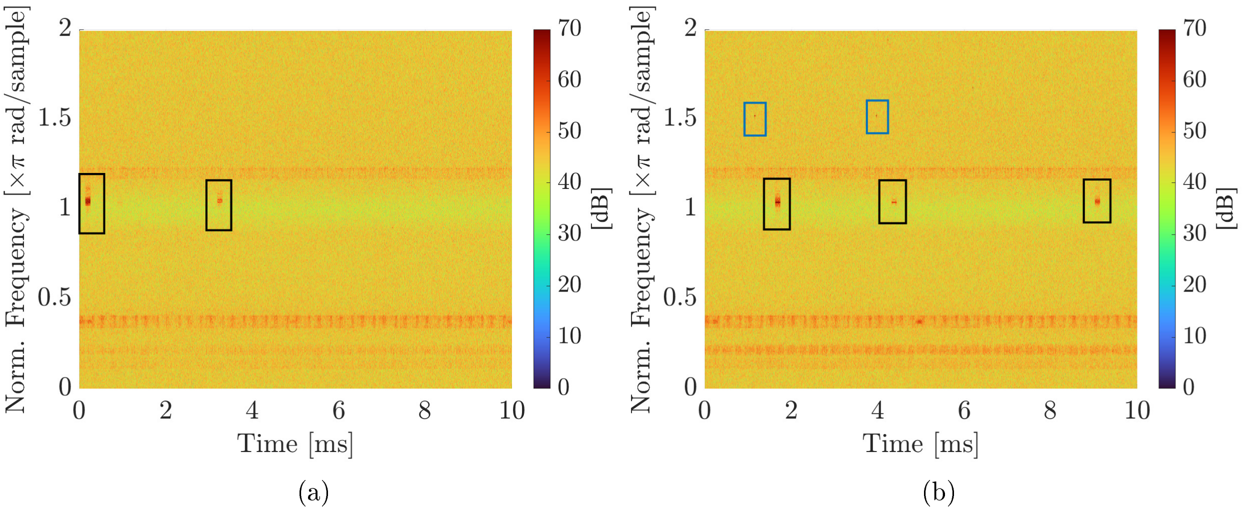

(a)

(b)

Figure 5.6: Spectrograms corrupted by ADS-B (a) and ADS-B & DME (b).

band. Interestingly, in Figure 5.7(b) the DME signals were not mitigated, although it is the expected behaviour since the matrix $\mathbf{W}_{\mathrm{RFI}}$ was calculated only considering ADS-B signals. Further, this reinforces the fact that the NMF-Sel framework is not corrupting the signal of interest.

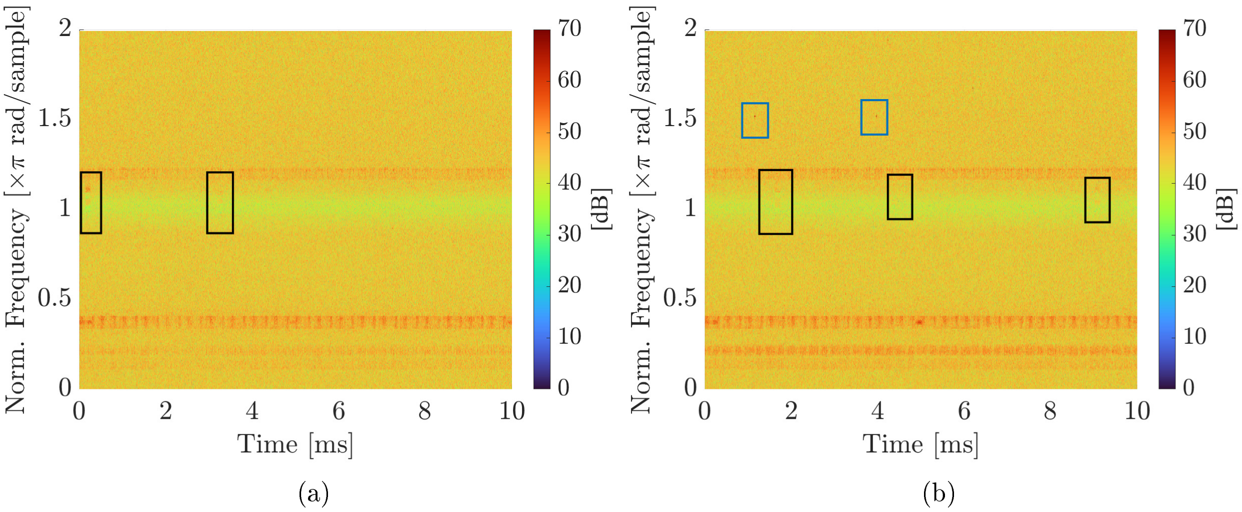

(a)

(b)

Figure 5.7: Reconstructed spectrograms of the signal of interest using the NMF-Sel technique from Figure 5.6(a) and Figure 5.6(b) respectively.

In regard to the NMF-Temp results, Figures 5.8(a–b) display the reconstructed spectrograms of the signal of interest with respect to Figures 5.6(a–b). As can be observed, there is significant ADS-B spectrum in the signal of interest, more specifically for the stronger ADS-B signals within the leftmost black rectangles. This is due to the fact that NMF-Temp employs a simple ADS-B template in $\mathbf{W}_{\mathrm{RFI}}$, i.e., a vector, whereas NMF-Sel uses $S = 10$ to estimate $\mathbf{W}_{\mathrm{RFI}}$ (Figure 5.3(b)). Therefore, NMF-Sel is able to represent the ADS-B signals in a better way than NMF-Temp, taking into account ADS-B signals with distinct strength and bandwidths. As a matter of fact, this spectrum varies according to numerous factors, such as distance and angle between aircraft and the radio telescope dish, and the antenna characteristics of the aircraft. NMF-Temp, however, does not require estimating the ADS-B signal characteristics from the received signal, nor the frequency selection process undertaken by NMF-Sel.

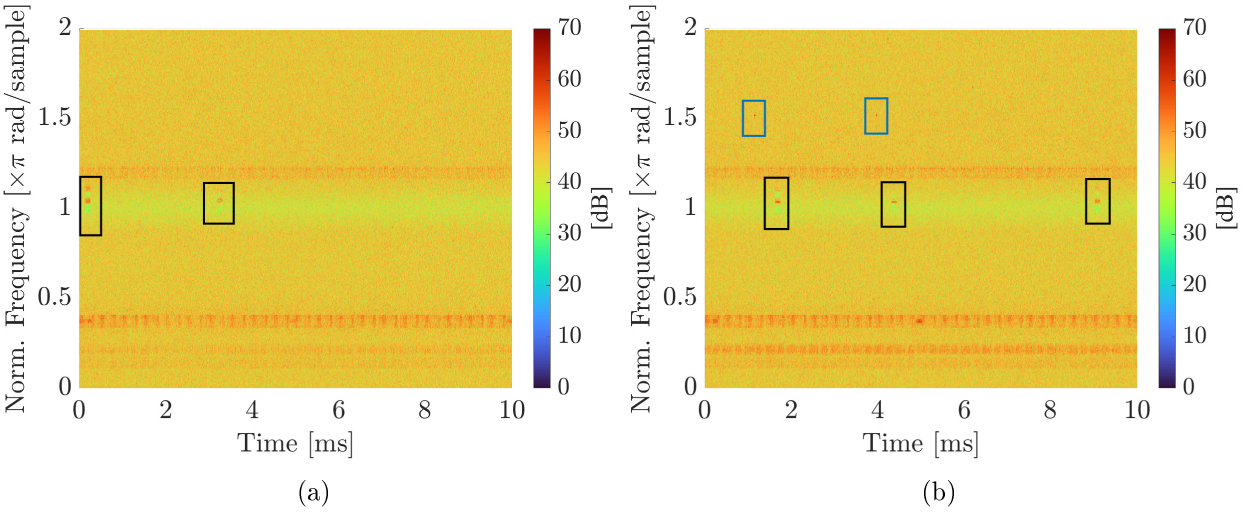

Figure 5.8: Reconstructed spectrograms of the signal of interest using the NMF-Temp technique from Figure 5.6(a) and Figure 5.6(b) respectively.

Considering the NMF-Semi performance, it is clear in Figures 5.9(a–b) that not only the ADS-B signals are mitigated but also the DME interference. Nonetheless, whenever the ADS-B is mitigated, the remaining frequency bins related to those time instants are also attenuated. This is a consequence of the estimated matrix $\mathbf{W}_{\text{RFI}}$, as in Figure 5.4(b), where the elements outside the ADS-B's spectrum are nonzero, thus, part of the frequency features of the signal of interest is also embedded in $\mathbf{W}_{\text{RFI}}$. As a result, when the NMF framework separates RFI from the signal of interest, a fraction of its power is present in the RFI's spectrogram. For instance, the signal of interest's power in Figures 5.9(a) is around 35 dB, whereas in Figures 5.7(a) and 5.7(a) is roughly 45 dB.

In general, the NMF-Sel technique presents the best results in terms of RFI mitigation while not disrupting the signal of interest. The NMF-Temp framework has poorer RFI suppression performance, however preserving the signal of interest. Lastly, the NMF-Semi scheme disregards prior knowledge about the interference sources, thus being able to mitigate multiple RFI. Nonetheless, this is achieved at the expense of attenuation of the signal of interest.

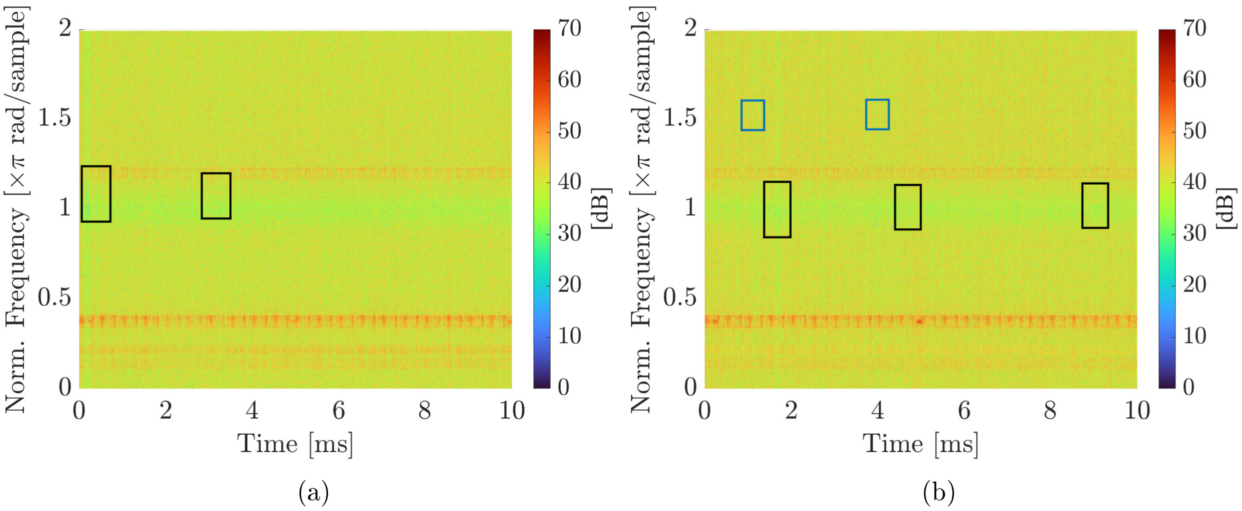

Figure 5.9: Reconstructed spectrograms of the signal of interest using the NMF-Semi technique from Figure 5.6(a) and Figure 5.6(b) respectively.

5.3.4 Post-folding Results

In this section we describe the mitigation results in terms of the pulsar profile, generated using the `DSPSR` software. Figure 5.10 shows the pulsar profiles generated using the reconstructed signal of interest respective to each of the NMF-based frameworks. Surprisingly, NMF-Sel and NMF-Temp have very similar pulsar profiles, despite the worse ADS-B suppression performance of the latter. One of the hypotheses is that the residual ADS-B spectrum in the signal of interest is averaged out by the pulsar folding, hence the similar results. Regarding NMF-Semi, as observed in previous spectrograms, this method considerably attenuates the signal of interest, which results in lower flux levels. As previously mentioned, the main capability of NMF-Semi is the mitigation of multiple RFI sources without prior knowledge. However, the main RFI of concern besides ADS-B is the DME interference, which does not corrupt many samples due to its very short time duration, thus, suppressing DME would not yield considerable improvements in terms of the pulsar profile.

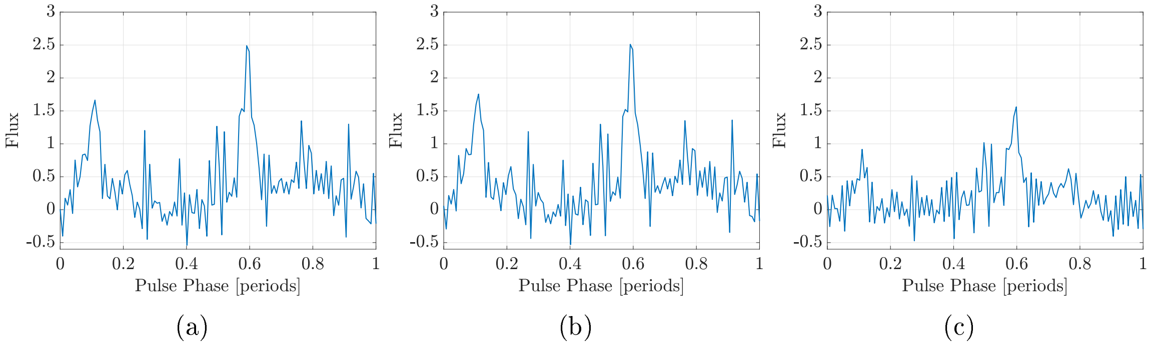

Figure 5.10: Pulsar profiles corresponding to NMF-Sel (a), NMF-Temp (b), and NMF-Semi (c).

Figure 5.11(a–b) displays the pulsar profile calculated from raw data (same as in Figure 5.2), and from flagged signals. Flagging consists of manually selecting the frequency channels of the DSPSR spectrogram corrupted by RFI and zeroing out their samples across all time instants. This way, the pulsar profile is generated neglecting the zeroed frequency channels, with the impact of RFI alleviated [45]. However, discarding samples is undesired since they may contain useful astronomical data. Moreover, flagging may completely hinder the observation of astronomical events in the case of other RFI types, such as satellite signals and mobile phone towers [40], which span much longer time periods, and wider frequencies. Furthermore, flagging may affect the analysis of the transient properties of pulsed-type cosmic events, e.g., pulsars [45]. Comparing Figures 5.10(a) and 5.11(a), one can note that the noisy behaviour outside the main peaks region (pulse phase around 0.1 and 0.6) is alleviated. Further, the leftmost peak in Figure 5.10(a) is more pronounced when compared to its neighbours, despite having a lower flux level. On the other hand, the rightmost peak has been enhanced, also with higher prominence. Considering Figure 5.11(b), the spurious peaks have been attenuated along with the rightmost peak. Also, the average level of the profile in between the peaks is now larger.

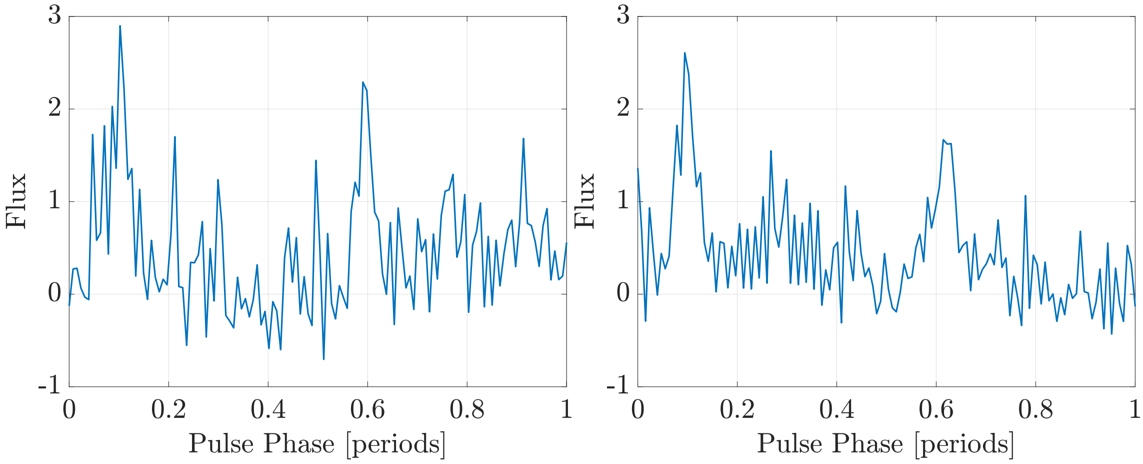

(a)

(b)

Figure 5.11: Pulsar profile from raw data (a) and from flagged signals (b).

5.4 Conclusions

Overall, the techniques described in this chapter present promising RFI mitigation performance, while not corrupting the underlying signal of interest. The main target for mitigation was the interference sources presented in sub-band 3 of the Parkes dataset, however, the proposed schemes for RFI mitigation can also be employed to work with signals from other sub-bands, with other RFI types involved. This work evaluated the potential of NMF in the context of radio astronomy, indicating its feasibility and pointing out the need of further research. Moreover, the results described in this chapter call for a deeper evaluation by experts on radio astronomy, which will bring more insights about the pulsar profiles and figures of merit for performance assessment.

Chapter 6

Conclusions and Future Work

In this thesis, we tackled the detection and mitigation of RFI in two applications: GNSS and radio astronomy. In relation to the RFI detection for GNSS, we investigated the challenges of detecting very weak narrow and wideband interference. In order to achieve this, we proposed an NMF-based framework able to extract the RFI's features from the power spectrogram of the received signal. The NMF estimated information is then compared with the spectrogram's time slices via a cosine similarity function. In the presence of RFI, the similarity achieves higher levels, which tend to be lower in the absence of RFI. Our framework compares the similarity values with a predefined threshold, followed by a majority voting scheme to aggregate the detection results of each time slice of the spectrogram into a single output, which enhances the performance under low JNR scenarios. The simulation results indicated that our NMF-based scheme yields high detection rates with low levels of false alarm, even in scenarios where the noise is 15 dB more powerful than the RFI. We also compared the performance with a state-of-the-art detection technique based on statistical tests. The proposal leads to similar detection results without *a priori* information about the RFI type, while maintaining lower computational complexity.

Considering interference detection for radio astronomy applications, we used signals captured by the Parkes radio telescope to assess the performance of our proposed detector. Extensive research on the RFI types present in our sub-band of interest was performed. Further, intensive manual labelling of the dataset was undertaken, so that the detection results could be properly inferred. Inspired by the NMF-based scheme for GNSS, we devised a TF-based detector for ADS-B signals, whose main characteristics are defined by international standards. Bases on them, we developed a ADS-B frequency template, which plays the role as the estimated RFI's frequency features by NMF. The proposed TF-based technique achieved high detection levels with low false alarms, outperforming methods widely employed in radio astronomy. Considering both GNSS and radio astronomy applications, RFI detection forms part of a larger framework, with interference mitigation being the next processing block in the received signal downstream.

The other main branch of this work is the RFI mitigation. In the context of GNSS, we studied the effects of RFI on the signal acquisition in the GNSS receiver. To alleviate this issue, we proposed an NMF-based framework with two distinct operation modes. Supervised NMF, which employs prior knowledge about the interference to estimate its frequency features, and semi-blind NMF, which calculates the interference frequency features directly from the received signal, and hence does not require *a priori* information about the RFI at hand. We assessed the performance of our proposed schemes considering two groups of interference, viz.: DME RFI, which can be classified as radar signals, and CW- and chirp-type RFI signals, that are commonly encountered in real-life environments. Considering the former, our proposal outperformed pulse-blanking-based techniques for DME mitigation, achieving higher levels of generalised SNR even under 60 dB-JSR scenarios. Also, unlike the pulse-blanking techniques, the proposal suppresses DME without discarding samples, thus preserving the GPS data. Based on the CW- and chirp-type signals as interference, we conducted studies on how to better represent chirps in the TF domain so that the overlap between the interference and signal of interest is minimised, aiding NMF with the separation task. To achieve this, we proposed the use of FSST, tailored for multicomponent signals such as chirp- and CW-type RFI, and incorporated it in our framework. Simulation results indicated that the NMF-based schemes can mitigate strong chirp signals with distinct bandwidth values, with better performance than techniques tailored to this RFI type, and classic methods as reported in the literature, enabling the GPS signal acquisition and further processing even in scenarios where the interference is 50 dB stronger than the GNSS signal. Moreover, the proposed techniques are able to suppress multiple interference signals at the receiver, improving the reliability of GNSS-based services without requiring multiple antennae.

We also investigated the RFI mitigation in the radio astronomy domain. By using data from the Parkes radio telescope, we were able to adapt the proposed NMF framework to mitigate ADS-B signals, aiming at minimal corruption of the underlying signal of interest. Besides employing the supervised and semi-blind schemes, we also proposed a supervised NMF using the ADS-B template as estimated RFI spectrum features. Through a qualitative performance assessment, we achieved promising results using the supervised NMF frameworks, with good ADS-B suppression. In addition, the pulsar profiles indicated that NMF appears to be able to mitigate the interference with minimal impact on the observation of cosmic events.

Future research work in the RFI detection for GNSS will investigate the application of denoising techniques so that even weaker RFI can be detected. Further, studies on other time-frequency representations more robust to noise should be conducted. In the radio astronomy domain, it is interesting to analyse further sub-bands of the Parkes dataset and their respective RFI. The number of potential interference increases on a daily basis and further mitigation work needs to be done. Also, the computational complexity of the proposed detector should be analysed and minimised with a view to hardware implementation.

Regarding RFI mitigation for GNSS, a future research direction would be to incorporating extra information about the interference, so that the matrices $\mathbf{W}_{\text{RFI}}$, $\mathbf{H}_{\text{RFI}}$ could be better estimated. For instance, considering a noise-free environment and chirp signals in the TF domain, at a given time instant only a few frequency bins are nonzero. Likewise, a given frequency bin has nonzero values only a few times, depending on its period. As a consequence, the matrices $\mathbf{W}_{\text{RFI}}$ and $\mathbf{H}_{\text{RFI}}$ tend to be orthogonal. Therefore, the NMF's cost function can be modified to leverage this property, so that enhanced mitigation results could be achieved. The mathematical details on this topic are described in Appendix A. Lastly, in the context of radio astronomy, another path that can be followed is the application of NMF after the pulsar folding. In this work, we operated on the spectrograms calculated from 10-ms long signal frames. Instead, the NMF matrices could be evaluated over the DSPSR spectrograms, which can be computed over several seconds, or even minutes worth of data. This would reduce the overall computational complexity drastically. In addition, further research on the pulsar profiles should be taken, so that, along with experts in the area, objective figures of merit to evaluate the mitigation performance can be established.

References

[1] VIANDIER, N., MARAIS, J., DE VERDALLE, E., et al. “Positioning urban buses: GNSS performances”. In: *2008 8th International Conference on ITS Telecommunications*, pp. 51–55, Phuket, Thailand, 2008.

[2] TADIC, S., FAVENZA, A., KAVADIAS, C., et al. “GHOST: A novel approach to smart city infrastructures monitoring through GNSS precise positioning”. In: *2016 IEEE International Smart Cities Conference (ISC2)*, pp. 1–6, Trento, Italy, 2016.

[3] BEUGIN, J., LEGRAND, C., MARAIS, J., et al. “Safety Appraisal of GNSS-Based Localization Systems Used in Train Spacing Control”, *IEEE Access*, v. 6, pp. 9898–9916, 2018.

[4] DEMPSTER, A. G., CETIN, E. “Interference localization for satellite navigation systems”, *Proceedings of the IEEE*, v. 104, n. 6, pp. 1318–1326, Jun. 2016.

[5] BORIO, D., O’DRISCOLL, C., FORTUNY, J. “Jammer impact on Galileo and GPS receivers”. In: *2013 International Conference on Localization and GNSS (ICL-GNSS)*, pp. 1–6, Turin, Italy, Jun. 2013.

[6] BORIO, D., DOVIS, F., KUUSNIEMI, H., et al. “Impact and detection of GNSS jammers on consumer grade satellite navigation receivers”, *Proceedings of the IEEE*, v. 104, n. 6, pp. 1233–1245, Jun. 2016.

[7] OJEDA, O. A. Y., GRAJAL, J., LOPEZ-RISUEÑO, G. “Analytical performance of GNSS receivers using interference mitigation techniques”, *IEEE Transactions on Aerospace and Electronic Systems*, v. 49, n. 2, pp. 885–906, Jul. 2013.

[8] KRAUS, T., BAUERNFEIND, R., EISSFELLER, B. “Survey of in-car jammers-analysis and modeling of the RF signals and IF samples (suitable for active signal cancelation)”. In: *Proc. 24th Int. Tech. Meeting Satellite Div. Inst. Navigat*, pp. 430–435, Portland, OR, USA, Sept. 2011.

[9] PATTINSON, M., DUMVILLE, M., YING, Y., et al. "Standardization of GNSS threat reporting and receiver testing through international knowledge exchange, experimentation and exploitation [STRIKE3]", *European Journal of Navigation*, v. 15, n. 3, pp. 4–12, Dec. 2017.

[10] WILDEMEERSCH, M., CANO, P. E., RABBACHIN, A., et al. *Impact study of unintentional interference on GNSS receivers*. Relatório Técnico EUR 24742 EN, EC Joint Research Centre, 2010.

[11] NUNES, F. D., SOUSA, F. M. G. "Interference detection in GNSS signals using the Gaussianity criterion". In: *2014 22nd European Signal Processing Conference (EUSIPCO)*, pp. 1497–1501, Lisbon, Portugal, Sept. 2014.

[12] CUNTZ, M., KONOVALTSEV, A., MEURER, M. "Concepts, development, and validation of multiantenna GNSS receivers for resilient navigation", *Proceedings of the IEEE*, v. 104, n. 6, pp. 1288–1301, Jun. 2016.

[13] CETIN, E., TRINKLE, M., BOURS, A., et al. "Overview of weak interference detection and localization techniques for the GNSS environmental monitoring system (GEMS)". In: *27th Int. Tech. Meeting Satellite Div. Inst. Navigat.*, pp. 2250–2259, Tampa, FL, USA, Sept 2014.

[14] BOURS, A., CETIN, E., DEMPSTER, A. G. "Enhanced GPS interference detection and localisation", *Electronics Letters*, v. 50, n. 19, pp. 1391–1393, Sept. 2014.

[15] BASTIDE, F., AKOS, D., MACABIAU, C., et al. "Automatic gain control (AGC) as an interference assessment tool". In: *16th International Technical Meeting of the Satellite Division of The Institute of Navigation (ION GPS/GNSS 2003)*, p. 2042–2053, Portland, OR, USA, Sept. 2003.

[16] THOMPSON, R. J. R., CETIN, E., DEMPSTER, A. G. "Detection and jammer-to-noise ratio estimation of interferers using the automatic gain control". In: *IGNSS Symp.*, pp. 1–14, Sydney, Australia, Nov. 2011.

[17] AXELL, E., EKLÖF, F. M., JOHANSSON, P., et al. "Jamming detection in GNSS receivers: performance evaluation of field trials", *Navigation*, v. 62, n. 1, pp. 73–82, Mar. 2015.

[18] KONOVALTSEV, A., DE LORENZO, D. S., HORNBOSTEL, A., et al. "Mitigation of continuous and pulsed radio interference with GNSS antenna arrays". In: *Proceedings of the 21st International Technical Meeting of the Satellite Division of The Institute of Navigation (ION GNSS 2008)*, pp. 2786–2795, Savannah, GA, USA, Sept. 2008.

[19] BROUMANDAN, A., JAFARNIA-JAHROMI, A., DANESHMAND, S., et al. "Overview of spatial processing approaches for GNSS structural interference detection and mitigation", *Proceedings of the IEEE*, v. 104, n. 6, pp. 1246–1257, Jun. 2016.

[20] TEUNISSEN, P., MONTENBRUCK, O. *Springer handbook of global navigation satellite systems*. 1 ed. New York, NY, USA, Springer, 2017.

[21] BALAEI, A. T., DEMPSTER, A. G., BARNES, J. "A novel approach in detection and characterization of CW interference of GPS signal using receiver estimation of C/N_0". In: *Proceedings of IEEE/ION PLANS 2006*, pp. 1120–1126, San Diego, CA, USA, Apr. 2006.

[22] BORIO, D., GIOIA, C. "Real-time jamming detection using the sum-of-squares paradigm". In: *2015 International Conference on Localization and GNSS (ICL-GNSS)*, pp. 1–6, Gothenburg, Sweden, Jun. 2015.

[23] FALLETTI, E., GAMBA, M. T., PINI, M. "Design and analysis of activation strategies for adaptive notch filters to suppress GNSS jamming", *IEEE Transactions on Aerospace and Electronic Systems*, v. 56, n. 5, pp. 3718–3734, Oct. 2020.

[24] JAHROMI, A. J., FADAEI, N., DANESHMAND, S., et al. "A review of pre-despreading GNSS interference detection techniques". In: *5th ESA Int. Colloq. Sci. Fundam. Aspects Galileo Program.*, pp. 1497–1501, Braunschweig, Germany, Oct. 2015.

[25] BORIO, D. "Swept GNSS jamming mitigation through pulse blanking". In: *2016 European Navigation Conference (ENC)*, pp. 1–8, Helsinki, Finland, May 2016.

[26] RAIMONDI, M., JULIEN, O., MACABIAU, C., et al. "Mitigating pulsed interference using frequency domain adaptive filtering". In: *19th Int. Tech. Meeting Satellite Div. Inst. Navigat.*, p. 2251–2260, Fort Worth, TX, USA, Jun. 2006.

[27] BORIO, D., CAMORIANO, L., SAVASTA, S., et al. "Time-frequency excision for GNSS applications", *IEEE Systems Journal*, v. 2, n. 1, pp. 27–37, Mar. 2008.

[28] MUSUMECI, L., DOVIS, F. "Use of the Wavelet transform for interference detection and mitigation in global navigation satellite systems", *International Journal of Navigation and Observation*, v. 2014, pp. 1–14, Oct. 2014.

[29] WANG, P., CETIN, E., DEMPSTER, A. G., et al. "GNSS interference detection using statistical analysis in the time-frequency domain", *IEEE Transactions on Aerospace and Electronic Systems*, v. 54, n. 1, pp. 416–428, Feb. 2018.

[30] WANG, P., WANG, Y., CETIN, E., et al. "Time-frequency jammer mitigation based on Kalman filter for GNSS receivers", *IEEE Transactions on Aerospace and Electronic Systems*, v. 55, n. 3, pp. 1561–1567, 2019.

[31] TANI, A., FANTACCI, R. "Performance evaluation of a precorrelation interference detection algorithm for the GNSS based on nonparametrical spectral estimation", *IEEE Systems Journal*, v. 2, n. 1, pp. 20–26, Mar. 2008.

[32] MOTELLA, B., PRESTI, L. L. "Methods of goodness of fit for GNSS interference detection", *IEEE Transactions on Aerospace and Electronic Systems*, v. 50, n. 3, pp. 1690–1700, Jul. 2014.

[33] MUSUMECI, L., CURRAN, J. T., DOVIS, F. "A comparative analysis of adaptive notch filtering and wavelet mitigation against jammers interference", *NAVIGATION*, v. 63, n. 4, pp. 533–550, 2016.

[34] MOSAVI, M. R., REZAEI, M. J., PASHAIAN, M., et al. "A fast and accurate anti-jamming system based on wavelet packet transform for GPS receivers", *GPS Solutions*, v. 21, n. 2, pp. 415–426, 2016.

[35] FORD, J. M., BUCH, K. D. "RFI mitigation techniques in radio astronomy". In: *2014 IEEE Geoscience and Remote Sensing Symposium*, pp. 231–234, Quebec City, QC, Canada, Jul. 2014.

[36] BELOSTOTSKI, L., HASLETT, J. W., VEIDT, B. "Wide-band CMOS low noise amplifier for applications in radio astronomy". In: *IEEE International Symposium on Circuits and Systems*, pp. 1347–1350, Island of Kos, Greece, 2006.

[37] FRIDMAN, P. A., BAAN, W. A. "RFI mitigation methods in radio astronomy", *A&A*, v. 378, n. 1, pp. 327–344, 2001.

[38] FIORI, F., CROVETTI, P. S. "Nonlinear effects of radio-frequency interference in operational amplifiers", *IEEE Transactions on Circuits and Systems I: Fundamental Theory and Applications*, v. 49, n. 3, pp. 367–372, 2002.

[39] CUCHO-PADIN, G., WANG, Y., LI, E., et al. "Radio frequency interference detection and mitigation using compressive statistical sensing", *Radio Science*, v. 54, n. 11, pp. 986–1001, Sept. 2019.

[40] HOBBS, G., OTHERS. “An ultra-wide bandwidth (704 to 4032 MHz) receiver for the Parkes radio telescope”, *Publications of the Astronomical Society of Australia*, Apr. 2020.

[41] BAAN, W. “RFI mitigation in radio astronomy”. In: *RFI Mitigation Workshop*, pp. 1–13, Groningen, Netherlands, Dec. 2010.

[42] OFFRINGA, A. R., DE BRUYN, A. G., BIEHL, M., et al. “Post-correlation radio frequency interference classification methods”, *Monthly Notices of the Royal Astronomical Society*, Mar. 2010.

[43] KESTEVEN, M. “Radio frequency interference mitigation in radioastronomy”. In: *IEEE International Conference on Acoustics, Speech, and Signal Processing*, v. 5, pp. 873–876, Philadelphia, PA, USA, Mar. 2005.

[44] MIDDELBERG, E. “Automated editing of radio interferometer data with PIEFLAG”, *Publications of the Astronomical Society of Australia*, v. 23, n. 2, pp. 64–68, 2006. doi: 10.1071/AS06004.

[45] CENDES, Y., PRASAD, P., ROWLINSON, A., et al. “RFI flagging implications for short-duration transients”, *Astronomy and Computing*, v. 23, pp. 103–114, 2018. ISSN: 2213-1337.

[46] PAATERO, P., TAPPER, U. “Positive matrix factorization: A non-negative factor model with optimal utilization of error estimates of data values”, *Environmetrics*, v. 5, n. 2, pp. 111–126, 1994.

[47] LEE, D. D., SEUNG, H. S. “Learning the parts of objects by non-negative matrix factorization”, *Nature*, v. 401, n. 6755, pp. 788–791, Oct. 1999.

[48] FU, X., HUANG, K., SIDIROPOULOS, N. D., et al. “Nonnegative matrix factorization for signal and data analytics: identifiability, algorithms, and applications”, *IEEE Signal Processing Magazine*, v. 36, n. 2, pp. 59–80, Mar. 2019.

[49] OZEROV, A., FEVOTTE, C. “Multichannel nonnegative matrix factorization in convolutive mixtures for audio source separation”, *IEEE Transactions on Audio, Speech, and Language Processing*, v. 18, n. 3, pp. 550–563, Mar. 2010.

[50] DIAS, T. L., MARTINS, W. A., BISCAINHO, L. W. P. “Multichannel source separation using time-deconvolutive CNMF”, *Journal of Communication and Information Systems*, v. 35, n. 1, pp. 103–112, May 2020.

[51] LEPLAT, V., GILLIS, N., ANG, A. M. S. "Blind audio source separation with minimum-volume beta-divergence NMF", *IEEE Transactions on Signal Processing*, v. 68, pp. 3400–3410, 2020.

[52] DA SILVA, F. B., CETIN, E., MARTINS, W. A. "Radio frequency interference detection using nonnegative matrix factorization", *IEEE Transactions on Aerospace and Electronic Systems*, pp. 1–1, 2021.

[53] CICHOCKI, A., ZDUNEK, R., AMARI, S. "New algorithms for non-negative matrix factorization in applications to blind source separation". In: *2006 IEEE International Conference on Acoustics Speech and Signal Processing Proceedings*, v. 5, pp. V–V, Toulouse, France, May 2006.

[54] SMARAGDIS, P. "Convolutive speech bases and their application to supervised speech separation", *IEEE Transactions on Audio, Speech, and Language Processing*, v. 15, n. 1, pp. 1–12, Jan. 2007.

[55] SHIMADA, K., BANDO, Y., MIMURA, M., et al. "Unsupervised speech enhancement based on multichannel NMF-informed beamforming for noise-robust automatic speech recognition", *IEEE/ACM Transactions on Audio, Speech, and Language Processing*, v. 27, n. 5, pp. 960–971, May 2019.

[56] ZAFEIRIOU, S., TEFAS, A., BUCIU, I., et al. "Exploiting discriminant information in nonnegative matrix factorization with application to frontal face verification", *IEEE Transactions on Neural Networks*, v. 17, n. 3, pp. 683–695, May 2006.

[57] TANG, Z., ZHANG, X., ZHANG, S. "Robust perceptual image hashing based on ring partition and NMF", *IEEE Transactions on Knowledge and Data Engineering*, v. 26, n. 3, pp. 711–724, Mar. 2014.

[58] FÉVOTTE, C., IDIER, J. "Algorithms for nonnegative matrix factorization with the β-divergence", *Neural Computation*, v. 23, n. 9, pp. 2421–2456, 2011.

[59] FÉVOTTE, C. "Majorization-minimization algorithm for smooth Itakura-Saito nonnegative matrix factorization". In: *2011 IEEE International Conference on Acoustics, Speech and Signal Processing (ICASSP)*, pp. 1980–1983, Prague, Czech Republic, May 2011.

[60] BOUTSIDIS, C., GALLOPOULOS, E. "SVD based initialization: A head start for nonnegative matrix factorization", *Pattern Recognition*, v. 41, n. 4, pp. 1350 – 1362, Apr. 2008.

[61] Li, S. Z., Jain, A. (Eds.). "Score Normalization". In: Li, S. Z., Jain, A. (Eds.), *Encyclopedia of Biometrics*, pp. 1134–1135, Boston, MA, Springer US, 2009.

[62] SCHOLKOPF, B., KAH-KAY SUNG, BURGES, C. J. C., et al. "Comparing support vector machines with Gaussian kernels to radial basis function classifiers", *IEEE Transactions on Signal Processing*, v. 45, n. 11, pp. 2758–2765, Nov. 1997.

[63] DA SILVA, F. B., CETIN, E., MARTINS, W. A. "ADS-B signal detection via time-frequency analysis for radio astronomy applications". In: *2021 IEEE International Symposium on Circuits and Systems (ISCAS)*, pp. 1–4, Daegu, South Korea, 2021.

[64] "Reception of automatic dependent surveillance broadcast via satellite and compatibility studies with incumbent systems in the frequency band 1087.7-1092.3 MHz", *M Series–Mobile, radiodetermination, amateur and related satellite services*, Nov. 2017.

[65] Available at <`https://www.atnf.csiro.au/observers/data/index.html`>. Accessed 01/03/2022.

[66] DA SILVA, F. B., CETIN, E., MARTINS, W. A. "DME interference mitigation for GNSS receivers via nonnegative matrix factorization". In: *2021 XXXIVth General Assembly and Scientific Symposium of the International Union of Radio Science (URSI GASS)*, pp. 1–4, Rome, Italy, 2021.

[67] DA SILVA, F. B., CETIN, E., MARTINS, W. A. "Radio frequency interference mitigation via nonnegative matrix factorization", *IEEE Transactions on Aerospace and Electronic Systems*, pp. 1–1, 2022. Under Review.

[68] ROUX, J. L., WENINGER, F., HERSHEY, J. R. "Sparse NMF – half-baked or well done?" 2015. Available at <`https://www.merl.com/publications/docs/TR2015-023.pdf`>. Accessed 01/03/2022.

[69] SMARAGDIS, P., RAJ, B., SHASHANKA, M. "Supervised and semi-supervised separation of sounds from single-channel mixtures,". In: *Independent Component Analysis and Signal Separation*, pp. 414–421, Berlin, Heidelberg, 2007. Springer Berlin Heidelberg.

[70] MYSORE, G. J., SMARAGDIS, P. "A non-negative approach to semi-supervised separation of speech from noise with the use of temporal dynamics". In: *2011 IEEE International Conference on Acoustics, Speech*

and Signal Processing (ICASSP), pp. 17–20, Prague, Czech Republic, 2011.

[71] FÉVOTTE, C., BERTIN, N., DURRIEU, J. “Nonnegative matrix factorization with the Itakura-Saito divergence: with application to music analysis”, *Neural Computation*, v. 21, n. 3, pp. 793–830, Mar. 2009.

[72] WANG, P., CETIN, E., DEMPSTER, A. G., et al. “Time frequency and statistical inference based interference detection technique for GNSS receivers”, *IEEE Transactions on Aerospace and Electronic Systems*, v. 53, n. 6, pp. 2865–2876, Dec. 2017.

[73] DINIZ, P. S. R., DA SILVA, E. A. B., NETTO, S. L. *Digital Signal Processing: System Analysis and Design.* 2 ed. 1 Liberty Plaza New York, NY, USA, Cambridge University Press, 2010.

[74] AUGER, F., FLANDRIN, P., LIN, Y.-T., et al. “Time-frequency reassignment and synchrosqueezing: an overview”, *IEEE Signal Processing Magazine*, v. 30, n. 6, pp. 32–41, 2013.

[75] OBERLIN, T., MEIGNEN, S., PERRIER, V. “The Fourier-based synchrosqueezing transform”. In: *2014 IEEE International Conference on Acoustics, Speech and Signal Processing (ICASSP)*, pp. 315–319, Florence, Italy, 2014.

[76] “Handbook on Radio Frequency Spectrum Requirements for Civil Aviation”, *ICAO spectrum strategy, policy statements and related information*, 2018.

[77] M. KAYTON, W. F. *Avionics Navigation Systems.* 2 ed. New York, NY, USA, Wiley, 1997.

[78] STEINGASS, A., THIASIRIPHET, T., SAMSON, J. “Modeling distance measurement equipment (DME) signals interfering an airborne GNSS receiver”, *NAVIGATION*, v. 65, n. 2, pp. 221–230, 2018.

[79] GAO, G. X. “DME/TACAN interference and its mitigation in L5/E5 bands”. In: *20th International Technical Meeting of the Satellite Division of The Institute of Navigation (ION GNSS 2007)*, pp. 1191–1200, Fort Worth, TX, USA, Sept. 2007.

[80] BRANDES, S., EPPLE, U., GLIGOREVIC, S., et al. “Physical layer specification of the L-band Digital Aeronautical Communications System (L-DACS1)”. In: *2009 Integrated Communications, Navigation and Surveillance Conference*, pp. 1–12, Arlington, VA, USA, 2009.

[81] MUSUMECI, L., SAMSON, J., DOVIS, F. "Performance assessment of pulse blanking mitigation in presence of multiple distance measuring equipment/tactical air navigation interference on global navigation satellite systems signals", *IET Radar, Sonar & Navigation*, v. 8, n. 6, pp. 647–657, 2014.

[82] BORRE, K., AKOS, D., BERTELSEN, N., et al. *A software-defined GPS and Galileo receiver: A single-frequency approach.* One New York Plaza, Suite 4600, New York, NY, USA, Springer, Jan. 2007.

[83] BORIO, D., GERNOT, C., MACCHI, F., et al. "The output SNR and its role in quantifying GNSS signal acquisition performance". In: *European Navigation Conference-GNSS*, pp. 231–234, Toulouse, France, Apr. 2008.

[84] PASCUAL, D. "danipascual/GNSS-matlab". Available at <`https://github.com/danipascual/GNSS-matlab`>. Accessed 01/03/2022.

[85] TAYLOR, J. "Millisecond pulsars: nature's most stable clocks", *Proceedings of the IEEE*, v. 79, n. 7, pp. 1054–1062, 1991.

[86] EMADZADEH, A. A., SPEYER, J. L. "On modeling and pulse phase estimation of X-Ray pulsars", *IEEE Transactions on Signal Processing*, v. 58, n. 9, pp. 4484–4495, 2010.

[87] EMADZADEH, A. A., SPEYER, J. L. "X-Ray pulsar-based relative navigation using epoch folding", *IEEE Transactions on Aerospace and Electronic Systems*, v. 47, n. 4, pp. 2317–2328, 2011.

[88] VAN STRATEN, W., BAILES, M. "DSPSR: digital signal processing software for pulsar astronomy", *Publications of the Astronomical Society of Australia*, v. 28, n. 1, pp. 1–14, 2011.

[89] KRISHNAKUMAR, M. A., MANOHARAN, P. K., JOSHI, B. C., et al. "High precision measurements of interstellar dispersion measure with the upgraded GMRT", *A&A*, v. 651, pp. A5, 2021.

[90] ANDREWS, J. G., BACCELLI, F., GANTI, R. K. "A tractable approach to coverage and rate in cellular networks", *IEEE Transactions on Communications*, v. 59, n. 11, pp. 3122–3134, Oct. 2011.

[91] HERSHEY, J. R., CHEN, Z., LE ROUX, J., et al. "Deep clustering: discriminative embeddings for segmentation and separation". In: *2016 IEEE International Conference on Acoustics, Speech and Signal Processing (ICASSP)*, pp. 31–35, Shanghai, China, Mar. 2016.

[92] QUEROL, J., ONRUBIA, R., ALONSO-ARROYO, A., et al. “Performance assessment of time–frequency RFI mitigation techniques in microwave radiometry”, *IEEE Journal of Selected Topics in Applied Earth Observations and Remote Sensing*, v. 10, n. 7, pp. 3096–3106, Feb. 2017.

[93] KESTEVEN, M., MANCHESTER, R., BROWN, A., et al. “Field trials of a RFI adaptive filter for pulsar Observations”. In: *RFI Mitigation Workshop*, p. 23, May 2010.

[94] BURRED, J. J., Mar. 2014. Available at <`https://www.jjburred.com/research/pdf/jjburred_nmf_updates.pdf`>. Accessed 01/03/2022.

Appendix A

NMF with Orthogonal Constraints

Figures A.1 illustrates the corresponding **W** and **H** matrices estimated by NMF considering a chirp signal with $B = 8$ MHz. As previously mentioned, chirp signals have orthogonal characteristics in the time and frequency domains. Therefore, one can modify the NMF cost function to aggregate this prior knowledge about the interference type. First, we show how to derive the standard update equations from NMF assuming the KL as distance function.

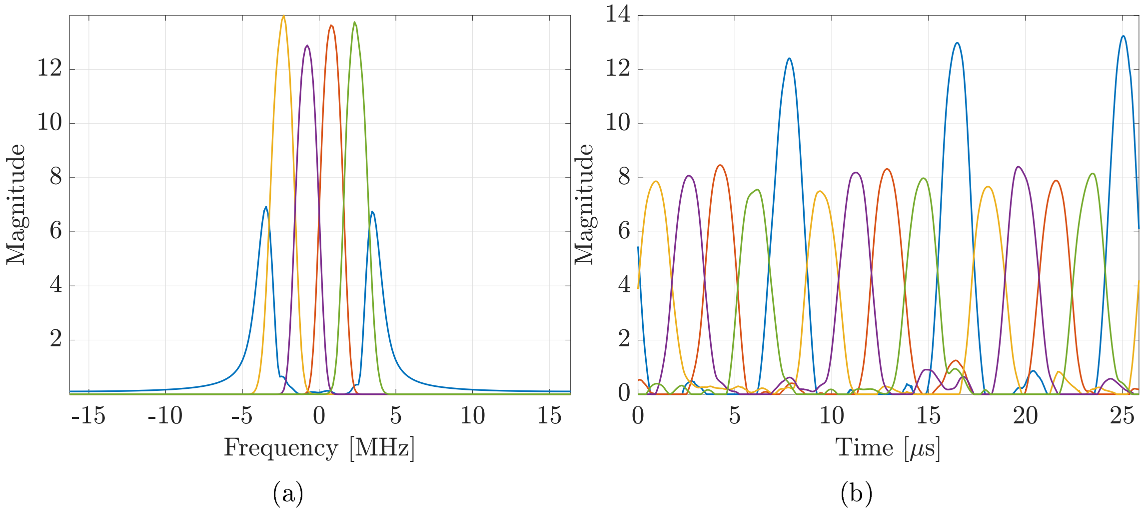

(a) (b)

Figure A.1: Columns of $\mathbf{W}_{\text{RFI}}$ (a) and rows of $\mathbf{H}_{\text{RFI}}$ (b) corresponding to a 8 MHz chirp-type RFI.

The optimisation problem to minimise the cost function $F(\mathbf{W},\mathbf{H})$ can be expressed as

$$\min_{\mathbf{W},\mathbf{H}} \bar{\mathbf{1}}^{\intercal} \left(\mathbf{X} \otimes \log\left(\frac{\mathbf{X}}{\mathbf{WH}}\right) + \mathbf{WH} - \mathbf{X} \right) \mathbf{1}$$
$$\text{subject to}\, \mathbf{W} \succeq 0, \mathbf{H} \succeq 0, \tag{A.1}$$

where $\bar{\mathbf{1}} \in \mathbb{N}^{N\times 1}$, $\mathbf{1} \in \mathbb{N}^{M\times 1}$ are vectors whose elements are 1's, and the division between $\mathbf{X}$ and $\mathbf{WH}$ is performed element-wise. In [94], it is shown that the gradient of $F(\mathbf{W},\mathbf{H})$ with relation to $\mathbf{W}$ and $\mathbf{H}$ can be described as

$$\nabla_{\mathbf{W}} F(\mathbf{W},\mathbf{H}) = \mathbf{1}'\mathbf{H}^{\intercal} - \frac{\mathbf{X}}{\mathbf{WH}}\mathbf{H}^{\intercal}, \tag{A.2}$$

$$\nabla_{\mathbf{H}} F(\mathbf{W},\mathbf{H}) = \mathbf{W}^{\intercal}\mathbf{1}' - \mathbf{W}^{\intercal}\frac{\mathbf{X}}{\mathbf{WH}}, \tag{A.3}$$

where $\mathbf{1}' \in \mathbb{N}^{N\times M}$ is a matrix composed of 1's. A simple method to describe the update equations for $\mathbf{W}$, avoiding subtractions, is to use the positive and negative terms of the gradient $\nabla_{\mathbf{W}} F(\mathbf{W},\mathbf{H})$, denoted as $[\nabla_{\mathbf{W}} F(\mathbf{W},\mathbf{H})]^{-}$, $[\nabla_{\mathbf{W}} F(\mathbf{W},\mathbf{H})]^{+}$ respectively, as follows [58]:

$$\mathbf{W}[k+1] = \mathbf{W}[k] \otimes \frac{[\nabla_{\mathbf{W}} F(\mathbf{W},\mathbf{H})]^{-}}{[\nabla_{\mathbf{W}} F(\mathbf{W},\mathbf{H})]^{+}}. \tag{A.4}$$

Therefore, using (A.2) and (A.4), the update equation for $\mathbf{W}$ can be described as

$$\mathbf{W}[k+1] = \mathbf{W}[k] \otimes \frac{\frac{\mathbf{X}}{\mathbf{W}[k]\mathbf{H}[k]}\mathbf{H}^{\intercal}[k]}{\mathbf{1}'\mathbf{H}^{\intercal}[k]}. \tag{A.5}$$

Conversely, the update equation for $\mathbf{H}$ using (A.3) and (A.4) are expressed as

$$\mathbf{H}[k+1] = \mathbf{H}[k] \otimes \frac{\mathbf{W}^{\intercal}[k+1]\frac{\mathbf{X}}{\mathbf{W}[k+1]\mathbf{H}[k]}}{\mathbf{W}^{\intercal}[k+1]\mathbf{1}'}. \tag{A.6}$$

In order to impose orthogonal constraints on $\mathbf{W}$ and $\mathbf{H}$, (A.1) can be modified as

$$\begin{aligned} &\min_{\mathbf{W},\mathbf{H}} \bar{\mathbf{1}}^{\intercal}\left(\mathbf{X}\otimes\log\left(\frac{\mathbf{X}}{\mathbf{WH}}\right)+\mathbf{WH}-\mathbf{X}\right)\mathbf{1} + \alpha_{\mathrm{W}}\sum_{i\neq j}\mathbf{w}_i^{\intercal}\mathbf{w}_j + \alpha_{\mathrm{H}}\sum_{i\neq j}\mathbf{h}_i\mathbf{h}_j^{\intercal} \\ &\text{subject to}\, \mathbf{W}\succeq 0, \mathbf{H}\succeq 0, \end{aligned} \tag{A.7}$$

where $\alpha_{\mathrm{W}} \in \mathbb{R}_{+}$, $\alpha_{\mathrm{H}} \in \mathbb{R}_{+}$ are penalty factors. After cumbersome matrix derivatives, denoting the modified cost function as $\overline{F}(\mathbf{W},\mathbf{H})$, the gradients with relation to $\mathbf{W}$ and $\mathbf{H}$ can be rewritten as

$$\nabla_{\mathbf{W}} \overline{F}(\mathbf{W},\mathbf{H}) = \mathbf{1}'\mathbf{H}^{\intercal} - \frac{\mathbf{X}}{\mathbf{WH}}\mathbf{H}^{\intercal} + \alpha_{\mathrm{W}}(\mathbf{W}(\check{\mathbf{1}}\check{\mathbf{1}}^{\intercal} - \mathbf{I}_{S\times S})), \tag{A.8}$$

$$\nabla_{\mathbf{H}} \overline{F}(\mathbf{W},\mathbf{H}) = \mathbf{W}^{\intercal}\mathbf{1}' - \mathbf{W}^{\intercal}\frac{\mathbf{X}}{\mathbf{WH}} + \alpha_{\mathrm{H}}((\check{\mathbf{1}}\check{\mathbf{1}}^{\intercal} - \mathbf{I}_{S\times S})\mathbf{H}), \tag{A.9}$$

where $\check{\mathbf{1}} \in \mathbb{N}^{S\times 1}$ is a vector of 1's, and $\mathbf{I}_{S\times S}$ stands for a square identity matrix whose dimensions are defined by the number of components S. The resulting update equation for $\mathbf{W}$ considering (A.8) and (A.4) can be expressed as

$$\mathbf{W}[k+1] = \mathbf{W}[k] \otimes \left(\frac{\frac{\mathbf{X}}{\mathbf{W}[k]\mathbf{H}[k]}\mathbf{H}^{\intercal}[k] + \alpha_{\mathrm{W}}\mathbf{W}[k]}{\mathbf{1}'\mathbf{H}^{\intercal}[k] + \alpha_{\mathrm{W}}\mathbf{W}[k]\check{\mathbf{1}}\check{\mathbf{1}}^{\intercal}} \right). \tag{A.10}$$

Likewise,

$$\mathbf{H}[k+1] = \mathbf{H}[k] \otimes \left(\frac{\mathbf{W}^{\intercal}[k]\frac{\mathbf{X}}{\mathbf{W}[k]\mathbf{H}[k]} + \alpha_{\mathrm{H}}\mathbf{H}[k]}{\mathbf{W}^{\intercal}[k]\mathbf{1}' + \alpha_{\mathrm{H}}\check{\mathbf{1}}\check{\mathbf{1}}^{\intercal}\mathbf{H}[k]} \right). \tag{A.11}$$

As described in Chapter 4, considering the supervised NMF framework, in the test phase the matrix $\mathbf{H}$ can be written as $\mathbf{H} = [\,\mathbf{H}_{\mathrm{RFI}}^{\intercal}\mathbf{H}_{\mathrm{SOI}}^{\intercal}\,]^{\intercal}$. Therefore, it is desired to introduce orthogonal constraints only on $\mathbf{H}_{\mathrm{RFI}}$. As a consequence, (A.11) should be adapted accordingly. In this sense, assuming that the number of components for the RFI and signal of interest is S, a partial update of $\mathbf{H}$ is achieved with the use of the matrix $\mathbf{C} \in \mathbb{N}^{S\times S}$, defined as

$$\mathbf{C} = \operatorname{diag}\left([\mathbf{1}_S\,\mathbf{0}_S]\right), \tag{A.12}$$

where the operator diag ($\mathbf{a}$) creates a diagonal square matrix whose nonzero elements are described by $\mathbf{a}$. Then, (A.11) can be rewritten as

$$\mathbf{H}[k+1] = \mathbf{H}[k] \otimes \left(\frac{\mathbf{W}^{\intercal}[k]\frac{\mathbf{X}}{\mathbf{W}[k]\mathbf{H}[k]} + \alpha_{\mathrm{H}}\mathbf{C}\mathbf{H}[k]}{\mathbf{W}^{\intercal}[k]\mathbf{1}' + \alpha_{\mathrm{H}}\mathbf{C}\check{\mathbf{1}}\check{\mathbf{1}}^{\intercal}\mathbf{C}\mathbf{H}[k]} \right). \tag{A.13}$$

This way, only the first S rows of $\mathbf{H}$ are updated according to the orthogonal constraints, hence, only $\mathbf{H}_{\mathrm{RFI}}$. Therefore, it is expected that when α_{W} and α_{H} are set properly during the training phase, a better representation of the chirp's frequency features is achieved. In addition, in the test phase, if $\mathbf{H}_{\mathrm{RFI}}$ is estimated considering the chirp signal time properties, we hope that it will yield a better representation of such RFI, thereby enhanced suppression performance, especially in the case of smaller bandwidth values, such as $B = 2$ MHz.